Dynamics and Transport of Laser-Accelerated Particle Beams

Stefan Becker

München 2010

Dynamics and Transport of Laser-Accelerated Particle Beams

Dissertation
an der Fakultät für Physik
der Ludwig–Maximilians–Universität
München

vorgelegt von
Stefan Becker
aus Hagen

München, den 5. Jan. 2010

Erstgutachter: Prof. Dr. Roland Sauerbrey
Zweitgutachter: Prof. Dr. Stefan Karsch
Tag der mündlichen Prüfung: 19. Apr. 2010

Contents

List of Figures

List of Tables

Zusammenfassung

Gegenstand der vorliegenden Arbeit ist die Untersuchung und Optimierung von Strahlführungselementen im stetig wachsenden Bereich der Laser-Teilchen-Beschleunigung. Diese kumulative Dissertation führt ein in die theoretischen Grundlagen der Elemente und präsentiert die Resultate anhand der entsprechenden Veröffentlichungen.

Der erste Themenbereich ist die Untersuchung der freien Vakuumexpansion eines Elektronenstrahls hoher Stromdichte. Anders als bei konventioneller Teilchen-Beschleunigung weisen laserbeschleunigte Elektronenstrahlen vergleichsweise hohe Ladungsdichten bei niedrigen Strahlenergien auf. Es hat sich gezeigt, dass die Berechnung der Raumladungseffekte in diesem Regime mit üblichen Simulationsprogrammen ausgeprägte Artefakte generieren. Sie setzen sich zusammen aus mangelhaften Annahmen für die Lorentztransformation, aus unzulänglichen Anfangsbedingungen und aus nicht vernachlässigbaren Retardierungsartefakten. Bestandteil dieser Arbeit ist die Entwicklung eines adäquaten Ansatzes für die Berechnung von laserbeschleunigten Elektronenstrahlen. Dieser kann auch zur Validierung weiterer Berechnungsmethoden für Raumladungseffekte verwendet werden.

Die nächsten betrachteten Elemente sind miniaturisierte magnetische Quadrupole zur Fokussierung geladener Teilchenstrahlen. Diese Quadrupole wurden um 1980 von Halbach erfunden und erzeugen Feldgradienten, die mindestens einen Faktor 2 über supraleitenden Quadrupolen liegen. Das generelle Problem im Zuge der Miniaturisierung ist das Auftreten störender Feldkomponenten höherer Ordnung. Können diese Komponenten nicht kontrolliert werden, so schmälert sich das Anwendungsfeld bedeutend. In der vorliegenden Arbeit wurde nicht nur ein Verfahren zur Charakterisierung der Komponenten entwickelt, sondern auch ein Verfahren zur Kompensation der störenden Komponenten. Dies könnte sich zu einer Standardmethode für den Bau dieser permanentmagnetischen Multipolgeräte entwickeln, wodurch deren Anwendungsbereich bedeutend erweitert werden könnte. Die neu entwickelte Methode zur Charakterisierung wurde am Elektronenstrahl des Mainzer Microtrons (MAMI) validiert. Da nun die optimale Leistung sichergestellt werden kann, wird die erste Anwendung im Zusammenhang mit Ionenstrahlen präsentiert. Das Experiment wurde am Z-Petawatt Lasersystem der Sandia National Laboratories durchgeführt.

Ein Freier Elektronenlaser (FEL) erzeugt kohärente Photonenstrahlen, deren Energie höher ist als die von konventionellen Lasern. Eine vielversprechende Anwendung von laserbeschle-

unigten Elektronenstrahlen ist der FEL in einer Größe, wie sie für das universitäre Umfeld geeignet ist. Die erste Diskussion aller relevanten Aspekte für einen lasergetriebenen FEL wird präsentiert.

Der Betrieb eines FELs hängt von mehreren Faktoren ab, unter denen sich die durchschnittliche Strahlgröße während der Propagation durch den Undulator befindet. Die Undulatorlänge könnte bedeutend reduziert werden wenn die durchschnittliche Strahlgröße verringert werden kann. Dieses Ziel motiviert die Entwicklung eines neuen Undulatorkonzepts, das auf den Miniaturmagnetquadrupolen basiert, die hier präsentiert werden. Dieser Quadrupolundulator weist starke intrinsische Fokussierungseigenschaften auf, die den Elektronenstrahl auf vergleichsweise kleinen und konstanten Strahlgrößen über lange Propagationstrecken hinweg zu halten vermögen.

Die experimentelle Umsetzung eines kompakten FELs beinhaltet im ersten Schritt den Bau eines Testundulators mit kurzen Periodenlängen. Im Rahmen der vorliegenden Arbeit wurde dieser Undulator hergestellt und Undulatorstrahlungsexperimente am Elektronenbeschleuniger MAMI durchgeführt.

Die hier präsentierten Untersuchungen markieren bedeutende Etappenziele auf dem Weg der Entwicklung vieler Anwendungen von laserbeschleunigten Teilchenstrahlen. Insbesondere stellen lasergetriebene kompakte FELs eine attraktive Alternative zu großen hochpreisigen konventionellen Systemen dar.

Summary

The subject of this thesis is the investigation and optimization of beam transport elements in the context of the steadily growing field of laser-driven particle acceleration. This cumulative thesis introduces to the theoretical framework of the elements and presents the results via corresponding publications. The first topic is the examination of the free vacuum expansion of an electron beam at high current density. Unlike in the case of conventional acceleration, laser acceleration yields charge densities which are comparatively high at lower energies. It could be shown that particle tracking codes which are commonly used for the calculation of space charge effects will generate substantial artifacts in the regime considered here. The artifacts occurring hitherto predominantly involve insufficient prerequisites for the Lorentz transformation, the application of inadequate initial conditions and non negligible retardation artifacts. A part of this thesis is dedicated to the development of a calculation approach which uses a more adequate ansatz calculating space charge effects for laser-accelerated electron beams. It can also be used to validate further approaches for the calculation of space charge effects.

The next elements considered are miniature magnetic quadrupole devices for the focusing of charged particle beams. Invented in 1980 by Halbach, miniature permanent magnet quadrupoles yield field gradients at least a factor two higher than superconducting quadrupole devices. General problems involved with their miniaturization concern distorting higher order field components. If these distorting components cannot be controlled, the field of applications is very limited. In this thesis a new method for the characterization and compensation of the distorting components was developed, which might become a standard method when assembling these permanent magnet multipole devices. Consequently, the field where these devices are applicable could be broadened. The newly developed characterization method has been validated at the Mainz Microtron (MAMI) electron accelerator. Now that we can ensure optimum performance, the first application of permanent magnet quadrupole devices in conjunction with laser-accelerated ion beams is presented. The experiment was carried out at the Z-Petawatt laser system at Sandia National Laboratories.

A Free Electron Laser (FEL) delivers coherent photon beams at higher energies than what can be reached by conventional laser systems. A promising application for laser-accelerated electron beams is the FEL in a university-scale size. The first discussion of all relevant aspects concerning a laser driven FEL is presented.

The operation of an FEL depends on many factors, among which is the average electron beam size while propagating through the undulator. The undulator length could be reduced significantly if the average beam size can be reduced. This goal motivates the development of a new undulator concept, based on miniature magnetic quadrupoles, which is presented here. This quadrupole undulator yields strong intrinsic focusing properties which allow to keep the electron beam at a comparatively small and constant size over a long propagation range.

The experimental realization of a compact FEL involves the first step of building a test undulator with a short undulator period length. This undulator device was assembled and experiments aiming at undulator radiation have been carried out at the MAMI electron accelerator facility in the course of this thesis.

The investigations presented in this thesis mark important development steps on the route towards many applications of laser-accelerated particle beams. Especially laser-driven compact Free-Electron-Lasers are an attractive alternative to costly large-scale conventional facilities.

Chapter 1

Motivation

The evolution of laser intensity within the past decades has been constantly opening up new fields of applications. In 1985, the laser intensity took an important step forward with the invention of the chirped pulse amplification (CPA) technique by Strickland and Mourou [1], allowing to generate light intensities easily surpassing the relativistic limit (10^{18} W/cm^2). At these intensities the motion of electrons in the laser fields becomes relativistic, leading to a plethora of new phenomena. Among the most actively pursued research fields sparked off by this new regime is the acceleration of charged particles, which has been theoretically predicted [2, 3] and experimentally demonstrated [4, 5]. Compared to conventional particle acceleration with an acceleration length of many meters up to kilometers required, this approach reduces the distances to the centimeter scale. Based on the acceleration within a laser-driven plasma wave, fields within the wave reach the order of 100 GV/m where conventional accelerators are restricted to about 100 MV/m. Beside the acceleration fields, also the focusing fields within the plasma wave reach similar values and give rise to many orders of magnitude higher charge densities of such beams.

The unique qualities of plasma-accelerated beams not only open up a wide field of novel applications, but the according reduction in size and potentially also cost of such accelerators promises to afford a boost in the availability of accelerated beams also in smaller laboratories. Electron beams, e.g., can be used to generate undulator radiation in the keV regime, which is instrumental in protein crystallography as well as in high-resolution medical diagnostics. Laser generated electron beams could thus potentially move these applications from large-scale facilities into small scale laboratories and hospitals.

The scope of this thesis is the study of transport and focusing properties of laser-generated charged particle beams. Several key beam transport elements are examined and improved. All these elements are in principle well known from classical accelerators, however, their application with ultradense laser-generated beams requires an adapted design. This partly results from the non-negligible free vacuum expansion of an electron beam dominated by space charge effects. In this regime, the energy of the space charge field per electron can reach up to 10% of the rest energy, which is much larger than for conventionally acceler-

ated electron beams. Most commonly used tracking codes applied here and in the field of conventional particle acceleration are found to exhibit substantial deficits in the applied models for treating space charge in the regime of laser acceleration. The ensuing artifacts stem from common approximations, which are adequate to rather dilute conventional beams, but which prove inapplicable for dense laser-generated beams. These problems predominantly arise from the chosen algorithm for Lorentz transformations, inadequate initial conditions and non negligible retardation artifacts. A part of this thesis consists of the development of a calculation approach for space charge effects based on Point-To-Point particle interactions, which is a more adequate ansatz. It can hence be applied to validate further calculation approaches, e.g. Poisson solvers. Understanding the new quality of space-charge is only one mandatory aspect for many applications of laser-accelerated electron beams.

Also novel, high-gradient beam optical devices are needed for focusing these beams, hence we report on the development, characterization and testing of miniature magnetic quadrupole devices. The miniaturization of these devices in general introduces higher field gradients, but consequently also stronger field distortions than present in conventional devices. Presented is a new method for detecting distorting magnetic field aberrations, based on a simple Hall probe measurement. They can then be compensated online by adjusting the permanent magnet poles in the device in a controlled way. The characterization results of these devices have been validated at the Mainz Microtron (MAMI) electron accelerator which delivers a high quality electron beam. An experiment performed at the Z-Petawatt laser system at the Sandia National Laboratories resulted in the first successful magnetic focusing of a laser-accelerated proton beam. Herefore, the new miniature quadrupole devices have been applied.

As outlined above, laser driven electron acceleration holds promise for a quantum leap in producing dense, short relativistic electron bunches, which are a prerequisite for driving a free electron laser, which has been prominently demonstrated in the FLASH and LCLS [6] facilities. By virtue of their substantially higher current density and compactness in producing them, laser accelerated beams could greatly reduce the overall size of the required magnetic undulator structures. The first discussion of all relevant aspects concerning a laser driven Free Electron Laser (FEL) is presented.

The required length of the undulator for operating an FEL depends on the average electron charge density while propagating through the undulator. With the intrinsic high phase-space density of laser-driven beams, the undulator length could be further reduced by keeping the average beams size to a minimum. For this reason, a new undulator concept was developed on the basis of miniature magnetic quadrupole lenses, which yields strong intrinsic focusing properties.

Following the theoretical concept, first steps for an experimental realization have been undertaken, starting with the construction and experimental testing of a miniature undulator device.

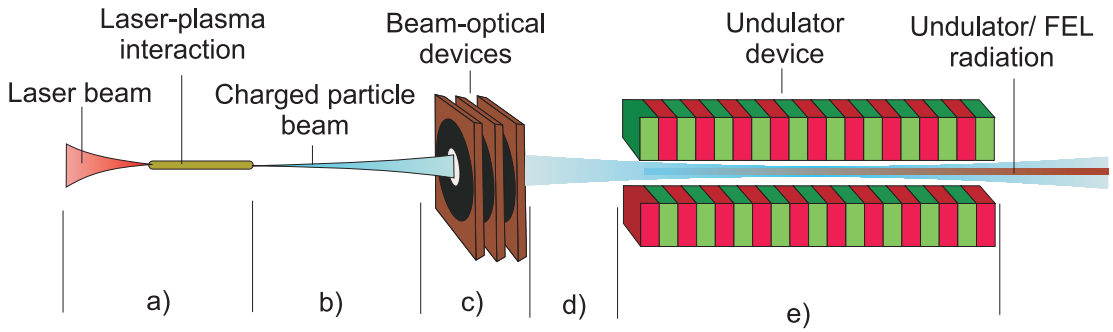

Figure 1.1: Schematic of a laser-driven undulator/FEL photon source: (a) A laser beam is focused into a gas-filled capillary, where laser-plasma interaction leads to electron acceleration. (b) The electron bunch at a high charge density propagates in vacuum under the influence of space-charge effects. In (c) and (d), the electron bunch is focused using quadrupole devices. (e) The electron bunch within an undulator device leads to emission of synchrotron radiation, i.e. undulator/FEL radiation.

The structure of this thesis follows the sequence of beam transport elements as shown in Fig. 1.1: (a) Introduction into laser acceleration (chapter 2). (b) Space charge effects during vacuum expansion[1]. (c) Miniature magnetic quadrupole devices[2]. (d) Beside the transport of electron beams, the quadrupole devices were successfully applied for focusing ion beams[3]. (e) Aspects concerning the dipole-based test undulator[4], the Free-Electron-Laser[5] and the Quadrupole Undulator[6].

[1]Space charge is introduced in chapter 3. Section 3.5 introduces to the publication in chapter I.

[2]Charged particle beam transport is introduced in chapter 4. Section 4.4 introduces to the publication in chapter II.

[3]The publication concerning ion focusing in chapter III is introduced by section 4.5.

[4]Undulators and undulator radiation is introduced in chapter 5. Section 5.3 introduces to the publication in chapter IV.

[5]The Free Electron Laser is introduced in chapter 6. Section 6.3 introduces to the publication in chapter V.

[6]The publication of the quadrupole undulator is presented in chapter VI and introduced in section 6.4.

Chapter 2

Foundations of Laser Particle Acceleration

The ever increasing laser intensities as delivered by modern short-pulse laser facilities in the range between 10^{19} and 10^{22} W/cm^2 push the development of laser-driven particle acceleration. In principle, this suggests much more compact accelerators for certain applications. Ultra-high fields allow to reach GeV electron beam energies within cm scales, whereas conventional particle accelerators for the same energies are typically hundreds of meters long. Moreover, a number of important properties of the resulting particle beams significantly differ from conventional approaches. An example are ultra-high transverse field gradients in addition to the longitudinal ones, which lead to strong focusing of the electron beam during acceleration. The result is an electron beam in a new space-charge dominated regime[1] regime.

The major part of this cumulative thesis relates to the treatment of particle beams after the acceleration process. The required beam transport elements are in principle well known from conventional accelerator physics. However, the different properties of the beam require an enhanced understanding of these elements, thus motivating the subject of this thesis.

This chapter introduces to basic aspects of laser particle acceleration in order to give an impression of the fundamental differences in comparison with conventional concepts. First, the electromagnetic field of the laser is presented as a solution to the Maxwell equations, followed by a description of the electron motion in the electromagnetic field, which is the first principal interaction considered here. Subsequently, the plasma generated by the interaction of the laser beam with a gas target is introduced with its relevant properties, since it acts as a field rectifier that transforms the fast oscillating, transverse laser fields into quasi static, longitudinal acceleration fields. With this basis, we can finally proceed to the introduction of laser-driven electron and ion acceleration.

[1]Space charge domination of an electron bunch was determined to be at ratios of the field energy to rest energy of values larger than 1%. This is described in chapter 3.

2.1 Laser-Electron-Interaction

Before we describe the microscopic interaction of an electron with a strong laser field, we will briefly discuss the latter's properties. The electromagnetic fields $\vec{E}$ and $\vec{B}$ in a very basic form are described using the Maxwell equations for the spatial coordinate $\vec{x}$ at time t. These fields can be expressed using the potentials Φ and $\vec{A}$ by

$$\begin{aligned} \vec{E} =& \frac{\partial}{\partial t}\vec{A} - \vec{\nabla}\Phi \\ \vec{B} =& \vec{\nabla} \times \vec{A}. \end{aligned} \tag{2.1}$$

The application of potentials describing the fields has the advantage that $\vec{E}$ and $\vec{B}$ intrinsically fulfill the Maxwell equations. In addition, the Lorenz gauge determines Φ and $\vec{A}$ to be Lorenz-invariant, which is given by the inhomogeneous differential equations

$$\Box\vec{A} = -\mu_0\vec{j} \tag{2.2}$$

$$\Box\Phi = -\frac{\rho}{\epsilon_0} \tag{2.3}$$

with $\Box = \Delta - \frac{1}{c^2}\frac{\partial^2}{\partial t^2}$. $\vec{j}$ is the electric current density and ρ is the charge density. The absence of any charge distribution and current flux corresponds to the wave propagation in vacuum, given by the homogeneous differential equations

$$\Box\vec{A} = 0 \tag{2.4}$$

$$\Box\Phi = 0. \tag{2.5}$$

A simple solution for (2.4) is the plane wave

$$\vec{A}(\vec{x}, t) = \vec{A}_0 \cos(\omega t - \vec{k}\vec{x} + \phi) \tag{2.6}$$

with a phase offset ϕ and the wave vector $\vec{k}$ pointing into the propagation direction with the absolute value related to the wavelength by $\lambda = 2\pi/|\vec{k}|$. The angular frequency is given by $\omega = 2\pi c/\lambda = ck$.

The plane wave potential (2.6) and the Maxwell equations (2.1) yield the electric and magnetic fields

$$\begin{aligned} E(\vec{x}, t) &= \omega \cdot A_0 \sin(\omega t - \vec{k}\vec{x} + \phi) \\ B(\vec{x}, t) &= k \cdot A_0 \sin(\omega t - \vec{k}\vec{x} + \phi). \end{aligned} \tag{2.7}$$

which result in $B = E/c$ and which are the basis for solving the equation of motion for charged particles in the next section.

2.1.1 Electron Motion in an Electromagnetic Field

The action of an electromagnetic wave onto a particle of the charge e and mass m_e is given by the Lorentz force

$$m_e \frac{d}{dt}(\gamma \vec{v}) = -e(\vec{E} + \vec{v} \times \vec{B}). \tag{2.8}$$

Here, the impact of the magnetic field depends on the velocity of the electron. The laser intensities considered here are in a regime, where the electron reaches $v \approx c$ within half a laser cycle. The magnetic field cannot be neglected.

A solution for the equation of motion for the plane infinite wave in Eq. (2.7) within the laboratory frame is the famous "Figure 8" motion [7] given by

$$\begin{aligned} p_x &= a_0 \sin\phi \\ p_z &= -\frac{1}{2} a_0^2 \sin^2\phi \\ x &= \frac{c}{\omega} a_0 (cos\phi - 1) \\ z &= \frac{c}{\omega}\frac{a_0}{2}(\frac{\phi}{2} - \frac{1}{4}\sin 2\phi) \end{aligned} \tag{2.9}$$

with the periodic phase ϕ.

The normalized vector potential a_0 is given by

$$a_0 = \frac{e|\vec{E}_0|}{m_e \omega c}. \tag{2.10}$$

An electron which is initially at rest gains relativistic kinetic energies in half a laser field oscillation for values[2] of $a_0 \geq 1$. Accordingly, the laser intensity is given by

$$I = \frac{1}{2}\epsilon_0 c \vec{E}_0^2 = \frac{a_0^2}{\lambda^2[\mu m^2]} \cdot 1.37 \times 10^{18} \mathrm{W/cm^2}. \tag{2.11}$$

The range available with today's laser systems spans values of $3 < a_0 < 100$.

Next, we consider a plane wave with a finite pulse duration acting on a single electron initially at rest. After the pulse is gone, the electron is resting again but it is spatially translated as shown by the red curves in Fig. 2.1.

We now consider a spatially confined wave. The oscillating electron is pushed out of the center of the pulse with the highest field energy density. During escaping the center region, the electron runs down the *ponderomotive potential*[8]

$$U_p = \frac{e^2}{4 m_e \omega^2 \langle\gamma\rangle} |\vec{E}_0|^2 = \frac{m_e c^2}{4\langle\gamma\rangle} a_0^2, \tag{2.12}$$

[2]Note the mass dependence $\sim 1/m_e$ of a_0, which means that only electrons become relativistic and hence gain a lot of energy from the laser field at the laser intensities considered here. In order to reach $a_0 > 1$ for ions, intensities on the order of 10^{24} W/cm^2 are necessary.

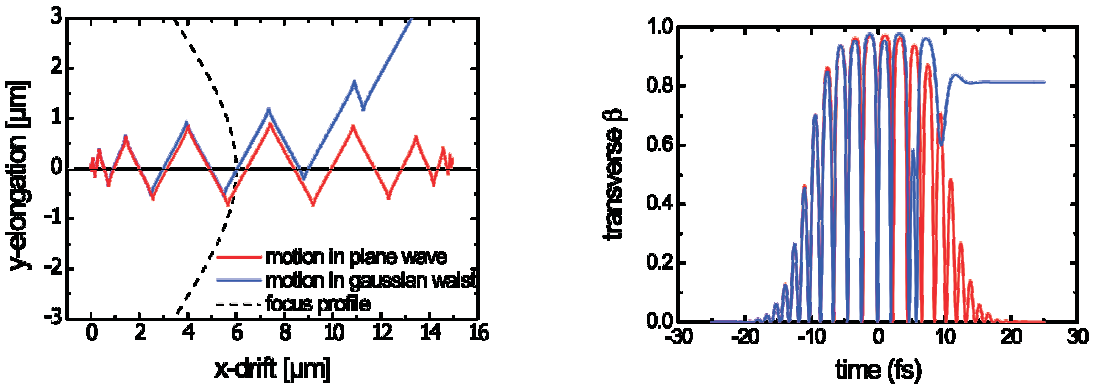

(a) "Figure 8"-trajectory (b) "Figure 8"-velocity

Figure 2.1: The solution to the equation of motion for an electron in an electromagnetic wave within the laboratory frame shown in space (a) and in velocity (b). The red curves show the results assuming a temporally Gaussion plane wave and the blue ones assume a spatial and temporal Gaussian pulse as shown by the dashed line.

within a Gaussian laser pulse between the maximum field $|\vec{E}_0|$ in the center and an infinite distance from the center. Lorentz factor $\langle\gamma\rangle$ of the electron is averaged over a laser cycle. An electron within a laser field at a potential a_0 moves at [9]

$$\langle\gamma\rangle = \sqrt{1 + a_0^2/2}. \tag{2.13}$$

The blue curves in Figs. 2.1 show the calculation of an electron running down a spatially confined Gaussion pulse with the normalized vector potential of $a_0 = 3$.

2.2 Plasma characteristics

The previous section described the acceleration of single electrons. The goal is, however, to accelerate a bunch of particles. The plasma serves as a field rectifier that transforms the fast oscillating, transverse laser fields into quasistatic, longitudinal fields. This section discusses some important plasma quantities which are required for understanding the acceleration mechanism.

2.2.1 Debye length

Having a significant amount of free charge carriers, the plasma neutralizes local disturbances. The introduction of a charge Q leads to shielding effects [10]. The charge appears virtually neutral at distances larger than the Debye length λ_D due to the screened Coulomb potential

$$\Phi_s = \frac{Q}{4\pi\epsilon_0} \exp\left(-\frac{r}{\lambda_D}\right). \tag{2.14}$$

The Debye length is given by

$$\lambda_D = \sqrt{\frac{\epsilon_0 k_B}{e^2}\left(\frac{n_e}{T_e} + \sum_{\text{ion sort}} \frac{Z_i n_i}{T_i}\right)^{-1}}, \tag{2.15}$$

where k_B is the Boltzmann constant. The electrons are characterized by their density n_e and temperature T_e. The ions are accordingly characterized by n_i and T_i and the charge state Z_i.

2.2.2 Plasma frequency

The Debye length describes the static shielding effects. In contrast, a dynamic local distortion of the quasi-neutrality leads to potential differences on the order of the perturbation strength, and consequently to strong electric fields and restoring forces. This leads to a dynamic effect exciting waves that propagate through the plasma. The corresponding *plasma frequency* is given by

$$\omega_p = \sqrt{\frac{e^2 n_e}{m\epsilon_0}} = \sqrt{\frac{e^2 n_e}{m_e \epsilon_0 \langle\gamma\rangle}}. \tag{2.16}$$

The density of $n_e = 7 \cdot 10^{18}\text{cm}^{-3}$ yields a plasma frequency of $\omega_p = 8 \cdot 10^{13}\text{s}^{-1}$ or a plasma wavelength of $\lambda_p \approx 20\ \mu\text{m}$.

Since local distortions of the plasma can be introduced by high-power laser pulses, the plasma frequency takes up an important role particularly for the electron acceleration considered next.

2.3 Electron Bunch Acceleration

The plasma frequency ω_p depends on laser and plasma parameters. Its direct impact on the refractive index shows the importance of this quantity with respect to understanding basic aspects of the laser pulse propagation within the plasma. These aspects are used to explain the electron acceleration mechanism.

2.3.1 Laser-Pulse Propagation in Plasma

Using the previous definition of a relativistic laser-pulse, we can draw simple conclusions on its interaction with the plasma. The dispersion relation for a laser pulse with relativistic intensities [11] is given by

$$\omega^2 = \tilde{\omega}_p^2 + c^2|\vec{k}|^2 \tag{2.17}$$

with $\tilde{\omega}_p^2 = \omega_p^2/\langle\gamma\rangle$. A plasma with $\omega_p > \omega$ is called overdense and underdense for $\omega_p < \omega$. It can be seen that only relativistic laser pulses are capable of propagating through overdense plasmas. Otherwise, the absolute value of the wave vector would be complex and thus lead to a reflection of the laser-pulse. The critical electron density for $\tilde{\omega}_p = \omega$ is at

$$n_e = \frac{\epsilon_0 m \langle\gamma\rangle \omega^2}{e^2}.$$

The refractive index η of a cold plasma is given by

$$\eta = \sqrt{1 - \left(\frac{\tilde{\omega}_p}{\omega}\right)^2}. \tag{2.18}$$

The group velocity of the laser pulse is $v_{g,\mathrm{Las}} = c\eta$ and the phase velocity is $v_{\phi,\mathrm{Las}} = c/\eta$. The group velocity $v_{g,\mathrm{Las}}$ equals the phase velocity of plasma wave $v_{\phi,\mathrm{PW}}$. The Lorentz factor of the propagation of the laser pulse and the plasma wave, respectively, is hence

$$\gamma_{\mathrm{Las}} = \gamma_p = \frac{\omega}{\tilde{\omega}_p} = \frac{\omega}{\omega_p}\langle\gamma\rangle. \tag{2.19}$$

Assuming a laser pulse with the wavelength $\lambda = 800$ nm and the values assumed above, we obtain $\gamma_p \approx 10$. The next sections we will deduce electron energies reaching significantly higher values than γ_p. The difference in velocity results in important implications concerning electron acceleration.

2.3.2 Laser Wakefield Acceleration

The interaction between the laser pulse propagating in the plasma and the electrons can be described using the ponderomotive force resulting in charge separation. This process drives a plasma wave with high longitudinal electric fields on short distances of a few μm. These fields co-propagate at the same velocity as the laser pulse within the plasma, as described in the section before. These propagating longitudinal fields can be used as particle acceleration fields, which is referred to as laser-wakefield acceleration (LWFA) [2]. Within the linear LWFA regime, the plasma electrons oscillate around their initial positions and hence cannot be accelerated using the propagating electric fields. In this linear case, electron acceleration would require external injection into the plasma wave at the proper phase.

For estimating the longitudinal acceleration fields, a laser pulse is assumed with a ponderomotive force

$$F_{\text{pond}} \approx F_{\text{el},\parallel} = E_{\parallel} e \tag{2.20}$$

$$= -\nabla U_p = -\frac{e^2}{4 m_e \omega^2 \langle\gamma\rangle} \nabla \vec{E}_0^2 = -\frac{m_e c^2}{4 \langle\gamma\rangle} \nabla_{\parallel} a_0^2. \tag{2.21}$$

With

$$\nabla_{\parallel} a_0^2 = 2 a_0 \frac{\partial}{\partial z} a_0 \approx 2 a_0 k_p a_0, \tag{2.22}$$

the longitudinal acceleration field can be written as

$$E_{\parallel} = -\frac{m_e c^2}{2e \langle\gamma\rangle} k_p a_0^2 = -\frac{m_e c \omega_p}{2e} \frac{a_0^2}{\langle\gamma\rangle}. \tag{2.23}$$

With Eq. (2.13), we finally obtain

$$E_{\parallel} = -\frac{m c \omega_p}{e} \frac{a_0^2}{\sqrt{1 + a_0^2/2}}. \tag{2.24}$$

The plasma frequency $\omega_p = 8 \cdot 10^{13}\ \text{s}^{-1}$ and a laser beam of $a_0 = 3$ yields acceleration fields in the order of $E_{\parallel} \approx 10^{11}$ V/m. This result certainly refers to the consideration of a single electron. If electrons are continuously injected into the plasma wave, the energy spectrum would become arbitrary broad.

2.3.3 Bubble Acceleration

LWFA is deduced from well defined plasma waves, which result from linear restoring forces. This process does not lead to a capturing of electrons. If the excitation of the plasma wave by far exceeds the linear regime, the wave front bends all the way back to the beam axis. At this point, the expelled electrons from the center of the laser pulse return to the laser axis again after half a plasma oscillation. The electron void behind the laser pulse is almost spherical in shape and is therefore called *bubble*. The Coulomb repulsion of the electrons meeting at the axis leads to electrons scattered into the bubble. This capturing process is also referred to as *wave breaking*. The highly non-linear acceleration regime is called bubble acceleration [3] and is shown in Fig. 2.2.

Once the electrons are captured, the acceleration distance is limited by relativistic electrons propagating at higher velocities than the laser pulse within the plasma (Eq. 2.18). At the center of the broken plasma wave, the fields are zero. This point marks the end of the acceleration process.

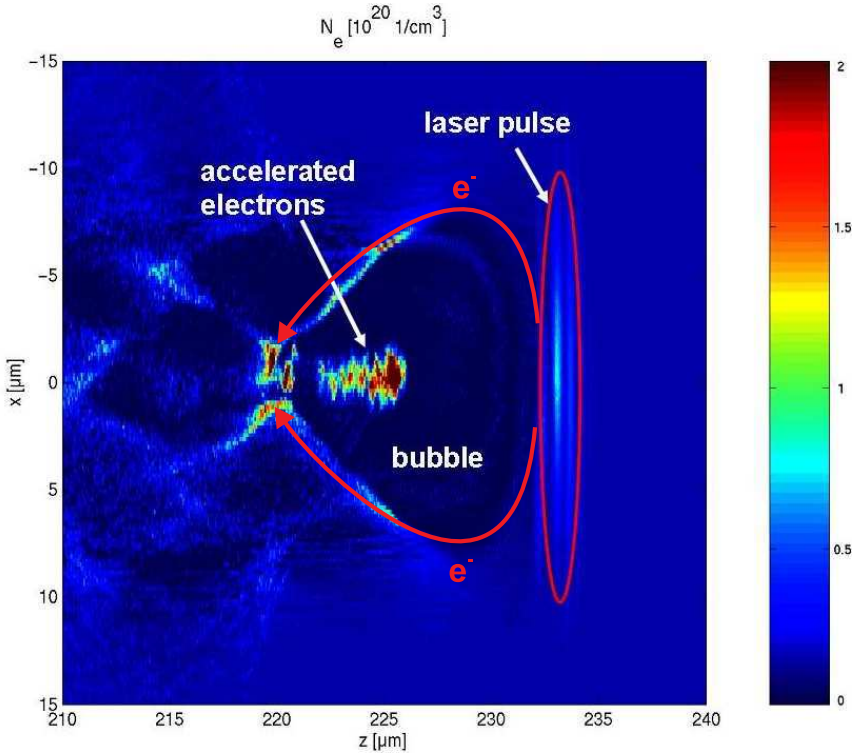

Figure 2.2: Snapshot of the electron density (in units of 10^{20} cm^{-3}) from a PIC simulation. The geometrical size of the electron-free cavity ("bubble") behind the laser spot corresponds to the plasma period, which is about 8 μm in this case (gas density $1.8 \cdot 10^{19}$ cm^{-3}). The stem of the high-energy electrons is much shorter than the plasma period.

Beyond the center, the bunch gets decelerated, which is called *dephasing*. The dephasing length L_d can be estimated taking the acceleration time $t_d = L_d/c$ and half the plasma-wave $\pi = \tilde{\omega}_p(L_D/v_p - t_d)$, which results in $L_d \approx \lambda_p \gamma_p^2$. An estimation of the electron energy gained is hence

$$W = eE_{\parallel} L_d \approx 10^9 \text{eV} \tag{2.25}$$

for the typical quantities used hitherto.

The capturing is mainly limited due to an effect called *beam loading*. The Coulomb field of the captured electrons leads to a deformation of the bubble. The electrons are kept from returning to the axis and are thus not scattered inside. Thus, beam loading is the reason for obtaining quasi-monoenergetic electron beams, since it interrupts the capturing and all electrons experience a comparable gain of kinetic energy during acceleration. However, beam loading as a result of space charge superimposes the acceleration fields within the bubble. Thus, the acceleration fields are not the same for all electrons which leads to a decline of the beam quality.

Particle-in-cell (PIC) simulations [12] show that the bubble electrons form a stem that is geometrically considerably smaller than the bubble as can be seen in Fig. 2.2. The

accelerated charge predicted by the simulations reaches values of up to 1 nC at a spatial bunch dimension of a few μm, which corresponds to beam currents in the order of 100 kA. Experiments hitherto, however, rather yield values of a few 10 pC. The reason for this discrepancy is currently in the focus of ongoing research.

Laser based electron acceleration has been experimentally demonstrated at various laser facilities up to an energy of about 1 GeV [4, 5, 13]. A normalized emittance of 1 mm mrad was deduced from the experimentally determined beam divergence and the source size as inferred from PIC simulations.

The amount of the longitudinal acceleration field yields the fundamental difference between laser-acceleration and conventional acceleration. The latter is principally limited by the Kilpatrick criterion for high voltage vacuum sparking [14]. Radio frequency accelerators experience a principal limit for the high voltage stability of acceleration structures of $\approx$ 100 MV/m. Modern super-conducting acceleration cavities as presently applied at DESY [15] reach 30 MV/m. Laser-acceleration fields are typically in the order of TV/m [Eq. (2.24)], which allows a reduction of the cavity length by at least 5 orders of magnitude. Acceleration distances of the order of kilometers can be reduced to the cm regime, which leads to a miniaturization of the accelerator device.

In addition to the miniaturization, laser-plasma accelerated electron beams possess different properties. The bubble shape leads to transverse focusing fields with gradients in the order of the longitudinal acceleration fields. These transverse fields are also unreachable by conventional accelerators and thus, laser particle acceleration is capable of reaching space charge fields in a new regime.

The resulting space charge effects after extraction of the beam into vacuum have to be studied in a way which so far was not necessary in conjunction with conventional acceleration. These studies are presented in this thesis.

2.4 Ion Acceleration

The ponderomotive force delivered by laser systems widely available today are capable of accelerating electrons to relativistic energies in vacuum. This is not the case with ions. Using Eq. (2.10) for protons and replacing the electron mass m_e by the proton mass m_p results in enormous requirements of the laser intensity, namely

$$I = \frac{a_0^2}{\lambda^2[\mu\mathrm{m}^2]} \cdot 4.6 \times 10^{24}\mathrm{W/cm}^2. \tag{2.26}$$

The Extreme Light Infrastructure (ELI) [16] is a laser project aiming at these intensities within the next years. For current laser systems, however, the ions are too heavy to follow the oscillations of the laser field. The solution here is the acceleration of electrons as a basis for transferring energy to the ions which are accelerated in a field due to charge separation between electrons and ions.

2.4.1 Target Normal Sheath Ion Acceleration

The target normal sheath acceleration (TNSA) [17, 18, 19] involves the irradiation of a foil target with a thickness in the μm range using a multi TW laser pulse. The acceleration of ions takes place within a quasi-static electric field, spanned between an ionic background and laser-accelerated electrons. The main aspects of this process will be explained in the following.

The energy of the laser pulse is predominantly transferred to the electrons due to the ponderomotive force. The foil is in solid state density and thus cannot be penetrated by the laser pulse. The resulting electron acceleration efficiency is poor compared to the case where the laser pulse penetrates the target, as it was the case with electron acceleration as described in the previous section.

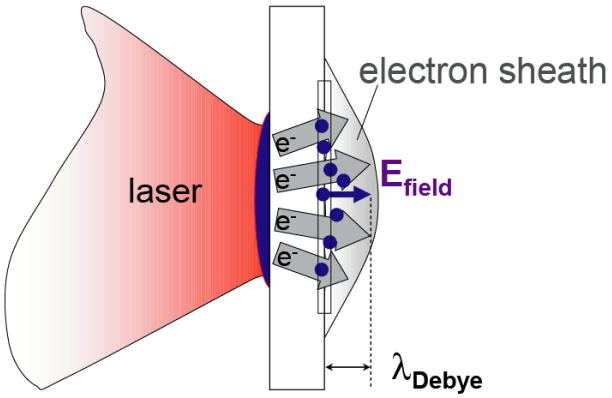

Figure 2.3: Target-normal-sheath-acceleration (TNSA) mechanism is shown schematically. A laser pulse is focused onto a foil of few 10 μm thickness. Electrons (e^-) are ponderomotively accelerated within the pre-plasma at the front side (on the left-hand side) of the foil and leaving it at the rear side. An electrostatic field is built up within a distance of the hot electron Debye-Length λ_D between the ionic background inside the foil and these electrons, accelerating ions from the rear side of the foil.

At the rear side of the foil, these electrons are in a thermal equilibrium, building up a quasi-static electron sheath. The sheath and the mirror charge within the foil generate the acceleration field for the ions.

The electrons accelerated within the pre-plasma possess a thermal energy distribution with a temperature of [20]

$$k_B T_e = m_e c^2 \left(\sqrt{1 + a_0^2} - 1 \right)$$

and are called *hot electrons*.

The electrostatic acceleration field for TNSA leads to ion energies of tens of MeV for currently available laser systems at an acceleration distance in the range of the Debye length, which is in the order of 1 μm. The comparison to conventional ion acceleration yields an emittance of the ion beam at much smaller values although the spatial charge density is much larger. The reason is the smooth curvature of the electron sheath as schematically shown in Fig. 2.3, perpendicular to which the ions are accelerated. The extraction angle of the ions is highly correlated with their initial position on the surface of the foil, which leads to small emittance values by definition.

However, the curvature of the electron sheath also leads to an ion beam at much higher divergence as obtained from conventional acceleration approaches. The concepts for reducing the divergence involve *mass-limited targets* with spherical shape at few μm in diameter [21] or shaped targets [22]. The principle disadvantages of TNSA is a large energy spread and little energy conversion efficiency. An acceleration scheme performing better in this respect is the Radiation Pressure Acceleration as introduced in the next section.

2.4.2 Radiation Pressure Acceleration

The radiation pressure acceleration regime (RPA) promises fundamental advantages over TNSA such as monoenergetic ion beams and a much higher energy conversion efficiency. Concerning laser ion acceleration, RPA is the best of all approaches known so far, but is extremely demanding on the temporal contrast of the drive laser pulses, since targets with thicknesses on the order of a few nm have to stay intact until the peak of the laser pulse arrives. Since RPA is not subject of this thesis, the description is kept brief.

Similar to TNSA, the RPA mechanism is also based on the interaction of a relativistic laser pulse with a solid target, pushing electrons in the forward direction [23, 24, 25, 26]. In the case of RPA, however, the thickness of the foil target is in the nm range [27] (e.g. Diamond Like Carbon (DLC)). The skin depth is larger than the thickness of the foil. Hence, in spite of the the foil in solid state density, which usually leads to reflection, the leaser pulse can yet penetrate the target and pushes all electrons to the front leading to a shift of the electron density with respect to the ion background. This shift one hand causes strong acceleration fields for the ions on the but also keeps space charge fields low on the other hand since most electrons remain inside the ionic background. The circular polarization of the laser pulse leads to a smooth momentum transfer from the laser pulse to the electron population without heating it and subsequently causing a strong bipolar expansion of the foil, as would be the case with linear polarization.

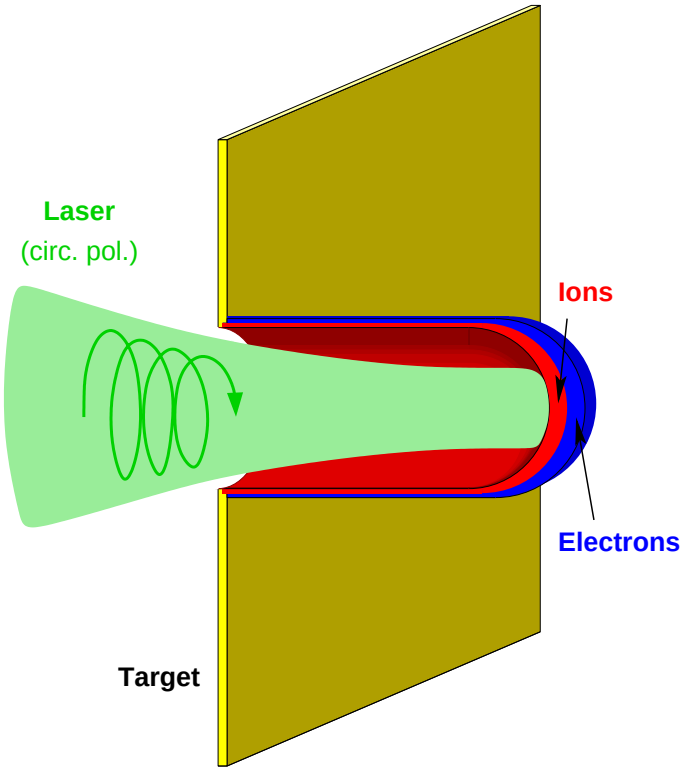

Figure 2.4: The Radiation Pressure Acceleration scheme (RPA) is shown schematically. An ultra-thin nm foil target is irradiated by a circularly polarized laser pulse ionizing all atoms. The electrons are pushed out of the nm-thick solid material and are accelerated. The constant energy transfer of the laser pulse to the electrons and the restoring forces of the ions lead to the acceleration of the target as a whole. [29].

The steady light pressure acting on the electrons is at an equilibrium with the restoring force of the ionic background. Consequently, the irradiated part of target is accelerated as a whole as shown in Fig. 2.4. The electron distribution and ion distribution shifted with respect to each other leads to a rotation in the longitudinal phase space during acceleration [28] and thus, to a compression of the phase space volume as it is also known from conventional acceleration. In a purely one dimensional scenario, all ions obtain similar energies and thus, a high efficiency for ion acceleration into a monochromatic spectrum can be achieved. In three dimensions, the acceleration is strongest in the center of the laser pulse, leading to a relatively poor overall efficiency for ions with the highest energy and best collimation. Therefore, a lot of research goes into the development of strategies that counteract this effect, such as flat-top laser intensity profiles or foils shaped to counterbalance the laser imprint, and hence strongly enhance the phase-space density of such beams [29]. This possibility constitutes one of the prime motivations for this thesis, since such beams will truly exploit the full potential of the beam optics developed here. High expectations for this novel scheme to efficiently deliver high-quality GeV ion beams have

sparked a vigorous competition among different research groups. The first observation of RPA signatures could be achieved in this group [30].

Moreover, the new method for characterizing and tuning beam optical devices presented in this thesis allows a proper manipulation and transport which currently gives our group a distinct advantage over our competitors.

Chapter 3

Space Charge Effects

The laser electron acceleration yields particle beams with specific properties as described in the chapter before, among which the beam current density significantly differs from conventional particle acceleration. As a consequence, space charge effects play an important role, the understanding of which is a prerequisite for the realization of many experiments, such as Free-Electron-Lasers. Particularly for laser-accelerated electron beams, these effects have to be understood in detail.

Although the space charge effect is merely based on the Coulomb interaction, it is a many-particle problem which can hardly be treated analytically. Besides introducing to the numerical calculations, this chapter also aims at presenting a visual impression of the dynamics of the intra-beam interaction of charged particles arguing with simple conserved quantities. Next, retardation effects in the context of space charge calculations are introduced, causing artifacts which cannot be neglected for high current electron beams. The minimization of of these artifacts is a topic of this thesis and will be introduced finally.

3.1 Numerical Calculation Methods

All numerical simulation approaches considered here are based on an ensemble of discrete particles[1] which are tracked through the simulation volume in the time domain and in a 6D phase space. This implies that every particle is characterized by its spatial position and momentum at a given point in time within the calculation frame of reference. It is thus only one 6D phase space coordinate for every particle which is used to determine the following coordinate at the next discrete time step[2].

[1] On could consider particle densities instead of discrete particles.

[2] The alternative would imply taking into account the 4D trajectory rather than the 6D phase space coordinate. These 4D approaches (also sometimes called "book keeping“) are not very common, also because computer performance presently does not allow for their treatment in an acceptable amount of time. 4D approaches are not considered here.

Einstein postulates that the laws of physics are the same for all observers in uniform motion (frame of reference) relative to one another. Accordingly, the frame of reference, where the equation of motion for particle i is solved, is further on called the *calculation frame of reference*. All frames considered here move in the same *longitudinal* direction with different velocities as required when applying the special theory of relativity. The equation of motion is given by

$$m_e \frac{d}{dt} \gamma_i \vec{v}_i = \vec{F} = -e(\vec{E}_i + \vec{v}_i \times \vec{B}_i) \tag{3.1}$$

with the rest mass m_e, the Lorentz factor γ_i, the velocity v_i, the charge e, the force $\vec{F}$, the electric field $\vec{E}$ and the magnetic field $\vec{B}$.

The large number of real particles calls for grouping many electrons into simulation particles, so called *macro-particles*, for reasons of computational efficiency. n_p particles form a macro particle having n_p-times the charge, thus experiences n_p-times the force, and n_p-times the mass m_e. The particle's dynamics

$$\frac{d}{dt} \gamma \vec{v} = \frac{n_p \vec{F}}{n_p m_e}$$

remains unchanged. This model certainly corresponds to n_p actual particles which are forced on a constant distance. This constraint leads to artifacts which have to be minimized using a convergence test. From this point on, we refer to the total number of particles n used in a simulation rather than referring to the number n_p per macro particle. Convergence can be identified using values such as the total energy (kinetic energy and field energy) of the system. The consideration of the mere vacuum expansion of high current beams usually only requires a few thousand macro particles[3]. Many more macro particles are required for example when evaluating the emittance of a beam which is focused. This scenario might require specific calculation methods, which yield appropriate scalings of the calculation time depending on the number n of particles considered. Here, two methods are introduced, the point-to-point interaction, where the calculation time scales like n^2 and the Poisson solver, where it almost linearly scales with n.

3.1.1 Point-to-Point Interaction

The calculation of space charge is examined here using a point-to-point interaction (PPI) model according to [31, 32]. A prominent implementation is the GPT code [33]. The frame of reference commonly used with PPI codes is the laboratory frame.

The electromagnetic fields are calculated relativistically, where radiation effects are neglected and retardation is treated in accordance with the constant velocity approximation.

[3]Note that the force $\vec{F}$ scales with n_p, which leads to a convergence of the system particularly when considering the electromagnetic field, even though the number of macro particles is many orders of magnitude smaller than the number of real particles.

For obtaining $\vec{E}_i$ and $\vec{B}_i$ required to solve the equations of motion (3.1), we first consider the Coulomb field of particle j acting on i in the rest frame of j given by

$$\vec{E'}_{j\to i} = \frac{Q\vec{r'}_{ji}}{4\pi\epsilon_0|\vec{r'}_{ji}|^3}, \tag{3.2}$$

with Q being the charge of the macro particle and

$$\vec{r'}_{ji} = \vec{r}_{ji} + \frac{\gamma_j^2}{\gamma_j+1}(\vec{r}_{ji}\vec{\beta}_j)\vec{\beta}_j = \vec{r'}_i - \vec{r'}_j \tag{3.3}$$

being the distance between the particles i and j in the rest frame of j moving at the normalized velocity $\vec{\beta}_j = \vec{v}_j/c$ within the calculation frame of reference.

The Lorentz transformation of the Coulomb field of particle j acting on i into the calculation frame of reference is given by

$$\vec{E}_{j\to i} = \gamma_j\left[\vec{E}'_{j\to i} - \frac{\gamma_j}{\gamma_j+1}(\vec{\beta}_j\vec{E}'_{j\to i})\vec{\beta}_j\right], \tag{3.4}$$

$$\vec{B}_{j\to i} = \frac{\gamma_j\vec{\beta}_j\times\vec{E}'_{j\to i}}{c}. \tag{3.5}$$

Coulomb Singularity

The Coulomb potential of Eq. (3.2) has the well known singularity at $|\vec{r'}_{ji}| \to 0$. If the time steps are chosen too large and of constant values, there is the chance that two particles i and j approach much closer than they would in reality. This incidence results in a gain of total energy of the system, which is a numerical artifact also referred to as *heating*.

Two ways are discussed which can be used either separately or in combination to prevent the system from heating.

Macro Particle Radius Problems due to the singularity of the Coulomb potential can be reduced considering each macro particle as a cloud of "real" particles. A radius r_0 is introduced for determining an overlap of the clouds. Eq. (3.2) is extended according to

$$\vec{E}'_{j\to i} = \frac{Q\vec{r'}_{ji}}{4\pi\epsilon_0}\cdot\begin{cases} |\vec{r'}_{ji}|^{-3} & : \quad |\vec{r'}_{ji}| > r_0 \\ r_0^{-3} & : \quad |\vec{r'}_{ji}| < r_0 \end{cases} \tag{3.6}$$

with a reasonable choice for r_0 which is the typical distance between two macro particles.

Adaptive Time Steps The application of adaptive time steps is an elegant way preventing the simulated system from heating. The evolution of the 6D phase space coordinate is observed, allowing for changes from step to step in time only within a specific radius.

Hence, this is an upper boundary for both, the change in momentum and the change of the spatial position. The simulation code steadily tries to increase the size of the steps for minimizing the total calculation time. Heating of the system is identified if the radius is exceeded. In this case, the calculation of the time step is repeated using a smaller step size.

3.1.2 Poisson Solver

The Poisson solver evaluates electrostatic fields in the mean rest frame of the bunch. Prominent examples for implementations are code packages GPT [33] and ASTRA [34].

For each time step, the electrostatic potential is solved on the grid points of a calculation mesh. Modern solvers utilize adaptive grids such that the resolution is enhanced where charges are accumulated. Relative motions within the mean rest frame are neglected since magnetic fields cannot be taken into account using this method. The transformation of the electrostatic field into the calculation frame of reference, which usually is the laboratory frame, is performed using Eq. (3.5).

A solver requires a number of assumptions and technical details, which are not introduced in detail here. This fact, however, requires the solver's calculation result to be carefully cross-checked with calculation approaches based on more fundamental principles. For example, the PPI method only utilizes the Coulomb field and can thus be used for validation. As already mentioned before, specific space charge calculation scenarios require $n \approx 10^5$ for converging safely. Since the Poisson solver almost linearly scales with n, this method might be without an alternative.

In the course of this thesis, three causes for artifacts were identified within prominent solver codes such as GPT:

- The approximation of the Lorenz transformation performed in every time step is inadequate for large relative longitudinal velocity components.
- The equations of motion solved in the mean rest frame only requires the Lorentz transformation ones instead of a transformation in every time step.
- The initial conditions have to be considered correctly. Assumptions for the bunch history regarding the acceleration process have to be made.

These issues are discussed in the publication of chapter I in more detail.

3.2 Symmetry Approximations

This section intends to help the reader obtaining an intuitive perception of the process during the beam expansion due to space charge effects. This picture can be useful when evaluating results of numerical simulations.

The two frames of reference considered here are the laboratory frame, where all beam transfer elements are at rest, and the mean rest frame of the bunch, where the average longitudinal velocity of all particles is zero. The initial spatial particle distribution is assumed to be point-symmetric in both frames of reference. The violations of this symmetry discussed here are due to two different reasons:

- A bunch with particles moving with respect to each other in longitudinal direction in principle cannot be point-symmetric in both frames of reference. The reason can be found in the *Lorentz transformation* as discussed in the publication in chapter I.
- The symmetry is violated for *geometrical reasons* due to the divergence of the bunch as discussed in the following.

The violation for the latter reason, geometrical one, clearly dominating over violations due to the Lorentz transformation. Hence, the violation due to the Lorentz transformation is neglected in the following discussion.

3.2.1 Geometrical Bunch Prolongation

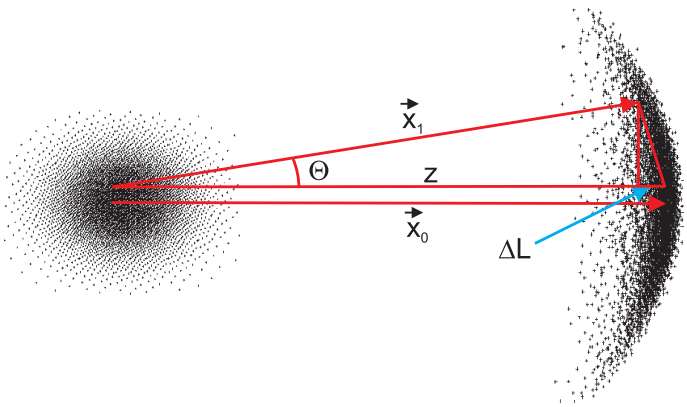

Figure 3.1: The evolution of a diverging particle bunch is shown schematically within the laboratory frame neglecting space charge. We consider two particles, one propagating on-axis along $\vec{x}_0$ and another one propagating along $\vec{x}_1$ at an angle of Θ.

We will first consider a case, where space charge is neglected and the bunch diverges at an angle Θ. In this simple and prominent case, the initial spatial point symmetry will be violated during propagation.

In Fig. 3.1, we schematically consider the case of geometrical prolongation of a bunch longitudinally propagating in the z direction. The bunch initially is point symmetric in space having a finite divergence without energy spread and neglecting space charge. A first particle which is initially located on axis propagates along the trajectory $\vec{x}_0$. A second particle propagates (at the same velocity) along the trajectory $\vec{x}_1$ at an angle Θ. The contribution to the bunch prolongation of these particles is $\Delta L \approx z \cdot \Theta^2/2$. This bunch loses the initial point-symmetry in space, since the initial divergence introduces a momentum distribution which is not any longer point-symmetric.

3.2.2 Self Acceleration

After having discussed a diverging bunch without considering space charge effects, we now discuss an initially cold bunch, i.e. with zero divergence and zero emittance[4] as shown in Table 3.1. This time, we consider the influence of space charge.

σ_x	σ_y	σ_z	γ^*	Q	ϵ	σ'
$1\mu m$	$1\mu m$	$1\mu m$	300	1 nC	0	0

Table 3.1: Initial configuration of a beam in the laboratory frame with a Gaussian particle density distribution of the energy γ^*, the emittance ϵ and divergence σ'.

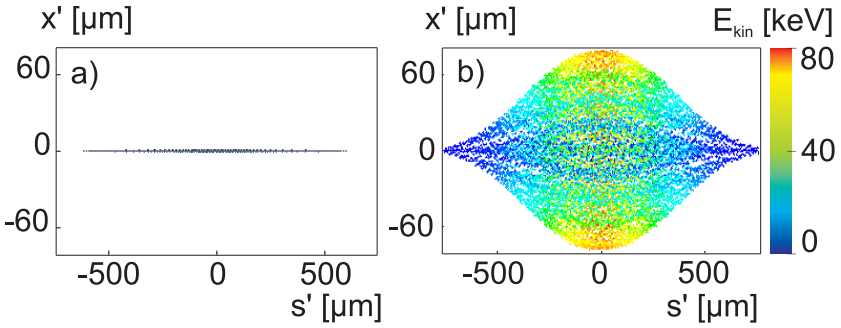

Figure 3.2: Evolution of a cold bunch as in Table 3.1 in its mean rest frame remains point-symmetric as shown schematically. (a) shows the initial state at the time $t'_0 = 0$, (b) at a later time t'_1. The color coding indicates the energy distribution.

The action of the Coulomb force is point-symmetric. As already mentioned, the spatial bunch density distribution and the momentum distribution in the mean rest frame of the bunch is assumed to be point-symmetric in both frames of reference.

We first move from the laboratory frame of reference into the mean rest frame of the bunch propagating with γ^*. The Lorentz transformation requires 4D trajectories for every

[4]The terms divergence and emittance are introduced in chapter 4.

particle. As already mentioned, the calculation approaches usually applied only yield coordinates in the 6D phase space. The Lorentz transformation thus has to be approximated.

A common and simple approximation[5] is $\sigma'_x = \sigma_x$, $\sigma'_y = \sigma_y$ and $\sigma'_z = \gamma^* \sigma_z$. This transformation implies that the spatial density distribution and momentum distribution remain point-symmetric for all times in all frames of reference.

The calculation of the evolution of the spatial density distribution in the mean rest frame of the bunch is shown in Fig. 3.2(a) initially and in Fig. 3.2(b) after some expansion. The Coulomb expansion does not violate the point-symmetry.

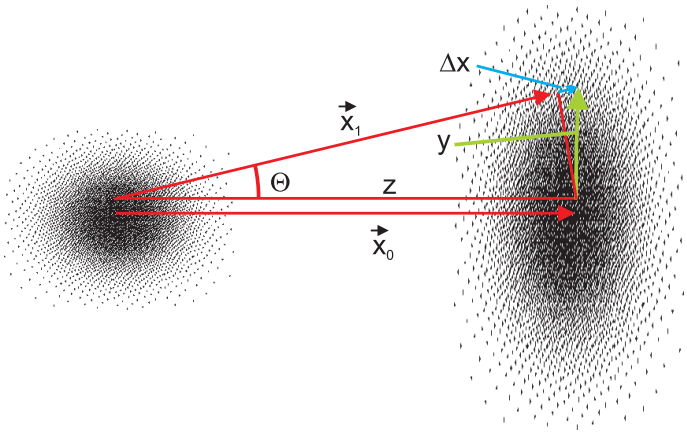

Figure 3.3: Space charge driven evolution of an initially cold bunch is shown schematically in the laboratory frame. As in Fig. 3.1, we consider two particles, one propagating on-axis along the trajectory $\vec{x}_0$ and one propagating along the trajectory $\vec{x}_1$ at an angle Θ. The distributions correspond to the schematic representations in the mean rest frame shown in Fig. 3.2.

Moving back to the laboratory frame, the spatial symmetry is conserved as schematically shown in Fig. 3.3, in contrast to Fig. 3.1. After the space-charge driven expansion, the electron propagating along $\vec{x}_1$ with a finite divergence $\theta > 0$ has to propagate at least[6] the distance $x_1 > x_0 + \Delta x$ within the same time as the electron on axis ($\theta = 0$) propagates the distance x_0. For a beam at ultra-relativistic velocities ($\gamma > 100$, $v \approx c$), additional velocity components result in a large gain of kinetic energy. However, neither does the geometrical center of the bunch change the state of motion nor does the system *as a whole* violate energy and momentum conservation, as shown in the next section.

[5]This approximation neglects the violation due to the Lorentz transformation and is commonly applied among a majority of simulation codes such as GPT. A more accurate approximation is discussed in the corresponding publication in chapter I.

[6]The real trajectory is curved, which enhances the difference in the propagation distance.

3.3 Self Acceleration and the Conservation of Energy and Momentum

The origin of the gain of kinetic energy can be found in the averaged potential field energy per electron in the mean rest frame of the electron bunch [31]

$$u'_f = \frac{1}{4\pi\epsilon_0 N}\sum_{i=2}^{N}\sum_{j=1}^{i-1}\frac{q_i q_j}{|\vec{r'}_i - \vec{r'}_j|} = \frac{\epsilon_0}{2N}\int |\vec{E}(\vec{r'})|^2 d^3r', \tag{3.7}$$

where N is the number of charged particles considered and q_i is the charge of the particle i at the position $\vec{r'}_i$. The normalized field energy $u'_n = u'_f/m_e c^2$ is a good indication for identifying the space charge regime of the electron bunch considered. A bunch can be considered space charge dominated for $u'_n > 1\%$[7].

The equivalence of energy and mass $u'_f = m_f c^2$ allows the treatment of the space charge field energy u_f as an effective field mass m_f. The average energy in the electrons' mean rest frame is

$$u' = m_e c^2 + u'_f = (m_e + m_f)c^2. \tag{3.8}$$

The potential energy is at its maximum at its release into vacuum after its acceleration. An effective total mass per electron is given by

$$m' = m_e + m_f, \tag{3.9}$$

where m_f is the effective field mass.

The expansion of the bunch leads to a reduced space charge field and thus to a reduced effective mass. As relaxation of the space-charge field corresponds to $m_f = 0$, the total energy $u' = m'c^2 = \gamma' m_e c^2$ is conserved for

$$\gamma' = 1 + \frac{m_f}{m_e}. \tag{3.10}$$

The potential energy per electron in the case considered is 50 keV, which is 10% of the electron's rest energy.

The transformation into the laboratory frame using Eq. (3.9) yields the total energy of the bunch

$$u = \gamma^* m' c^2 = \gamma^* m_e c^2 \left(1 + \frac{m_f}{m_e}\right) \tag{3.11}$$

directly after its acceleration. After a complete relaxation, Eq. (3.10) yields $u = \gamma^*\gamma' m_e c^2 = \gamma m_e c^2$ and thus

$$\gamma = \gamma^*\gamma'. \tag{3.12}$$

[7] It was found from a series of simulations that charge densities of $u'_n > 1\%$ require careful studies of the of space charge effects.

The average gain of kinetic energy corresponds to the ratio of field energy and rest energy of the electron. The same approach yields the longitudinal momentum gain of the electron bunch propagating at the velocity $v^* = \beta^* c$, while conserving the total momentum of the system

$$p_z = \gamma^* m' v^*, \tag{3.13}$$

for the bunch right after acceleration and

$$p_z = \gamma' \gamma^* m_e v^*, \tag{3.14}$$

after complete relaxation.

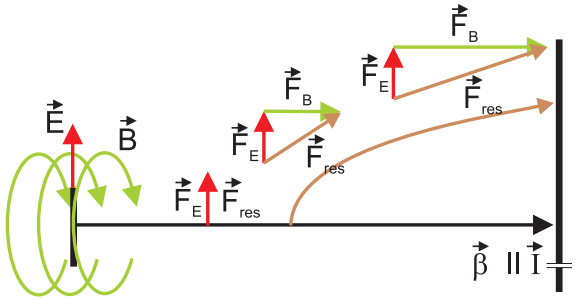

Figure 3.4: Self acceleration fields for particles of a bunch propagating in the laboratory frame. This scheme as an example considers particles which are located within the bunch. On the left, there is the electrostatic field pointing towards the transverse direction, which is the dominant direction of the electrostatic field due to the Lorentz contraction. The magnetic field is a consequence of the beam current. The further the electrons depart from the beam axis, the more kinetic energy they obtain from the electric field and at the same time, the greater the force in the forward direction which they experience from the magnetic field.

The illustrative impression of the acceleration process in the laboratory frame can be obtained by regarding the electromagnetic fields. The major electric field component results in a transverse acceleration as shown in Fig. 3.4. The transverse electric field component of $\vec{E}$ dominates over the longitudinal component as a result of the Lorentz transformation $E_x = \gamma^* E'_x$ and $E_z = E'_z$.

The transformation from the rest frame into the laboratory frame introduces an azimuthal magnetic field. The mainly transverse velocity component from the acceleration by the electric field leads to a longitudinal velocity component due to the Lorentz force.

This fact allows for an interesting and fundamental conclusion. The magnetic field is a result of the Lorentz transformation from the mean rest frame to the laboratory frame and *assures* the center of mass at the position $\vec{x}_{\mathrm{cm}}$ moving at constant velocity $\vec{v}_{\mathrm{mean}}$ in any

frame of reference[8]. The center of mass is written as

$$\vec{x}_{\mathrm{cm}}(t) = \frac{\sum_i \gamma_i(t)\vec{x}_i(t)}{\sum_i \gamma_i(t)} = \vec{x}_{s0} + \vec{v}_{\mathrm{mean}}t. \tag{3.15}$$

3.4 Retardation Artifacts

The PPI calculation method principally requires the approximation of retardation effects. This approximation can become questionable if the state of motion changes on short time scales. The electrons within a space charge dominated bunch are exposed to large accelerations and hence artifacts due to the constant velocity approximation are not negligible. In the following, we will examine the quantities on which artifacts depend on.

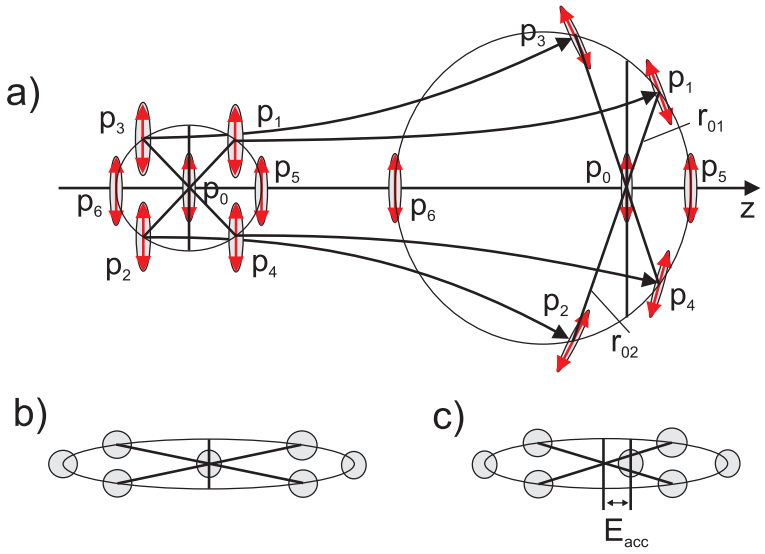

Figure 3.5: Electrons p_0 - p_6 are shown schematically within the laboratory frame. p_0 is the symmetry particle. The left hand side of (a) shows the laboratory frame with the initial beam configuration at a time t_0 and after some propagation on the right hand side at the time t_2. The electrons are shown with the electrostatic fields contracted as a result of the quasi static approximation in Eq. (3.4). (b) shows the symmetric particle positions of the 4D trajectory in the mean rest frame at the time t_1. (c) shows the retarded positions at t_1 in the mean rest frame estimated from the 6D phase space coordinate using the constant velocity approximation. This approximation results in an acceleration field E_{acc}, which is a retardation artifact.

[8]Strictly speaking, the center of mass of only the particles (electrons) does not exactly move at constant velocity. It is the total center of mass moving at constant velocity, which also includes the effective mass of the electromagnetic field m_f.

Fig. 3.5 schematically shows the electrons p_0 to p_6 within a space charge dominated bunch expansion. The center particle p_0 is the symmetry particle and also the center of mass. The distance between the particles i and j is r_{ij}. The center of mass as in Eq. (3.15) and the symmetry condition determine relative distances of particles located opposite to each other, e.g. $r_{01} = \gamma_2/\gamma_1\, r_{02}$ or $r_{05} = \gamma_6/\gamma_5\, r_{06}$.

These electrons have to remain in symmetry in any frame of reference at all times. The electrostatic fields are schematically shown contracted in space, which is a result of the constant-velocity approximation. The correct retarded position for the point in space is schematically shown in Fig. 3.5(b). The initial spatial point symmetry is not broken and hence the symmetry particle does not experience any accelerating fields. In contrast, Fig. 3.5(c) shows the retarded positions applying the constant velocity approximation. p_1, p_2, p_3 and p_4 yield a longitudinally accelerating component acting on p_0, which is an artifact.

The reason for acceleration can be found when determining the retarded distance R at a time t_1 when particle j is acting on particle i. The retarded distance is characterized such that knowing R allows to use the *point-symmetric* Coulomb field *particularly for relativistic velocities*. The field can also be deduced from the Liénard-Wiechert potentials [31] and is given by

$$\vec{E}_{j\to i} = \frac{e}{4\pi\epsilon_0}\left[\frac{\vec{n}_{ji} - \vec{\beta}_j}{\gamma_j^2 R_{ji}^2\left(1 - \vec{n}_{ji}\vec{\beta}_j\right)^3}\right]_{\text{ret}} \tag{3.16}$$

with $\vec{n}_{ji} = \vec{R}_{ji}/R_{ji}$. The corresponding magnetic field is

$$\vec{B}_{j\to i} = \frac{1}{c}\left[\vec{n}_{ji} \times \vec{E}_j\right]_{\text{ret}}. \tag{3.17}$$

The origin of the interaction, hence, is located earlier in time at the time t_0. Within the retarded time $t_{ji} = t_1 - t_0$, particle j has traveled the distance $\vec{x}_{ji} = c\vec{\beta}_j t_{ji}$. Using linear extrapolation, the retarded distance can be calculated according to

$$\vec{R}_{ji} = \vec{r}_{ji} + \vec{x}_{ji} = \vec{r}_{ji} + c\vec{\beta}_j t_{ji} \tag{3.18}$$

$$= \vec{r}_{ji} + \vec{\beta}_j R_{ji}. \tag{3.19}$$

The absolute value is then determined to be

$$R_{ji} = \gamma_j^2\left(\vec{r}_{ji}\vec{\beta}_j + \sqrt{(\vec{r}_{ji}\vec{\beta}_j)^2 + \frac{|\vec{r}_{ji}|^2}{\gamma_j^2}}\right). \tag{3.20}$$

The particle interaction as deduced in this section does not involve any changing of the frame of reference. Furthermore, it can be shown that Eqs. (3.16) and (3.17) correspond to Eqs. (3.4) and (3.5).

The approximation as in Eq. (3.20) assumes uniform motion within the "dead time" interval

$$t_{ji} = \frac{R_{ji}}{c} \sim \gamma_j^2, \tag{3.21}$$

in which acceleration is not respected.

The retarded time transformed into the rest frame of the ultra relativistic bunch ($\gamma \gg 1$) scales according to

$$t'_{ji} \sim \gamma_j. \tag{3.22}$$

Hence, t_{ji} is minimized for the individual particle if γ_j is minimized. The "dead time" for a particle bunch propagating at the mean velocity $\langle\gamma\rangle$ can be reduced likewise by a factor of $\langle\gamma\rangle$ if the calculation is performed in the mean rest frame of reference. In this frame, retardation artifacts are minimized.

3.5 Appropriate Space Charge Calculation Method

Chapter I studies the dynamics of a high current electron beam as obtained from laser electron acceleration directly after the release into vacuum.

The first conclusion concerns the Lorentz transformation of the particle beam between the mean rest frame and the laboratory frame. Here, principal assumptions are required concerning the history of the bunch, which in our case involves the extraction of the bunch from a plasma accelerator. After the release, the electron bunch expands in vacuum due to Coulomb forces. These forces severely alter the energy distribution within the beam in a spatially highly correlated manner.

A further conclusion concerns widely applied calculation methods, which produce severe retardation artifacts being visible in the longitudinal phase space and which lead to the violation of energy conservation.

The problems with codes using these methods are severe enough to state that the design of applications being sensitive to space charge effects might be misguided. A prominent application of this kind is the FEL as described in chapter 6. Therefore, this topic is of importance and interest for both, the plasma-based advanced accelerator and the FEL modeling communities.

In this thesis, a calculation method for space charge effects has been developed, which is appropriate for calculating laser-accelerated electron beams. This development requires an enhanced understanding of the interactions revealing effects which can be neglected in conjunction with conventional acceleration but can clearly not be neglected using laser-accelerated beams.

All calculations contained in the publication that will be presented in chapter I were performed in the course of this thesis.

Chapter 4

Transport of Laser Accelerated Particle Beams

The next consequent step after considering the expansion of an electron beam in vacuum is its beam optical treatment. Similar to space charge effects, the application of optical devices for charged particle beams is as old as particles accelerators themselves.

Beam transport is a crucial component for all future real-world applications of laser-accelerated particles beams. The commonly used formalism to describe beam propagation is linear beam optics, where intra-beam interactions, i.e. space charge effects, are neglected. The introduction to linear beam optics provided here follows [35, 36].

Optical devices are considered for relativistic particles with $\beta \approx 1$. The Lorentz force

$$\vec{F} = -e(\vec{E} + \vec{v} \times \vec{B}) = -e(\vec{E} + c\vec{\beta} \times \vec{B}) = \dot{\vec{p}} \tag{4.1}$$

yields an effect of magnetic fields of the strength of 1 T = 1 Vsm^{-2}, corresponding to an electric field of the strength $3 \cdot 10^8$ V/m. For obtaining maximum focusing strength for relativistic beams, magnetic fields can be produced more easily than electrostatic fields. Magnetic fields are thus the method of choice for beam optical components used here.

4.1 Transport Matrices

A single particle propagating along the longitudinal direction z with given transverse positions, $x(z)$ horizontally and $y(z)$ vertically and the corresponding spatial derivative $x'(z) = \frac{p_x}{p_z}$ is written as

$$\boldsymbol{X}(z=0) = \begin{pmatrix} x(0) \\ x'(0) \\ y(0) \\ y'(0) \end{pmatrix} = \begin{pmatrix} x_0 \\ x'_0 \\ y_0 \\ y'_0 \end{pmatrix}. \tag{4.2}$$

The free longitudinal drift of a distance s of a particle for one plane is given by

$$\begin{aligned} x(s) =& x_0 + x_0' \cdot s \\ x'(s) =& x_0'. \end{aligned}$$

The distance s and the position z both refer to the longitudinal direction. We distinguish z to be the absolute position within the whole beam line system and s the position within one beam transport element.

The free drift is a beam transport element, the action of which can be written as a matrix transformation element. The state of a particle in Eq. (4.2) is hence altered using a 4×4 linear transformation matrix

$$\boldsymbol{X}(s) = \begin{pmatrix} x(s) \\ x'(s) \\ y(s) \\ y'(s) \end{pmatrix} = \begin{pmatrix} 1 & s & 0 & 0 \\ 0 & 1 & 0 & 0 \\ 0 & 0 & 1 & s \\ 0 & 0 & 0 & 1 \end{pmatrix} \begin{pmatrix} x_0 \\ x_0' \\ y_0 \\ y_0' \end{pmatrix} = \boldsymbol{M}_{\text{FreeDrift}} \begin{pmatrix} x_0 \\ x_0' \\ y_0 \\ y_0' \end{pmatrix}. \tag{4.3}$$

The linear transformation $\boldsymbol{M}$ for a single particle $\boldsymbol{X}_0$ is

$$\boldsymbol{X}_1 = \boldsymbol{M} \cdot \boldsymbol{X}_0. \tag{4.4}$$

In addition to the free drift, two further specific transportation matrices are of interest in this thesis.

Firstly, the magnetic dipole only acting on the x-component and neglecting focusing due to fringe fields in the y-component is given by the matrix

$$\boldsymbol{M}_{\text{Dipole}} = \begin{pmatrix} \cos\frac{s}{R} & R\sin\frac{s}{R} & 0 & 0 \\ -\frac{1}{R}\sin\frac{s}{R} & \cos\frac{s}{R} & 0 & 0 \\ 0 & 0 & 1 & s \\ 0 & 0 & 0 & 1 \end{pmatrix}, \tag{4.5}$$

where the bending radius is $R = p/(eB)$ with the particle's charge e, the particle's momentum p and the homogeneous magnetic field B.

Secondly, a magnetic quadrupole focuses the beam in one plane and defocuses it in the other. The matrix reflecting this behavior for focusing in the horizontal plane and defocusing the vertical plane is given by

$$\boldsymbol{M}_{\text{QF}} = \begin{pmatrix} \cos\Omega & \frac{1}{\sqrt{k}}\sin\Omega & 0 & 0 \\ -\sqrt{k}\sin\Omega & \cos\Omega & 0 & 0 \\ 0 & 0 & \cosh\Omega & \frac{1}{\sqrt{k}}\sinh\Omega \\ 0 & 0 & \sqrt{k}\sinh\Omega & \cosh\Omega \end{pmatrix} \tag{4.6}$$

for $\Omega = \sqrt{k}s$ with

$$k = \frac{e}{p}\frac{dB}{dx}. \tag{4.7}$$

Correspondingly, a quadrupole focusing in the vertical plane and defocusing the horizontal plane is given by

$$\boldsymbol{M}_{\mathrm{QD}} = \begin{pmatrix} \cosh\Omega & \frac{1}{\sqrt{k}}\sinh\Omega & 0 & 0 \\ \sqrt{k}\sinh\Omega & \cosh\Omega & 0 & 0 \\ 0 & 0 & \cos\Omega & \frac{1}{\sqrt{k}}\sin\Omega \\ 0 & 0 & -\sqrt{k}\sin\Omega & \cos\Omega \end{pmatrix}. \tag{4.8}$$

4.2 Determining the Magnetic Field Distribution

The matrix representation introduced above treats elements which have ideal pure dipole or quadrupole magnetic field components. Real beam optical devices in general include unwanted field errors, particularly multipole devices. Hence, the ability to analyze the magnetic field distribution of beam transport elements is a necessary prerequisite for the construction of high quality beam transport elements. The publication in chapter II presents a new method for determining the magnetic field distribution neglecting longitudinal field components ($B_z = 0$). Within the analyzed element, the field distribution is expanded in a simple way which quantitatively delivers dipoles, quadrupoles and higher order magnetic field components (HOMFC).

The magnetic vector fields of these elements satisfy the Maxwell equations $\vec{\nabla}\cdot\vec{B}(\rho,\varphi) = 0$ and $\vec{\nabla}\times\vec{B}(\rho,\varphi) = 0$, with ρ and φ being the transverse cylindrical coordinates.

The field expansion can be written as

$$\vec{B}(\rho,\varphi) = \sum_{l=1}^{\infty}[B_{l\rho}(\rho,\varphi)\vec{e}_\rho + B_{l\varphi}(\rho,\varphi)\vec{e}_\varphi] \tag{4.9}$$

with l being the order of the field component, namely dipole (l=1), quadrupole (l=2), sextupole (l=3), octupole (l=4), decapole (l=5) and dodecapole (l=6) for the lowest six orders.

The expansion terms $B_{l\rho}$ (radial) and $B_{l\varphi}$ (azimuthal) are given by

$$\begin{aligned} B_{l\rho}(\rho,\varphi) &= \rho^{l-1}[a_l\sin(l\varphi) + b_l\cos(l\varphi)] \\ B_{l\varphi}(\rho,\varphi) &= \rho^{l-1}[a_l\cos(l\varphi) - b_l\sin(l\varphi)]. \end{aligned} \tag{4.10}$$

The coefficients a_l and b_l of the order l can also be written in a more intuitive way, namely in magnitude $[\sqrt{a_l^2 + b_l^2}]$ and phase $[\arctan(b_l/a_l)]$.

Regarding a multipole device with a specific device axis at $\rho = 0$, the scaling of ρ in Eq. (4.10) shows that the field components close to the axis have less influence for higher orders l and on the other hand have an increased influence for larger radii ρ. This scaling explains why HOMFCs have less disturbing influence on the imaging quality of quadrupole devices if the aperture is only partially illuminated.

The conventional measurement method of the magnetic field distribution involves rotating coils. This approach is a reasonable characterization method if the size of the apertures is sufficiently large such that the coil fits in. A Fourier transform of the analog coil signal enables a direct access to the field components. For decreasing aperture sizes, however, the rotating coil method poses increasing challenges. These are not only limited to the requirements of the fabrication in accordingly small sizes, which is a source of measurement errors on its own. Also mechanical vibrations during the measurement process have to be suppressed, which involves large efforts [37].

In the publication presented in chapter II, a method was developed allowing to characterize the magnetic field distribution of miniature quadrupole lenses merely using a Hall probe. The Fourier expansion not only delivers the magnitude of HOMFCs, but also their phase. Measurement errors are accessible through the data itself and thus are intrinsically available. The method requires the knowledge of the center of rotation of the quadrupole, which can be obtained through very basic properties of the magnetic field distribution. The method is described in the appendix A.

4.3 Beam Propagation

The discussion hitherto describes the propagation of a single charged particle in a beam optical system. We now extend the discussion to a beam which is defined by a ensemble of particles moving in longitudinal direction.

Fig. 4.1a shows the beam propagation at several stages: Converging, collimated at the beam waist, diverging and during refocusing. A more detailed view on the state of a beam is given by the $x - x'$ diagrams in Fig. 4.1b-e, with the spatial transverse component x and the spatial transverse slope $x' = {}^{dp_x}/_{dp_z} \approx \beta_x$ for $\beta_z \approx 1$: The inclination of the beam ellipse as shown in Fig. 4.1b-e indicates the beam state. The $x - x'$ representation implies the ellipse rotating clockwise as a function of the propagation distance.

These ellipses are commonly called phase space ellipses in accelerator physics. A phase space is spanned by the canonical coordinates x and p_x and its phase space area is preserved according to Liouville's theorem. The plots as shown in Fig. 4.1b-e, which are commonly used in accelerator physics, do not refer to a phase space in general:

- Phase space: $x - p_x$
- Trace space: $x - x'$

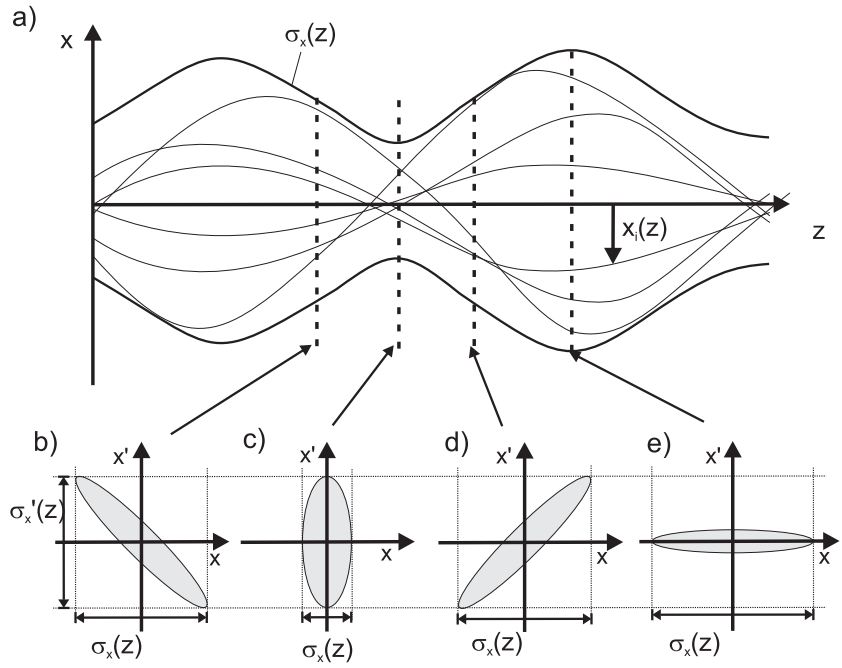

Figure 4.1: (a) The beam envelope function $\sigma_x(z)$ describes the spatial beam envelope of one transverse plane including all beam particles i at positions $x_i(z)$. The trace space diagrams at a longitudinal beam position z include the transverse positions x_i plotted versus the derivative $x_i' = {}^{dp_{ix}}/_{dp_{iz}}$. Trace space diagrams are shown for a converging beam (b), at its waist (c), diverging (d) and during refocusing (e).

The phase space area and the trace space area are proportional only if the beam is monoenergetic [38]:

$$\begin{aligned} x' &= \frac{dp_x}{dp_z}\ , \text{ not dependent of } \gamma, \text{ whereas} \\ p_x &= \beta_x \gamma m_0 c = p_x(\gamma) \text{ with} \\ \gamma &\sim E. \end{aligned} \tag{4.11}$$

A beam line commonly includes beam transport elements which are chromatic. A finite energy spread therefore enlarges the phase space area during the propagation including the free drift. The phase space volume grows steadily and is smoothly affected by chromatic beam elements such as focusing devices. The trace space area, in contrast, remains constant during the free drift, independently of energy spread and divergence. A chromatic element causes a jump of the trace space volume. If experiments have to be design according to specific emittance values, one has to be aware of the different behaviors of the phase space and the trace space. Laser particle acceleration in particular involves energy spreads to an extent, where these differences have to be considered.

For an analytical treatment, this section is based on the assumption of a monoenergetic beam and thus assumes a trace space volume which is proportional to the phase space volume.

According to Fig. 4.1, the beam can be defined using three quantities:

- The beam envelope size $\sigma(z)$

  with z being the longitudinal position of the beam during propagation. σ is the rms value of the transverse particles' positions, either horizontally or vertically.

- The divergence $\sigma'(z) = \frac{\mathrm{d}\,\sigma(z)}{\mathrm{d}\,z}$

- The trace space area A

  which is a conserved quantity for monoenergetic beams and translates into the beam emittance $\epsilon = A\pi$.

The use of beam optical elements allows to adjust the envelope size and divergence in accordance with experimental requirements. The conservation of the trace space volume or the emittance ϵ, respectively, allows for the introduction of a further set of parameters to identify the state of the beam. The emittance ϵ, the beam size $\sigma_x(z)$ and the divergence $\sigma_x'(z)$ are used to define the more general Courant-Snyder parameters [39]

$$\alpha(z) = -\frac{\beta'(z)}{2} = -\frac{\sigma'(z)}{\epsilon} \tag{4.12}$$

$$\beta(z) = \frac{\sigma(z)^2}{\epsilon}. \tag{4.13}$$

Apparently, three parameters are reduced to two. We will return to the question what exactly is generalized herein.

For convenience, we define $\gamma(z) = [1 + \alpha^2(z)]/\beta(z)$. The parameters β and γ have nothing to do with the relativistic normalized velocity or the Lorentz factor.

In a next step, we define the $\boldsymbol{\beta}$ matrix which describes a beam state in a general representation as

$$\boldsymbol{\beta}(z) = \begin{pmatrix} \beta(z) & -\alpha(z) \\ -\alpha(z) & \gamma(z) \end{pmatrix}. \tag{4.14}$$

Similar to Eq. (4.4), the beam propagation is calculated following

$$\boldsymbol{\beta}_1 = \boldsymbol{M} \cdot \boldsymbol{\beta}_0 \cdot \boldsymbol{M}^T. \tag{4.15}$$

A simple and important example of a beam transport calculation is the free drift. The longitudinal position $s = 0$ is chosen to be the waist position, i.e. the symmetry point within the free propagation. Since we consider only the free drift as a single transportation element, we use s instead of z. At this point, we choose an initial $\beta(0) = \beta^*$ and $\alpha_0 = 0$.

This initial beam configuration corresponds to a phase space ellipse as shown in Fig. 4.1c. Using Eqs. (4.3), (4.14) and (4.15), we obtain

$$\begin{aligned}\boldsymbol{\beta} &= \begin{pmatrix} 1 & s \\ 0 & 1 \end{pmatrix} \cdot \begin{pmatrix} \beta^* & 0 \\ 0 & \frac{1}{\beta^*} \end{pmatrix} \cdot \begin{pmatrix} 1 & 0 \\ s & 1 \end{pmatrix} \\ &= \begin{pmatrix} \beta^* + \frac{s^2}{\beta^*} & \frac{z}{\beta^*} \\ \frac{z}{\beta^*} & \frac{1}{\beta^*} \end{pmatrix} \end{aligned} \tag{4.16}$$

and hence

$$\begin{aligned}\beta(s) =& \beta^* + \frac{s^2}{\beta^*} \\ \alpha(s) =& -\frac{s}{\beta^*}. \end{aligned} \tag{4.17}$$

With Eqs. (4.12) and (4.13), the beam size is

$$\sigma^2(s) = \epsilon\beta(s) = \frac{\epsilon}{\beta^*}\left(\beta^{*2} + s^2\right) = \frac{\epsilon}{\beta^*}\left[1 + \left(\frac{\beta^*}{s}\right)^2\right] s^2. \tag{4.18}$$

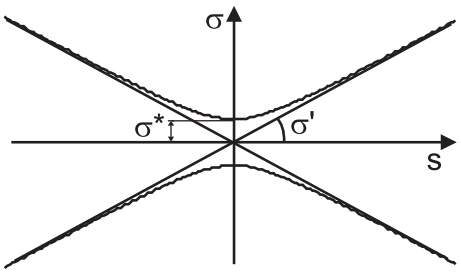

Figure 4.2: Free drift of a converging electron beam of the slope $\sigma' = \frac{d\sigma(s)}{ds}$ going through a waist at the longitudinal position $s = 0$ at a waist size σ^*.

Using $\sigma^* = \sqrt{\epsilon\beta^*}$, we obtain

$$\sigma(s) = \sqrt{\sigma^{*2} + \frac{\epsilon^2 s^2}{\sigma^{*2}}}, \tag{4.19}$$

as shown in Fig. 4.2. Moreover, due to

$$\frac{d\sigma(s)}{ds} = \sigma'(s) = \frac{\epsilon^2}{\sigma^{*2}}\left[\frac{\sigma^{*2}}{s^2} + \frac{\epsilon^2}{\sigma^{*2}}\right]^{-\frac{1}{2}} \tag{4.20}$$

for $s \to \infty$ we obtain the simple and important result

$$\sigma^* \cdot \sigma' = \epsilon. \tag{4.21}$$

Hence, the size of the beam waist σ^* solely depends on the divergence σ' for $s \to \infty$ and the emittance ϵ.

Conventional accelerators with typical acceleration lengths of tens of meters up to kilometers have a critical section at the very beginning of the acceleration line. It is this beginning which determines the emittance within the first few centimeters. The major reason herefore is the space charge which has a dominant impact on the momentum distribution of the particle beam where the velocities are not yet relativistic. Afterwards, the transverse motion components can be assumed to remain constant during acceleration.

The effect of acceleration onto the beam emittance can be eliminated introducing the normalized emittance

$$\epsilon_n = \epsilon \cdot \gamma \tag{4.22}$$

with a Lorentz factor $\gamma \sim p_z (\gamma \gg 1)$.

The linear beam optics formalism provides a basis for designing and calculating the beam propagation for virtually any application of particle beams.

4.4 Tuning Permanent Magnet Quadrupoles

Many important applications for electron beams require beam optical treatments as introduced in the section before. In the course of this thesis it was found that conventional beam optical devices cannot be applied for laser accelerated particle beams for a major reason. Long drift distances between the laser accelerator and the experiment harm the quality of the electron beam due to space charge effects. It is hence mandatory to minimize the distance between extraction of the beam from the accelerator and the experiment.

The answer to these issues is making use of miniature beam optical devices such as the permanent magnet multipole devices proposed in 1980 by Halbach [40]. These devices produce ultra-high magnetic quadrupole field gradients in the order of 500 T/m, which exceeds even superconductive quadrupole devices by at least a factor of 2.

The drawback in using miniature devices has already been introduced in section 4.2. Due to the large ratio of beam size to aperture size, they commonly yield unwanted or even severely distorting HOMFCs. The resulting imaging aberrations lead to an increasing beam emittance. Applications which are sensitive to the beam emittance require the minimization of HOMFCs to values virtually zero. An example is the FEL.

In the course of this thesis, miniature Halbach-like quadrupole devices have been built. Not only was a measurement method developed, which allows their characterization by precisely determining HOMFCs quantitatively as described in section 4.2. But also does the publication contained in chapter II describe how this characterization is used as a basis for tuning the Halbach kind multipole device in order to achieve full control over HOMFCs. The characterization result is used for compensating undesired HOMFCs, which mainly originate from unavoidable fabrication tolerances. An important aspect is the fact that the

knowledge of the precise origin of HOMFCs is irrelevant for the compensation. The only information required is the magnitude and particularly the phase of a field component. The compensation is achieved by introducing a field component of the same magnitude but with a phase shift of 180°.

This approach is general enough to not only correct for the field errors, but also enable the shaping of the magnetic field distributions by introducing specific HOMFCs. In the case of multipole devices, HOMFCs can be used to compensate principal effects such as spherical aberrations due to fringe fields.

These methods were developed in the course this thesis and concern miniature multipole devices which are mandatory for experiments such as the laser-driven FEL. The field of application for these tuned quadrupole devices might also be extended to conventional particle acceleration.

4.5 First Focusing of Laser Accelerated Ions

The miniature Halbach-like beam optical devices are mandatory for many applications of laser-particle acceleration. The first experimental proof of principle for focusing of a laser based accelerated ion beam has been obtained in the course of this thesis and is published as shown in chapter III. The acceleration method used in this publication is Target Normal Sheath Acceleration (TNSA) as introduced in section 2.4.1. The experiment was carried out at the Z-Petawatt laser facility at Sandia National Laboratories. The quadrupole devices applied are of the Halbach type as introduced in the previous section. The task of

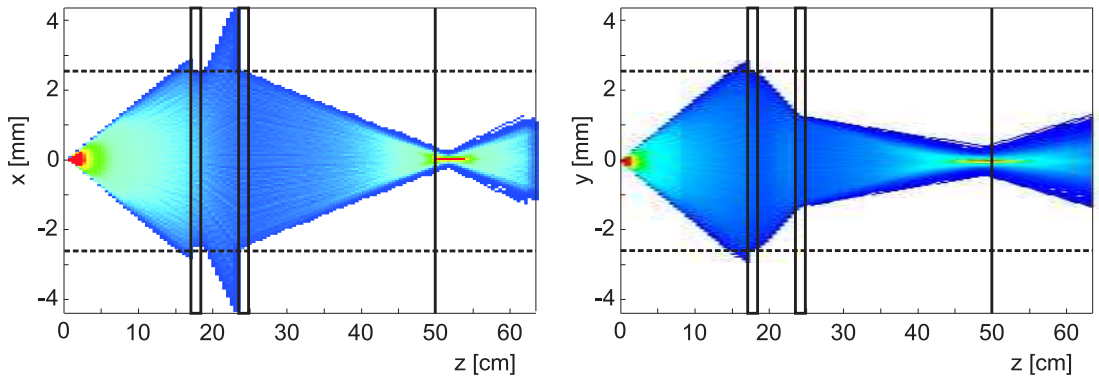

Figure 4.3: Spatial ion beam propagation as obtained from numerical calculations in 3D are shown in the horizontal beam plane x and the vertical plane y plotted versus the propagation direction z. The rainbow kind color coding shows the flux density of the proton beam. The pairs of vertical lines show the positions of the quadrupole devices and the single vertical line indicates the position of the stack of radiochromic films. The dashed horizontal lines show the aperture size of the quadrupole devices.

focusing an ion beam might at first glance appear to be trivial, as it has been performed for many decades. There are major aspects, however, which are different in the regime of laser-accelerated particle beams. The laser system used for the experiment mentioned above has a repetition rate of 45 minutes. The number of parameters of the beam optical system is too large to be adjusted during the experiment. They mainly involve the length and position of the quadrupole devices as well as the position of the stack of radiochromic films[1] as shown in Fig. 4.3. Hence, the precision of the calculations of these parameters performed prior to the experiment decides on the success of the experiment. The calculations for this experiment were done using a 3D tracking algorithm and applying Maxwell-compliant 3D magnetic field maps in accordance with the specific design of the quadrupoles.

In the course of this thesis concerning chapter III, the assembly and characterization of the quadrupole devices has been carried out as well as the calculations leading to the positioning of quadrupoles and diagnostic elements as shown in Fig. 1 and all simulations displayed in Fig. 3.

[1]The stack of radiochromic films allows the detection of both, the spatial distribution and the energy distribution of the ion beam.

Chapter 5

Undulators and Undulator Radiation

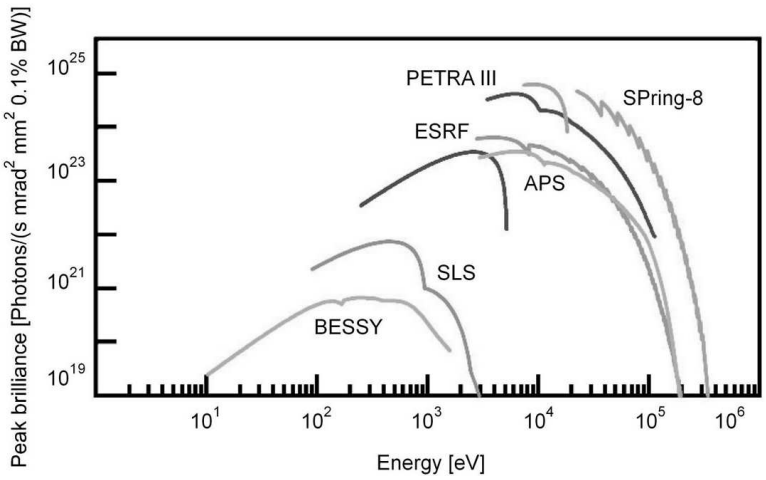

Figure 5.1: Shows the peak brilliance among a number of prominent 3$^{\text{rd}}$ generation synchrotron radiation sources. [41].

The production of photon beams using synchrotron radiation took a remarkable development in the past 40 years. The quality of a photon beam can be described defining the peak brilliance which is the number of photons per second, per mm^2, per mrad^2 and per 0.1% bandwidth. New methods have been developed, producing photon beams which stepwise lead to an increase of the brilliance by orders of magnitude as shown in Fig. 5.1. In the 1970s, the first step marks the introduction of first generation synchrotron radiation (SR) sources [42, 43], where the accelerated electron or positron beams have been primarily used for high-energy experiments. These first SR experiments took the "left overs" of the main experiments and have thus been carried out in a parasitic mode. In the early 1980s, dedicated machines have been built for the first time producing SR in the second generation, where electron beams are deflected in a bending magnet. In the late 1980s, SR sources of the third generation have been designed and built. The key device here is the

undulator, which consists of a periodic arrangement of dipole magnets. An electron propagating through the dipole magnet fields is accelerated in transverse direction, which results in the emission of undulator radiation, which is a special kind of synchrotron radiation. The periodic acceleration leads to a sinusoidal trajectory, which causes interference effects enhancing the brilliance by orders of magnitude compared to bending magnet radiation.

A number of results are presented in this thesis, which concern the testing and the development of undulator devices. The following introduction to the basics of undulators and undulator radiation follows the description given in Refs. [35, 44].

5.1 Electron Trajectories

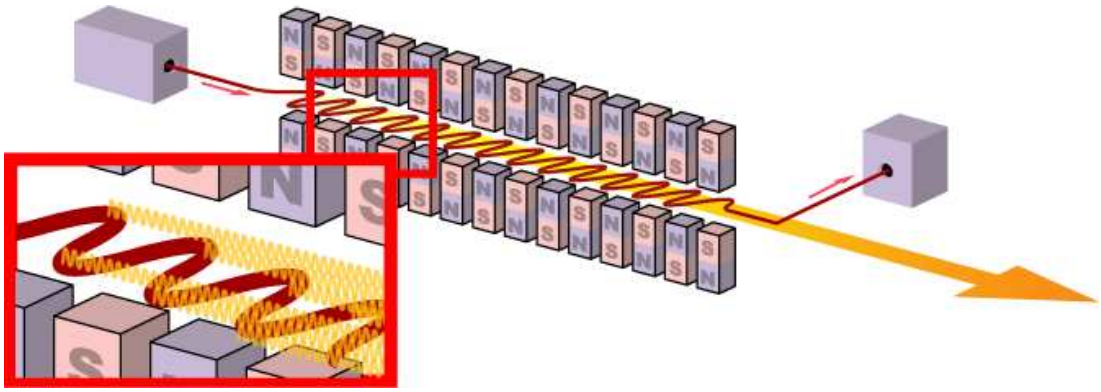

Figure 5.2: An undulator is a periodic arrangement of dipole magnets forcing an electron beam on a sinusoidal trajectory as shown schematically. Due to the periodical transverse acceleration, the electron beam emits undulator radiation in the propagation direction of the electron beam. [45].

An undulator setup is schematically shown in Fig. 5.2. The consideration of an ideal planar undulator is assumed to have no field dependence along the transverse undulator plane and hence $B_x = 0$.

The analytical Maxwell-compliant magnet undulator field is given by

$$B_y(z, y) = \frac{B_0}{\cosh\left(\pi \frac{g}{\lambda_u}\right)} \cosh(k_u y) \cos(k_u z) \tag{5.1}$$

in the transverse component y and

$$B_z(z, y) = \frac{B_0}{\cosh\left(\pi \frac{g}{\lambda_u}\right)} \sinh(k_u y) \sin(k_u z), \tag{5.2}$$

in the longitudinal component z. Here, B_0 is the peak magnetic field on axis, λ_u is the undulator period length, g is the undulator gap and $k_u = 2\pi/\lambda_u$ is the undulator wave number.

The ratio of the on-axis peak field B_0 at $y = 0$ and the peak field on the surface of the undulator $\hat{B}$ at $y = \pm g/2$ is

$$\frac{B_0}{\hat{B}} = \cosh\left(\pi \frac{g}{\lambda_u}\right) \tag{5.3}$$

leading to the equation of motion

$$\frac{d^2x}{dt^2} = \ddot{x} = -\frac{\beta c e \hat{B}}{m_e \gamma} \cos(k_u z). \tag{5.4}$$

The trajectory is obtained by replacing the derivative in time with the derivative in space $\dot{x} = x'\beta c$ and $\ddot{x} = x''\beta^2 c^2$, which yields

$$\frac{d^2x}{dz^2} = x'' = -\frac{e\hat{B}}{m_e \beta c \gamma} \cos(k_u z), \tag{5.5}$$

$$x' = \frac{\lambda_u e \hat{B}}{2\pi m_e \gamma c} \sin(k_u z), \tag{5.6}$$

$$x = \frac{\lambda_u^2 e \hat{B}}{4\pi^2 m_e \gamma c} \cos(k_u z). \tag{5.7}$$

The deflection angle is $\Theta = \arctan x' \approx x'$. With Eq. (5.6), this results in the maximum deflection angle

$$\Theta_w = \frac{1}{\gamma} \frac{\lambda_u e \hat{B}}{2\pi m_e c}. \tag{5.8}$$

This expression suggests the definition of the undulator parameter

$$K = \frac{\lambda_u e \hat{B}}{2\pi m_e c} \tag{5.9}$$

with the deflection angle $\Theta_w = K/\gamma$.

The particle propagates with constant velocity βc and the magnetic field periodically alters the propagation direction. The average horizontal velocity $\dot{s}$ can finally be estimated with the transverse velocity $\dot{x}$ using $\dot{s}^2 = (\beta^2 c)^2 - \dot{x}^2$ and $\beta^2 = 1 - 1/\gamma^2$. We obtain

$$\dot{s}^*(t) = c\sqrt{1 - \left(\frac{1}{\gamma^2} + \frac{\dot{x}^2}{c^2}\right)}. \tag{5.10}$$

A first-order Taylor approximation yields

$$\dot{s}^*(t) = c\left[1 - \frac{1}{2\gamma^2}\left(1 + \frac{\gamma^2}{c^2}\dot{x}^2\right)\right]. \tag{5.11}$$

Following from Eqs. (5.4) and (5.9)

$$\dot{x} = \beta c \frac{K}{\gamma} \sin(\omega_u t), \tag{5.12}$$

we obtain

$$\dot{s}(t) = c \left\{ 1 - \frac{1}{2\gamma^2} \left[1 + \frac{\beta^2 K^2}{2} \left(1 - \cos(2\omega_u t) \right) \right] \right\}. \tag{5.13}$$

Averaging yields the average longitudinal velocity

$$\dot{\bar{s}}(t) = c \left\{ 1 - \frac{1}{2\gamma^2} \left[1 + \frac{\beta^2 K^2}{2} \right] \right\}, \tag{5.14}$$

which is required for calculating the characteristics of the undulator spectrum in the next section.

5.2 Spontaneous Undulator Radiation

The spectrum of spontaneous undulator radiation, i.e. third generation SR, consists of a fundamental peak and higher harmonics. This peaked spectral distribution is the result of a single electron interfering with its own emitted radiation, while propagating through the undulator. The wavelength of the fundamental peak can be calculated by deducing a resonance condition.

First we consider the oscillation frequency in the laboratory frame which is

$$\Omega = \frac{2\pi}{T} = \frac{2\pi\beta c}{\lambda_u} = k_u \beta c. \tag{5.15}$$

The transformation into the rest frame of the velocity β^* and the corresponding Lorentz factor γ^* for the frequency yields

$$\omega^* = \gamma^* \Omega. \tag{5.16}$$

The transformation back into the laboratory, which requires the relativistic Doppler shift for frequencies, is then given by

$$\omega = \frac{\omega^*}{\gamma^*(1 - \beta^* \cos\Theta)} = \frac{\Omega}{1 - \beta^* \cos\Theta} \tag{5.17}$$

with Θ being the angle of observation with respect to the propagation direction. The observed wavelength is written as

$$\lambda = \lambda_u (1 - \beta^* \cos\Theta). \tag{5.18}$$

This result together with Eq. (5.14) yields the undulator radiation wavelength for the fundamental peak

$$\lambda = \frac{\lambda_u}{2\gamma^2}\left(1 + \frac{K^2}{2} + \gamma^2\Theta^2\right). \tag{5.19}$$

Purely harmonic wiggling of an electron bunch in an infinitely long undulator yields monochromatic undulator radiation. However, in a realistic scenario the undulator will be limited in length and thus the undulator radiation wave train with an undulator frequency ω_u will be limited in time as

$$u(\omega_u, t) = \begin{cases} a\exp(i\omega_u t) & : -\frac{T}{2} \leq t \leq \frac{T}{2} \\ 0 & : \text{else.} \end{cases} \tag{5.20}$$

The Fourier transform from time into the frequency domain is given by

$$A(\omega) = \frac{1}{\sqrt{2\pi}T}\int_{-\infty}^{\infty} u(\omega_u, t)\exp(-i\omega t)dt, \tag{5.21}$$

and thus

$$A(\omega) = \frac{a}{\sqrt{2\pi}T}\int_{-T/2}^{T/2} \exp(-i(\omega-\omega_u)t)dt \tag{5.22}$$

$$= \frac{2a}{\sqrt{2\pi}T}\frac{\sin(\omega-\omega_u)\frac{T}{2}}{\omega-\omega_u} \tag{5.23}$$

$$= \frac{a}{\sqrt{2\pi}}\frac{\sin\left(\pi N_u \frac{\Delta\omega}{\omega_u}\right)}{\pi N_u \frac{\Delta\omega}{\omega_u}} \tag{5.24}$$

with $\Delta\omega = \omega - \omega_u$ and $\omega_u T = 2\pi N_u$. Finally, the intensity scales as

$$I(\Delta\omega) \propto \left[\frac{\sin\left(\pi N_u \frac{\Delta\omega}{\omega_u}\right)}{\pi N_u \frac{\Delta\omega}{\omega_u}}\right]^2 = \left[\frac{\sin x}{x}\right]^2 = \text{sinc(x)} \tag{5.25}$$

where $x = \pi N_u\, \Delta\omega/\omega_u$. Applying $\text{sinc(x)} = 1/2$ for $x = 1.392$ yields

$$\frac{2\Delta\omega}{\omega_u} = \frac{2x}{\pi N_u} = \frac{0.886}{N_u} \sim \frac{1}{N_u}. \tag{5.26}$$

This important result shows the scaling of the line width of an undulator radiation peak as a function of the number of undulator periods.

A last conclusion on the spontaneous undulator radiation can be drawn from the fact that the radiation intensity scales linearly with the undulator length and so does the number of periods: With Eq. (5.26), the peak spectral intensity scales as

$$\hat{I} \sim N_u^2, \tag{5.27}$$

which favors the undulator over a bending magnet for experiments requiring high spectral peak intensity.

5.3 New Test Undulator Device

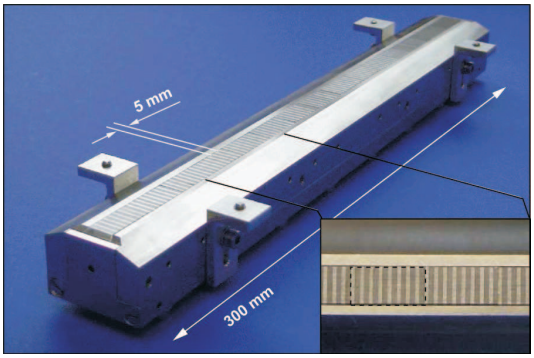

Figure 5.3: Photograph of the lower half of the 60 period planar undulator after the first preliminary assembly. In the insert, the precision glued magnet stacks are visible (dashed box).

An undulator was built, characterized and tested at the Mainz Microtron MAMI. For maximizing the photon energy, the undulator period length was minimized according to Eq. (5.19). The period length of 5 mm is currently (to our knowledge) the shortest in the world. Important knowledge and experience was gathered while building and testing this undulator device. The tests at MAMI are published as shown in chapter IV involve the generation of spontaneous undulator radiation and the first test of the (non-tuned) permanent magnet quadrupoles, which have been introduced in the publication as shown in chapter 4.4.

In the course of this thesis concerning chapter IV, the assembly and characterization of the quadrupole devices leading to Fig. 10 was performed as well as the experimental analysis leading to Fig. 11. Important contributions leading to the experimental results as published and presented in chapter IV have been made.

5.3.1 Further Investigations on the Undulator Spectrum

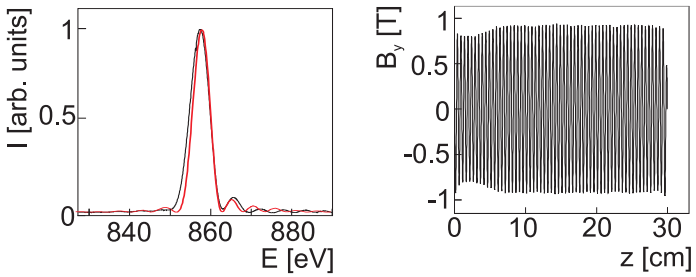

Figure 5.4: The black curve on the left hand side shows the measured on-axis high-resolution energy spectrum of the third harmonic undulator radiation for an electron beam energy of 405 MeV as used during the experiment at the MAMI accelerator facility. The red curve on the left hand side is the calculation of the spectrum using a magnetic field measurement shown on the right hand side. The magnetic field was obtained using a Hall probe measurement.

The measurements of the undulator radiation spectrum as published in chapter IV, Fig. 7 were performed at high energy resolution.

The spectrum is also shown as the back curve on the left hand side of Fig. 5.4. The question remains, however, where the asymmetry for the red curve, which is the third harmonic, originates from. The deduction of basic characteristics of undulator radiation of Eq. (5.25) yields a symmetric spectrum.

The magnetic field distribution of the test undulator yields a dip at one end of the device as shown on the right hand side of Fig. 5.4. This dip was not taken into account for the discussion of the spectrum. The calculation of the undulator radiation using the measured magnetic field distribution was performed using WAVE [46], where the asymmetry as obtained by the measurement at MAMI could be reproduced as shown on the left hand side of Fig. 5.4.

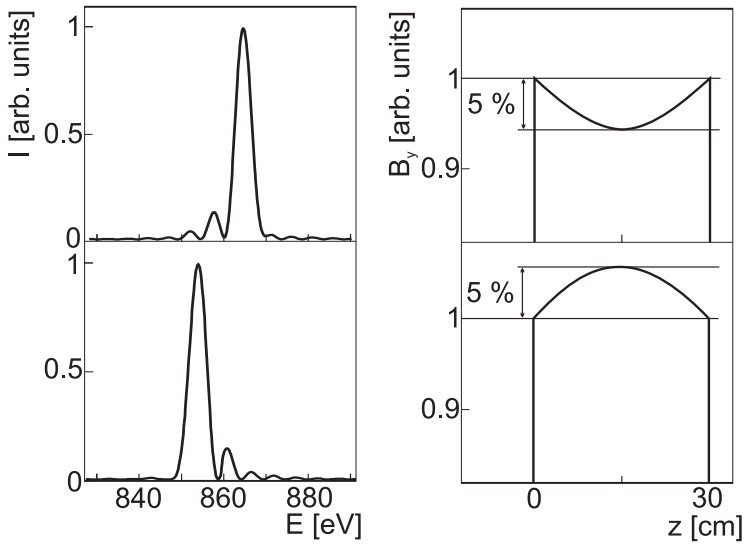

Figure 5.5: The figures on the left hand side show numerical calculations of an ideal undulator field, which is modulated according to the drawing on the right hand side. Asymmetries occur in dependence of the kind of modulation: On the upper right hand side, the course of the magnetic field distribution shows a dip while the curse on the lower right hand sides shows an elevation of the distribution field. The lower figures well reflect the kind of distortion as it was obtained from the field measurements of the undulator device as used in the experiment.

The question arises, whether a spectral distribution as shown in Fig. 5.4 allows to draw more general conclusions on the undulator device. The right hand side of Fig. 5.5 shows a modulation of the magnetic field as a function of the longitudinal undulator position and the asymmetry introduced within the undulator spectrum. Since the results of the corresponding calculations of the spectrum on the left hand side of Fig. 5.5 correspond to the observations, some asymmetries could be used more general to obtain indications on the origin of the asymmetry in the undulator spectrum.

5.4 Laser-driven soft-X-ray undulator source

Our group recently succeeded in measuring laser-driven spontaneous undulator radiation in the soft-X-ray regime for the first time [47]. This experiment poses two major challenges. Firstly, laser-plasma acceleration is still a single shot experiment since fluctuations of important beam parameters from shot to shot are too large for producing a radiation spectrum by accumulating several shots. Secondly, the large energy spread compared to conventional accelerators smears out the characteristics of undulator radiation if the experiment is carried out conventionally. The experiences presented in the previous section gathered with the test undulator and the Halbach-like quadrupoles at MAMI have been the basis for successfully obtaining spontaneous undulator radiation using laser accelerated electrons. The undulator used for this experiment is the test undulator presented in this thesis.

Concerning the comparatively large energy spread of beams obtained from bubble acceleration, the key elements for these experiments are the quadrupole focusing devices. Their chromatic properties allow the selection of electrons at a more narrow energy distribution. The narrowed distribution allows to obtain the characteristic undulator radiation spectrum. The electrons at the desired energy are focused on the transmission grating as shown in Figs. 5.6 and 5.7. Not using quadrupoles would result in a radiation spectrum, where all characteristics of undulator radiation are smeared out. The quadrupole devices applied do not require high quality quadrupole fields, since spontaneous undulator radiation is insensitive to emittance.

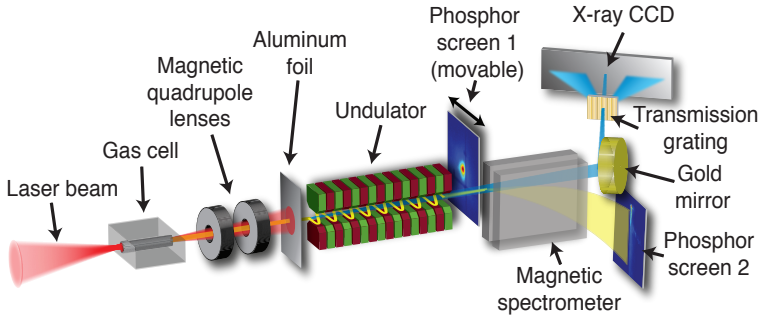

Figure 5.6: The experimental set-up is shown schematically. A laser pulse (red) is focused into a gas cell. The electron beam is collimated by a pair of quadrupole lenses. The electrons propagate through an undulator and emit soft-X-ray radiation into a narrow cone along the forward direction (blue). The radiation is characterized by a transmission grating in combination with an X-ray CCD camera. [47].

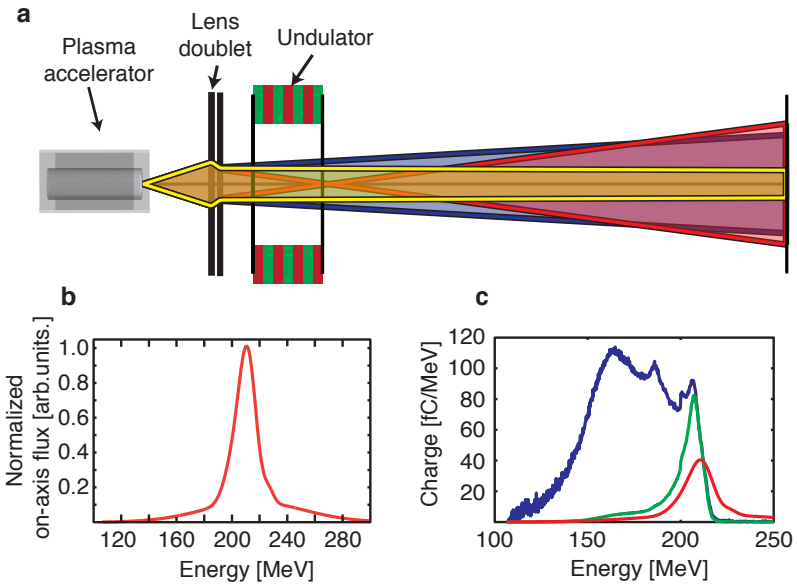

Figure 5.7: The effect of the magnetic lenses is shown schematically. a, Divergence of electrons traversing the magnetic lens assembly with energies of 190 MeV (red), 215 MeV (yellow) and 240 MeV (blue). b, Simulated normalized on-axis flux of the fundamental undulator emission versus electron energy. The narrow bandwidth of 9% FWHM is due to the energy-dependent electron-beam divergence introduced by the magnetic lenses. c, Measured electron spectrum (blue). The effective electron spectrum (green) is determined by the product of the measured spectrum (blue) and the system response curve (red in b,c). [47].

Chapter 6

Free Electron Laser

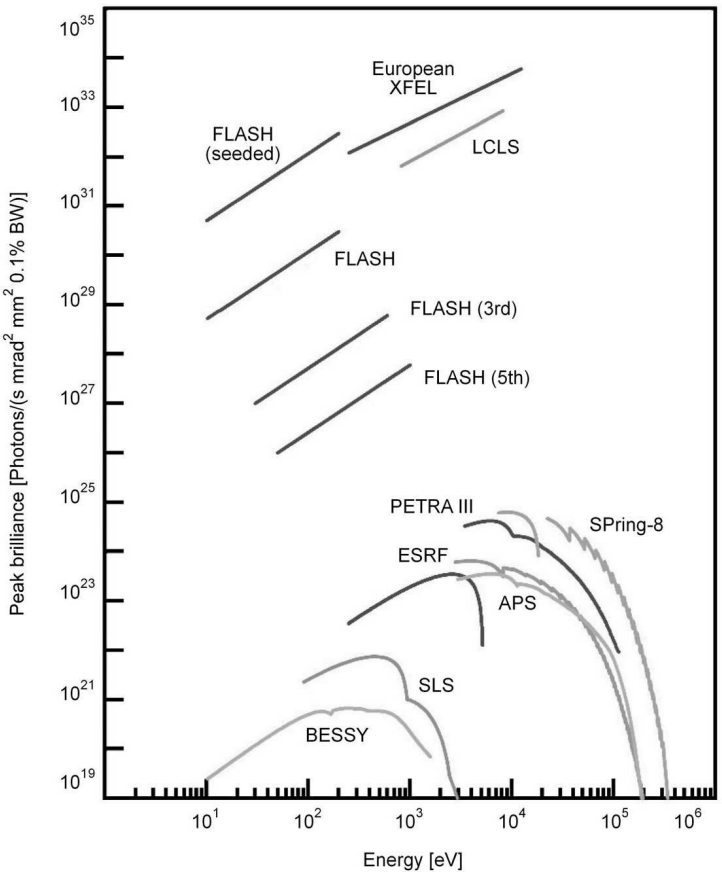

Figure 6.1: In addition to the 3rd generation synchrotron radiation sources, the photon peak brilliance of 4th generation sources are shown. FLASH and LCLS [48] are in operation, the European XFEL [15] is currently under construction. [41].

Conventional laser systems emit photon beams based on discrete quantum mechanical transitions in atoms, molecules or solids. These transitions cover a maximum energy gap expressed as lasing wave lengths down to 100 nm. Beyond these wave lengths down to the Å-regime, conventional lasers do not exist. The Free-Electron-Laser (FEL) is the most prominent method to overcome this limitation. The FEL is also referred to as fourth generation synchrotron radiation (SR) source producing the most brilliant X-ray photon source currently available as shown in Fig. 6.1. An FEL is based on an electron beam propagating through an undulator device. The modulation of the electron density distribution within the beam leads to coherent emission of undulator radiation. In comparison to third generation SR sources, the photon beam peak brilliance is further increased by typically ten orders of magnitude.

A prominent goal for laser-accelerated electron beams is driving an FEL.

6.1 Energy Transfer

The working principle of an FEL is the energy transfer from electrons on the trajectory s into a coherent light field $\vec{E}_L$, which is generally given by [35]

$$\Delta W = -e \int \vec{E}_L \cdot d\vec{s} = -e \int \vec{E}_L \vec{v} dt. \tag{6.1}$$

On the one hand, the condition for an efficient transfer of kinetic electron energy into electromagnetic field energy is the co-propagation of electron and field. On the other hand, this general case yields $\vec{v} \perp \vec{E}_L$ and thus $\Delta W = 0$. If the electron moves through an undulator, however, a transverse velocity component of $\vec{v}$ is introduced and therefore $\Delta W \neq 0$.

Introducing into Eq. (6.1) the transverse electron motion

$$v_y = c\frac{K}{\gamma} \sin(k_u z) \tag{6.2}$$

and the light field

$$E_{L,y} = E_{L,0} \cos(k_L z - \omega_L t + \varphi_0), \tag{6.3}$$

we obtain a phase between the periodic electron motion and the light field

$$\Psi_\pm = (k_L \pm k_u) z - \omega_L t + \varphi_0. \tag{6.4}$$

The transfer of energy is only possible, if the phase does not vary:

$$\frac{d\Psi_\pm}{dt} = (k_L \pm k_u)\dot{z} - \omega_L \approx 0. \tag{6.5}$$

Here, $\dot{z}$ corresponds to the average velocity $\bar{\dot{z}}$ from Eq. (5.14). With $k_u \ll k_L$, we obtain

$$k_u = \frac{k_L}{2\gamma^2}\left(1 + \frac{K^2}{2}\right). \tag{6.6}$$

Replacing k_L and k_u results in the condition for energy transfer

$$\lambda = \frac{\lambda_u}{2\gamma^2}\left(1 + \frac{K^2}{2}\right), \tag{6.7}$$

which equals the resonance condition for spontaneous undulator radiation as in Eq. (5.19).

Hence, at first glance, an experimental setup of an FEL is equivalent to a third generation SR. An electron beam is coupled into an undulator device. The difference is that the electrons have to contribute to the energy of the light field *in phase*. The light field is hence coherent. This is only possible if the electron beam generates sub-bunches at distances of the wavelength of the light field called *microbunching* as shown in Fig. 6.2.

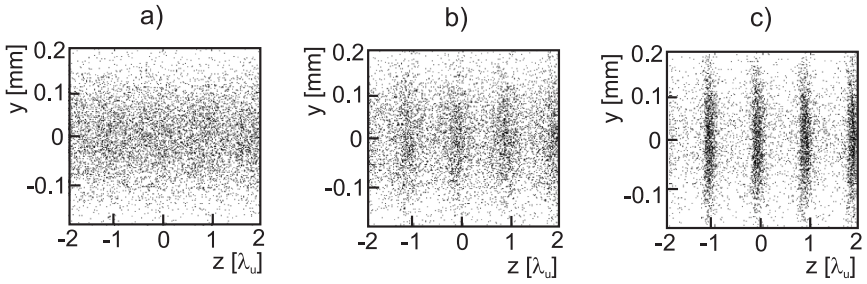

Figure 6.2: (a) Schematically an initially uncorrelated electron distribution is shown. Inside an undulator, this distribution emits spontaneous incoherent undulator radiation. Under specific conditions, the bunch develops correlations as shown in (b) and (c) called microbunching. (Plots are generated using Genesis 1.3 [49].)

The coherent properties of the light field due to microbunching affect the intensity of the emitted radiation. Spontaneous undulator radiation as introduced the previous chapter can be deduced considering only a single electron, which is equivalent to an electron bunch with a homogeneous density distribution, shown in Fig. 6.2a. The bunch emits incoherent spontaneous undulator radiation. The scaling of the electric field amplitude and the radiation intensity correspond to a random walk with respect to the number of electrons N_e radiating with

$$E \sim \sqrt{N_e} \tag{6.8}$$

$$I \sim N_e, \tag{6.9}$$

where I is the intensity.

In the case of an FEL, the electron bunch has developed microbunches, which are separated from each other by the distance of the emitted wavelength λ_u as shown in Fig. 6.2c. The emission is coherent and the field amplitude scales as

$$\begin{aligned} E &\sim N_e \\ I &\sim N_e^2. \end{aligned} \tag{6.10}$$

A typical number of electrons participating in the lasing process is in the order of $N_e = 10^{10}$. Consequently, the intensity of the coherent emission is a factor of 10^{10} above the one for spontaneous undulator radiation.

6.2 Self-Amplification of Spontaneous Emission

Microbunching can be generated in different ways. An experimentally rather simple approach is *seeding*, where a coherent photon beam co-propagates with the electron bunch and interacts with the bunch, such that energy modulations lead to microbunching. A major disadvantage of seeding is the non-availability of a coherent light source in the desired lasing wavelength in the X-ray regime. Hence, seeding is not further discussed here.

The approach mainly referred to in this thesis is Self-Amplification of Spontaneous Emission (SASE), which was first predicted in 1984 by R. Bonifacio [50]. Under certain conditions, small density fluctuations inside the homogeneous density distribution, called shot noise, result in an unstable behavior leading to larger density modulations and eventually microbunching. This process is shown in the sequence of Fig. 6.2.

The power of the radiation field evolves exponentially as a function of microbunching. The length in which the power has increased by a factor of Euler's number e is called the gain length

$$L_{\text{gain,ideal}} = \frac{\lambda_u}{4\pi\sqrt{3}\rho} \tag{6.11}$$

with the undulator period length λ_u and the Pierce parameter ρ. The Pierce parameter, also called *FEL parameter*, describes the conversion efficiency of the electron beam energy into the FEL beam energy and is given by

$$\rho = \frac{1}{2\gamma}\left[\frac{I}{I_A}\left(\frac{\lambda_u A_u}{2\pi\sigma_x}\right)^2\right]^{1/3}, \tag{6.12}$$

where γ is the Lorentz factor of the electron beam, I is the beam current, $I_A = 17kA$ is the Alfvén current, σ_x the beam size and $A_u = a_u[J_0(\zeta) - J_1(\zeta)]$ (planar undulator) with $J_\alpha(\zeta)$ being the Bessel functions and $a_u^2 = K^2/2$ with K being the undulator parameter as defined in Eq. (5.9).

This consideration, however, only addresses the ideal case, i.e. neglecting energy spread, emittance, diffraction and time dependence.

A realistic gain length can be approximated [51] using

$$L_{\text{gain}} = L_{\text{gain,ideal}}(1 + \Lambda). \tag{6.13}$$

The correction factor Λ accounts for energy spread, emittance and diffraction.

The propagation length at which the SASE-FEL process reaches saturation is called the saturation length

$$L_{\text{sat}} = L_{\text{gain}} \ln\left(\frac{P_{\text{sat}}}{\alpha P_n}\right). \tag{6.14}$$

P_n is the shot noise power originating from the spontaneous undulator radiation and α=1/9 is the coupling factor describing the efficiency at which the noise power couples to the FEL gain process. The saturation length determines the required undulator length. A large pierce parameter reduces the saturation length and thus reduces the required undulator size. Laser acceleration promises beam currents which are significantly higher than what can be obtained from conventional acceleration and consequently yields a larger Pierce parameter.

P_{sat} is the saturation power which scales as

$$P_{\text{sat}} \sim \left(\frac{1}{1+\Lambda}\right)^2 (I\lambda_u)^{4/3}. \tag{6.15}$$

The FEL wavelength corresponds to the resonance condition of the spontaneous undulator radiation in Eq. (5.19).

An important condition for an upper limit of the energy spread of the electron bunch required for the operation of a SASE-FEL is

$$\frac{\sigma_\gamma}{\gamma} < \rho. \tag{6.16}$$

In conjunction with laser-accelerated electron beams, this condition certainly poses challenges. Calculations for an electron beam current of 100 kA yields that a Pierce parameter of the order of 1% is required. The energy spread of electron beams from laser-accelerators optimized for high beam currents is still in the order of 10%. Improving both, the energy spread and the beam current is work in progress.

6.3 First Design Consideration of a Table-Top FEL

Laser electron acceleration as introduced in chapter 2 opens up the perspective of miniaturizing fourth generation light sources. The corresponding project is called Table-Top Free-Electron-Laser (TT-FEL) and is described in the publication as shown in chapter V. This concept fundamentally differs from large scale approaches not only in terms of reducing the required acceleration distance from the kilometer scale to the centimeter scale. Also

the current of the electron beam is predicted to exceed conventional accelerators by orders of magnitude. For the case of an X-ray TT-FEL, this leads to a reduction of the saturation length from around 100 meters to a few meters. Accordingly, the required undulator length is reduced.

A laser driven XFEL would imply both, the size of the whole system reduced to university laboratory scale and a significant reduction of costs. A larger availability of high energy, ultra brilliant light sources would boost fields of applications ranging from physics via chemistry, biology and pharmacy all the way to the application as a medical device in hospitals.

The first design considerations for a laser-driven TT-FEL have been published as shown in chapter V.

In the course of this thesis concerning chapter 2, Figs. 3 and 4 have been generated as well as the calculations and deductions relating to space charge effects have been carried out.

6.4 New Quadrupole Undulator Concept

The TT-FEL project aiming at the miniaturization of the FEL setup involves a compact acceleration stage and the reduction of the saturation length. The latter is mainly due to a larger electron beam current, which requires an optimum electron beam radius σ_x [Eq. 6.12] during the propagation through the undulator device. The optimum size for a TT-FEL is at relatively small values compared to conventional FELs and influence the saturation length according to Eqs. (6.11) and (6.12). The optimum beam radius for high-current electron beams is far beyond of what can realistically be achieved using conventional dipole based undulators.

In the course of this thesis, a new undulator concept was developed which is based on magnetic quadrupole fields. A quadrupole field does not deflect an electron beam causing synchrotron radiation as it is the case with dipole fields. However, shifting a quadrupole field with a field gradient g off-axis by the distance Δx, the field acts like a dipole of the strength $g \cdot \Delta x$, superimposed with a quadrupole of the gradient g. Using this principle allows the construction of an undulator device with ultra-strong focusing properties.

The quadrupole undulator presented is based on Halbach-like permanent magnet quadrupole devices. Its realization requires miniature high-gradient quadrupole devices with a highly purified quadrupole field component. This purification can be achieving using the tuning method also developed in the course of this thesis, presented in section 4.4. The ability to tune the quadrupole devices prepares the path for the first construction of a quadrupole based undulator.

Besides the focusing properties, the ability to tune and adjust the quadrupole undulator exceeds the tuneability of dipole undulators. The dipole field components of individual undulator half-periods can be controlled without interacting with the neighboring half-

period. Tapering of a quadrupole undulator can be introduced and adjusted flexibly at the assembled device. Dipole undulators commonly incorporate specific tapering configurations already in the design stage of the device.

All analytical deductions and numerical calculations presented in chapter VI have been performed in the course of this thesis.

Chapter 7

Conclusion and Outlook

This thesis is focused on the examination of both the field of dynamics of charged particle beams and the field relating to the transport of charged particle beams. Ever since particle acceleration has existed, these fields have been the subject of investigation. The presented work demonstrates the necessity to extend these fields for laser-accelerated particle beams. In particular, for applications requiring high quality electron beams, the compulsory improvements include both, a better understanding of space charge effects as well as an increased quality of the beam optical devices.

The point-to-point space charge calculation method was examined and has lead to a significant improvement of its understanding. It was shown that widely used calculation codes exhibit substantial artifacts, in particular in relation to laser-accelerated high-current density electron beams. The origin of these artifacts have been identified and minimized. It is now possible to calculate the space charge driven expansion of a laser accelerated particle beam in an appropriate way. Therefore, this topic is of importance and of great interest for both, the plasma-based advanced accelerator and the Free-Electron-Laser (FEL) modeling communities.

Miniature magnetic beam optical devices have been characterized in detail. Possessing a small aperture, the measurement of the field distribution within the devices posed significant challenges. A simple method was developed which is based on the multipole field expansion and which allows to measure the field distribution only using a single small Hall probe.

A method was developed to tune the magnetic field distribution of Halbach type miniature magnetic multipole devices, on the basis of the ability to detect and measure the field distribution within their apertures. Due to the large ratio of beam size to aperture size, they commonly yield unwanted or even severely distorting higher order field components. For the first time we are now able to introduce specific higher order field components in a controlled manner. Thus the classification of the distorting field components, allows these to be compensated for. The ability to tune miniature beam optical devices is an absolute must for their applications within a laser-driven FEL system.

Although this thesis predominantly focuses on the treatment of electron beams, these quadrupole devices have also been successfully used for the first time to focus a laser accelerated ion beam. Using a quadrupole lens doublet at the Z-Petawatt laser system at Sandia National Laboratories, it was possible to focus the laser-accelerated ion beam onto a spot.

The use of electron beams suggest the application of undulator devices. A test undulator was built and successfully used for producing spontaneous undulator radiation at the Mainz electron accelerator MAMI. The undulator period has a length of 5 mm and, to our knowledge, is the shortest in the world. Moreover, using this undulator we succeeded in measuring laser-driven soft X-ray radiation at the MPQ.

An FEL is one of the most promising applications for laser accelerated high-current electron beams. These beams allow to reduce the saturation length of the SASE process from a hundred meter to meters. Together with the compact laser-electron accelerator, a fourth generation light source could become possible in university scale laboratories. We have carried out a first design consideration addressing the major aspects.

Trying to realize a compact FEL, a quadrupole undulator concept was developed. The reduction of the saturation length requires an average electron beam size which is comparatively small while it is propagating through the undulator device. The new concept is based on the use of the miniature magnetic quadrupole devices discussed in this thesis. Simultaneously, the new device accomplishes both, the undulator specific deflection and the focusing of the electron beam. The quadrupole undulator aims at the reduction of the average beam size by at least a factor of 6 when compared to the free drift, this significantly reduces the required undulator length of the laser-driven FEL.

7.1 Further Improvement of Multipole Devices

The tuning of the magnetic quadrupoles beyond what is presented in chapter II is work in progress. An automated adjustment apparatus is under development, which aims at significantly improving the possibilities of minimizing the distorting higher order magnetic field components. The apparatus will allow to move the magnet wedges individually in the μm regime in a reproducible and well defined way.

The apparatus for tuning the quadrupole devices is additionally used to determine the phase of the quadrupole field component at a μrad precision. The ability to precisely determine the quadrupole phases is also mandatory for achieving high quality imaging properties. The distortion of the quadrupole phases within multiplet lenses introduces severe imaging abberations.

7.2 Emittance Measurements

Emittance measurements for laser-accelerated electron beams have to be carried out in single shots since fluctuations among important beam parameters are too large from shot to shot. Most emittance measurement methods are complex experiments which usually cannot be carried out in single shot mode. Hitherto, the emittance of laser-accelerated electron beams can experimentally only be estimated very roughly. Particle-In-Cell simulations yield source sizes of $\sigma^* \approx 1\mu$m [12] and the divergence experimentally determined is in the order of $\sigma' \approx 10$ mrad. The emittance is thus $\epsilon = \sigma^* \cdot \sigma' = 10^8$ mm mrad as deduced in chapter 4. The two major uncertainties introduced in conjunction with this value are numerically determined source size and the large energy spread of these beams. Quantitative values of the beam emittance, however, are only feasible for monoenergetic beams. A good emittance measurement method, hence, has to account for the energy spread.

The approach proposed for determining the emittance ϵ is based on measuring the source size σ^* and the divergence σ' of the electron beam for a specific energy. Measuring the source size is non-trivial. The electron beam at the exit of the plasma accelerator has to be imaged e.g. onto a screen. Since the quadrupole devices have chromatic aberrations, it is only one selected energy which has a focal spot at a certain longitudinal position. Using an additional dipole magnet allows to separate the different energies on the screen. Thus, the source size for one selected energy can be directly measured within a single shot, which also includes the beam divergence. A simulation of this experiment is shown in Fig. 7.1.

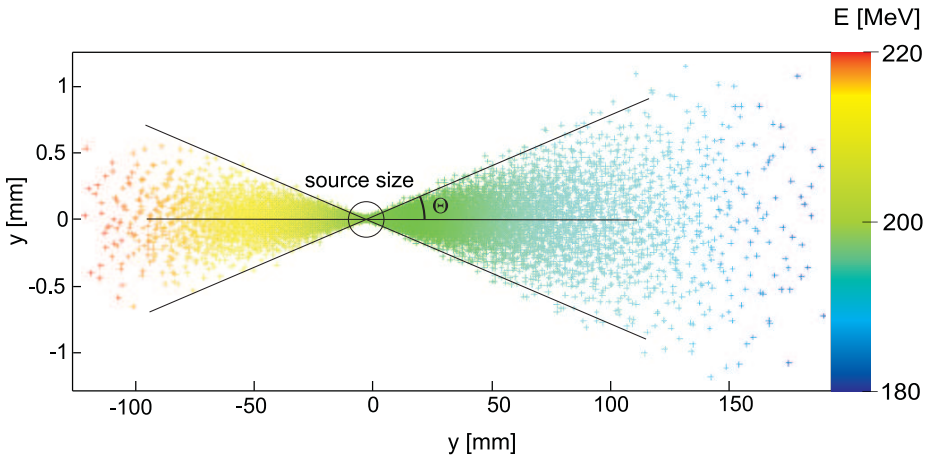

Figure 7.1: The calculated measurement signal on the screen behind the quadrupoles and the dipole is shown imaging the source at the exit of the plasma accelerator. The electron beam has an energy $E = 200$ MeV at an rms energy spread of 3.5%. The horizontal plane is deflected using a magnetic field. The source size is imaged onto the screen for a selected energy which is also 200 MeV in the calculation shown. The initial divergence of the beam can be deduced from the measured value Θ.

The critical elements of this measurement approach are the quadrupole devices. Higher order field components increase the imaged source size and thus severely disturb the measurement result. If higher order field components can be successfully minimized, the emittance measurement of a laser-accelerated electron beam could be the first important application for tuned quadrupole devices.

7.3 Building a Quadrupole Undulator

The availability of high quality miniature quadrupoles is the basis for the realization of a quadrupole undulator as proposed in chapter VI. Building a first proof-of-principle quadrupole undulator is work in progress.

7.4 FEL Amplification

We have successfully produced laser-driven soft X-ray photon beams as presented in section 5.4. The next step is the optimization of the experimental setup towards a SASE-FEL. A first mile stone would be the experimental observation of SASE signatures. The differences in the characteristics of undulator radiation and SASE radiation can be used to detect these signatures.

7.5 FEL Applications

Once SASE signatures have been detected, the next step is going into saturation obtaining an ultra-brilliant fourth generation photon beams. These beams open up a wide field of applications.

The short electron bunches as obtained from laser-electron acceleration suggests femtosecond time-resolved pump-and-probe experiments. Also the study of the interaction between soft X-ray radiation and matter yields an interesting field. A high photon flux allows nonlinear multi-photon excitation of atoms, molecules and clusters.

Once reaching the X-ray regime, a prominent application is *single molecule imaging*: The chemical properties of molecules can generally be deduced if the structure of the molecule is known. The solution of the structure presently requires the molecule to be crystallized in order to obtain sufficient intensity of the diffracted X-ray photons. There are important molecules which do not crystallize. An FEL photon beam in the X-ray regime promises a peak brilliance which is sufficient for solving the structure from the diffracted pattern of a single molecule. A method of rendering the molecular structure from the diffraction patterns was proposed by R. Neutze et al. [121]. This outlook promises a tremendous impact on structural biology.

Chapter I

On Space Charge Calculations

Title of publication:

On Retardation Effects in Space Charge Calculations Of High Current Electron Beams

The additional references [52]-[59] are included in this publication.

PHYSICAL REVIEW SPECIAL TOPICS - ACCELERATORS AND BEAMS **12**, 101301 (2009)

Retardation effects in space charge calculations of high current electron beams

S. Becker,* P. B. Hilz, F. Grüner, and D. Habs
Ludwig-Maximilians-Universität München, 85748 Garching, Germany
(Received 18 June 2009; published 22 October 2009)

Laser-plasma accelerators are expected to deliver electron bunches with high space charge fields. Several recent publications have addressed the impact of space charge effects on such bunches after the extraction into vacuum. Artifacts due to the approximation of retardation effects are addressed, which are typically either neglected or approximated. We discuss a much more appropriate calculation for the case of laser wakefield acceleration with negligible retardation artifacts due to the calculation performed in the mean rest frame. This presented calculation approach also aims at a validation of other simulation approaches.

DOI: 10.1103/PhysRevSTAB.12.101301 PACS numbers: 41.75.−i, 52.38.Kd

I. INTRODUCTION

Laser acceleration is a promising field in various aspects, such as the miniaturization of the accelerator setup and the availability of electron beams with high-current density. The plasma wakefield acceleration in the bubble regime was predicted in particle-in-cell simulations [1] and led to rapid progress in various experiments [2–5].

The effect of the charge density on the electron beam dynamics after the extraction into vacuum can be estimated when considering the electromagnetic field energy [6] per particle in the mean rest frame of the particle bunch,

$$u'_f = \frac{1}{4\pi\epsilon_0 N}\sum_{i=2}^{N}\sum_{j=1}^{i-1}\frac{q_i q_j}{|\vec{r}'_i - \vec{r}'_j|} = \frac{\epsilon_0}{2N}\int |\vec{E}(\vec{r}')|^2 d^3r', \quad (1)$$

where N is the number of charged particles considered and q_i is the charge of the particle i at the position $\vec{r}'_i$. Within the mean rest frame, the average electron velocity in the longitudinal direction is at a minimum. For a large N, a homogeneously charged sphere with a radius R scales as $u'_f \propto Q^2/R$ with Q being the total charge. Laser accelerated electron beams yield normalized field energies $u_n = u'_f/m_e c^2$ which enter a regime which is far above the one that can be reached by conventional accelerators. Space charge effects in this regime have been examined under various aspects; these are, for example, longitudinal wakefields [7,8], energy spreads introduced at the electron extraction from the plasma [9], and the temporal development of the induced energy chirp [10].

A frequently used method to calculate space charge effects consists of simulations based on point-to-point interactions (PPI). Numerical calculations based on PPI are particularly exposed to artifacts if the calculation is performed in the laboratory frame. This issue is discussed in [11] explaining the artifacts in the way PPI simulations commonly account for retardation: In the absence of the knowledge on the particles 4D trajectory, retardation is approximated by assuming constant velocities. Consequently, the acceleration of the simulated particles, i.e., the macroparticles during each finite time step, is neglected. For the regime discussed here, these artifacts are examined in detail. Much more appropriate results can be obtained when the calculation is carried out in the mean rest frame of the electron bunch using PPI. In this case, the average velocities of the macroparticles are only weakly relativistic and, consequently, the retardation artifacts are minimized. This result is then discussed in comparison with the PPI method performed in the laboratory frame and the Poisson solver. These two approaches exhibit considerable artifacts which manifest in different characteristics of the longitudinal phase space. Therefore, the design of experiments using laser accelerated electron beams could possibly be misguided, especially tabletop free-electron lasers [12], which crucially depend on the characteristics of the longitudinal phase space. The calculations here are performed using GPT [13]. The artifacts addressed, however, are not specific to the GPT code, but can be found in any code utilizing the PPI model.

II. COULOMB EXPANSION

The electron bunch considered here is cold and thus has zero divergence and zero emittance. The initial bunch configuration with a spatial Gaussian density distribution in the laboratory frame has the rms values $\sigma_x = \sigma_y = \sigma_z = 1\ \mu$m, an initial kinetic energy given by the Lorentz factor $\gamma_0 = 300$, and a total charge of $Q = 1$ nC and, hence, results in a normalized field energy of $u_n \approx 10\%$.

For obtaining a 4D trajectory, we have to make assumptions for the acceleration process: Within the plasma, any expansion driven by the Coulomb forces is suppressed due to the strong plasma fields. We can, hence, assume that the bunch is in a Gaussian shape before leaving the plasma accelerator in both relevant frames of reference, laboratory

*Corresponding author.
stefan.becker@physik.uni-muenchen.de

 © 2009 The American Physical Society

frame and the mean rest frame. The end of the plasma is assumed to be a ''sharp'' edge behind which the expanding effect of the Coulomb forces is suddenly switched on. This means that only electrons that have crossed the boundary take effectively part in the Coulomb interaction.

Mean rest frame

The mean rest frame for the case considered here is an inertial frame of reference copropagating with the electron bunch at the constant normalized velocity β_0. Before the Coulomb interaction is switched on, the Lorentz transformation leads to a bunch prolongation of a factor of γ_0. In this frame of reference, the Coulomb interaction cannot set in instantaneously and globally. Instead, the onset of the interaction starts at the front end of the bunch and spreads towards the rear end. Note that the bunch geometry in the mean rest frame leads to a transverse expansion dominating over the longitudinal debunching.

Figure 1 shows Minkowski diagrams and particle distributions in the mean rest frame of the bunch. Figure 1(a) illustrates the initial beam condition in the laboratory frame and in the mean rest frame of the electron bunch before leaving the wakefield accelerator. The bunch is assumed to exhibit a Gaussian spatial density distribution in both frames of reference. This state in the mean rest frame is also shown in Fig. 1(b) using a PPI calculation.

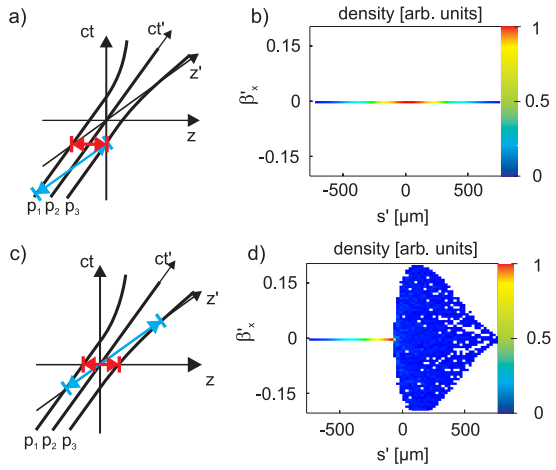

FIG. 1. (Color) The electron bunch is shown schematically in (a) at the end of the wakefield acceleration in its initial configuration using a Minkowski diagram in the laboratory frame (red) and the mean rest frame (blue). The spatial axis z is the longitudinal propagation direction. The plasma boundary is located in the laboratory frame at $z = 0$ and in the mean rest frame at $z' = 0$. p_1, p_2, and p_3 are 4D trajectories corresponding to the rear end, the center, and the front end of the bunch. Part (b) shows the beam state using a PPI simulation performed in the mean rest frame in correspondence with (a). The longitudinal bunch position s' is plotted against the normalized transverse velocity β'_x with $s' = 0$ being the center of mass. Part (c) shows the situation when half of the particles have left the plasma and (d) correspondingly in the mean rest frame at $t' = 0$.

Figure 1(c) illustrates the beam in the laboratory frame and in the mean rest frame of the electron bunch at the time $t = t' = 0$, where the plasma boundary is at the center of the bunch and moves at the constant velocity $\beta_{\mathrm{pb}} = -\beta_0$. This center of the bunch is also determined to be at the longitudinal position zero in both frames $z = z' = 0$.

In general we can state that the calculation performed in the laboratory frame does not require sophisticated assumptions concerning the initial simulation conditions, since the predominant transverse space charge interactions can be assumed to set in instantaneously: The duration of propagation of the plasma boundary in the laboratory frame is ultrafast, which means that the shape of the bunch does not significantly change during the propagation of the boundary. Therefore, simulations yield the same results for the cases of the electrostatic interaction being switched on instantaneously and the moving of the boundary through the bunch. Within the mean rest frame, however, the different ways of coincidence cause a longitudinal bunch prolongation, which can be seen from Figs. 1(a) and 1(c). Figure 1(d) shows the spatial electron density distribution being altered while the plasma boundary is still within the bunch. As a precondition, however, we can assume that the bunch has the same spatial symmetry at the end of the wakefield acceleration in both frames of reference, i.e., the mean rest frame and the laboratory frame as shown in Fig. 1(a). Since we have chosen a Gaussian density distribution, we have a spatial point symmetry for the case discussed here. The end of the acceleration distance is at $z = 0$, which requires the introduction of a constraint, whereby the onset of the Coulomb interaction propagates from the front end to the rear end of the bunch as shown in Fig. 1(c).

The further evolution of the electron bunch calculated in the mean rest frame is shown in the laboratory frame in Fig. 2. The Lorentz transformation into the laboratory frame is performed assuming constant velocity and is given by

$$\begin{aligned}
\beta_{xi} &= \frac{\beta'_{xi}}{\gamma_0(1+\beta_0\beta'_{zi})} \quad x_i = x'_i \\
\beta_{yi} &= \frac{\beta'_{yi}}{\gamma_0(1+\beta_0\beta'_{zi})} \quad y_i = y'_i \\
\beta_{zi} &= \frac{\beta'_{zi}+\beta_0}{1+\beta_0\beta'_{zi}} \quad z_i = \frac{z'_i}{\gamma_0(1+\beta_0\beta'_{zi})},
\end{aligned} \tag{2}$$

where $z_i(z'_i)$ is obtained using linear extrapolation in the (z, ct) space. A slice is a longitudinal subsection of the bunch. The small slice energy spread can be explained regarding the longitudinal phase space in the mean rest frame [Fig. 2(b)]: Particles with the highest values of γ' originate from the regions with the highest initial electro-

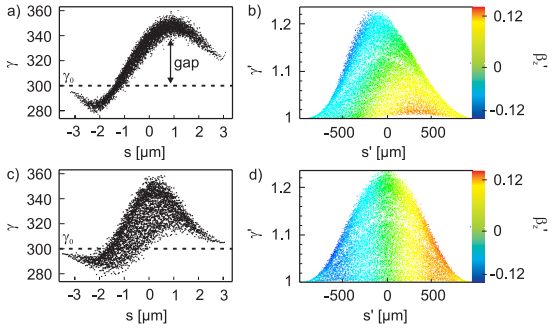

FIG. 2. (Color) The further evolution of the bunch in Fig. 1 is shown 3 ps later in the longitudinal phase space with the calculations performed in the mean rest frame. Part (a) displays the longitudinal phase space of the bunch transformed to the laboratory frame using Eqs. (2). The slice energy spread yields significantly smaller values than the total energy spread of the bunch. This fact also leads to a gap in the phase space. The reason for this property can be seen in (b), where the longitudinal phase space is drawn with the longitudinal normalized velocity color coded in the mean rest frame. The plasma boundary leads to an asymmetric particle distribution in the mean rest frame. The instantaneous onset of the Coulomb interaction in the mean rest frame would lead to a symmetric particle distribution as shown in (c) and (d) in a direct comparison after 0.7 ps of expansion.

static fields, i.e., in the longitudinal direction along the axis around the center of the bunch and transversely from off axis. In contrast to the laboratory frame, the bunch shape in the mean rest frame changes significantly already during the propagation of the plasma boundary [Fig. 1(d)]. The off-axis electrons close to the boundary are predominantly accelerated towards the rear (left) end of the bunch and therefore pushing on-axis electrons towards the head as a result of momentum conservation. Because of the Lorentz transformation $\gamma = \gamma_0\gamma'(1 + \beta_0\beta'_z)$ for a particle at a certain position s', a larger value of γ' is reduced by a negative value of β'_z and a smaller γ' is boosted by a positive β'_z. Finally, particles with different values of γ' obtain virtually the same γ in the laboratory frame, which leads to the "gap," i.e., the small slice energy spread for electrons at a specific bunch position s as can be seen in Fig. 2(a).

A symmetric particle distribution in the mean rest frame would be obtained from the instantaneous onset of the Coulomb interaction and is shown in Figs. 2(c) and 2(d). The phase space does not yield the correlation described above and, thus, the slice energy spread is larger.

III. COMPARISON OF CALCULATION APPROACHES

The calculation of the space charge driven expansion is examined using PPI according to [6,13,14]. The electromagnetic fields are calculated relativistically, where radiation effects are neglected and retardation is treated in accordance with the constant velocity approximation. The Coulomb field of particle j acting on i is given in the rest frame of j by

$$\vec{E}'_{j\to i} = \frac{Q\vec{r}'_{ji}}{4\pi\epsilon_0|\vec{r}'_{ji}|^3}, \tag{3}$$

$$\vec{r}'_{ji} = \vec{r}_{ji} + \frac{\gamma_j^2}{\gamma_j + 1}(\vec{r}_{ji}\cdot\vec{\beta}_j)\vec{\beta}_j = \vec{r}'_i - \vec{r}'_j, \tag{4}$$

with Q being the charge of the macroparticles and $\vec{r}'_{ji}$ being the distance between the particles in the rest frame of j. The Lorentz transformation of the electromagnetic fields of particle j acting on i in the laboratory frame yields

$$\begin{aligned}\vec{E}_{j\to i} &= \gamma_j\left[\vec{E}'_{j\to i} - \frac{\gamma_j^2}{\gamma_j + 1}(\vec{\beta}_j\cdot\vec{E}'_{j\to i})\vec{\beta}_j\right],\\ \vec{B}_{j\to i} &= \frac{\gamma_j\vec{\beta}_j\times\vec{E}'_{j\to i}}{c}.\end{aligned} \tag{5}$$

A tracking code [13] applying Eqs. (5) is used to calculate the free drift of the considered electron bunch in vacuum. Figure 3 compares results of different calculation methods at a later point in time than Fig. 2. The appropriate calculation using PPI performed in the mean rest frame is shown in the column I′ of Fig. 3. The results being Lorentz transformed are shown in column I of Fig. 3. The slice energy spread (column I of Fig. 3(c)) is larger compared to the one shown in Fig. 2(a), because debunching effects on larger propagation distances cause a longitudinal phase space as displayed in Fig. 2(b) developing towards the one as in Fig. 2(d). Column II of Fig. 3 shows the PPI calculation performed in the laboratory frame. The difference in comparison with column I of Fig. 3 can be explained with retardation artifacts due to the constant velocity approximation as described in [11]. A further method besides PPI treating space charge is the application of Poisson solvers, which evaluate the electrostatic space charge field in the mean rest frame of the bunch, where magnetic fields are neglected occurring due to relative velocities. The Lorentz transformation into the laboratory frame introduces the magnetic fields. In this respect, the Poisson solvers referred to solve the equations of motion in the laboratory frame. The calculation time using this method linearly scales with the number of macroparticles and thus allows many more macroparticles to be considered. We evaluated a calculation using PPI performed in the mean rest frame of the bunch as it would be obtained from a Poisson solver by using the fields

$$\vec{E}'_{j\to i} = \frac{Q\vec{r}'_{ji}}{4\pi\epsilon_0|\vec{r}'_{ji}|^3}, \qquad \vec{B}'_{j\to i} = 0. \tag{6}$$

We obtained virtually identical results for the example

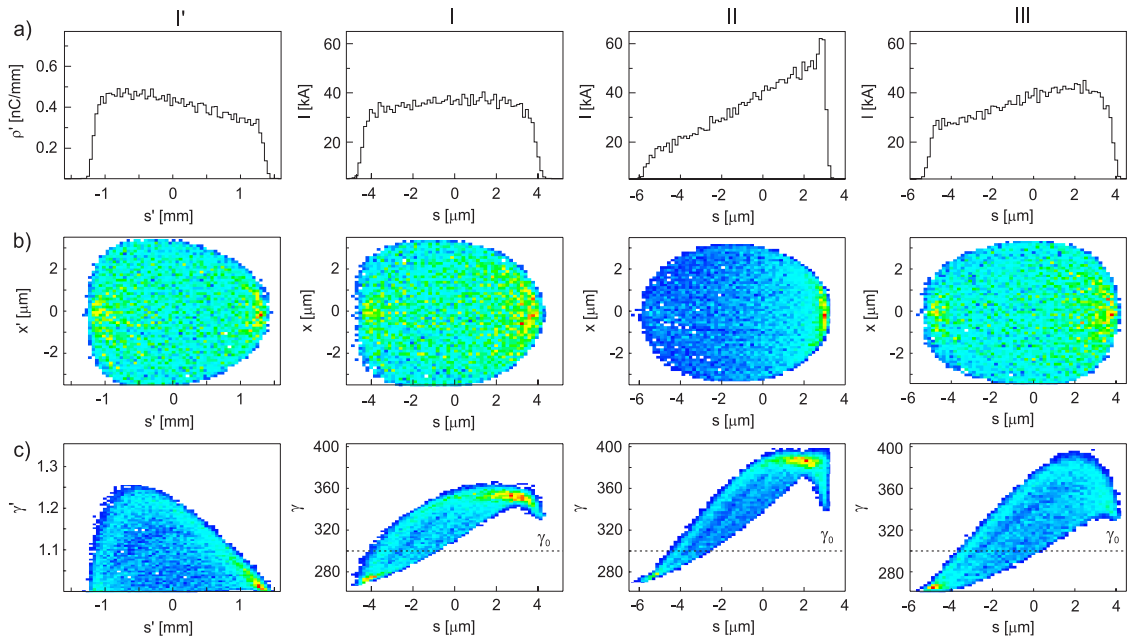

FIG. 3. (Color) Calculation of the vacuum expansion of the considered electron bunch is shown with the initial state as illustrated in Fig. 1 after the propagation distance of 1.8 m corresponding to 6 ns in the laboratory frame or after 20 ps in the mean rest frame. The center of mass is located at $s = 0 = \sum_i \gamma_i(t) s_i(t) / \sum_i \gamma_i(t)$. Panels in column I′ show the calculation with negligible retardation artifacts in the mean rest frame and panels in column I show the Lorentz-transformed results [Eqs. (2)] in the laboratory frame. Column II shows the PPI calculation performed in the laboratory frame and column III shows the calculation result corresponding to a Poisson solver, both with instantaneous onset of the Coulomb interaction. The longitudinal spatial inner bunch position is plotted in the mean rest frame (s') and in the laboratory frame (s). Part (a) in column I′ shows the line charge density distribution, parts (b) and (c) in column I′ show the bunch current. Both of these representations are proportional to the longitudinal particle density. Row (b) shows the spatial particle density distribution with the transverse coordinate plotted in the mean rest frame (x') and in the laboratory frame (x). Row (c) shows the longitudinal phase space. The color coding is linear and equivalent to the one of parts (b) and (d) in Fig. 1.

bunch considered here comparing the cases utilizing Eqs. (5) and utilizing Eqs. (6) in the mean rest frame. Thus, the case examined here yields an appropriate treatment with respect to the retardation artifacts when utilizing a Poisson solver. However, the electromagnetic field being obtained in the mean rest frame also requires the correct consideration of the 4D trajectories of the bunch particles as described above. The result of Poisson solvers assuming instantaneous onset of the Coulomb interaction leads to a longitudinal phase space [Fig. 2(c)], where the slice energy spread within the laboratory frame is shown to be overestimated compared to the case of correct initial conditions applied [Fig. 2(a)]. To our knowledge, the instantaneous onset of the Coulomb interaction is assumed among the vast majority of codes which are widely applied and which utilize the method of a Poisson solver. In addition, more realistic simulation scenarios might involve particle bunches having a notable energy spread or divergence. In

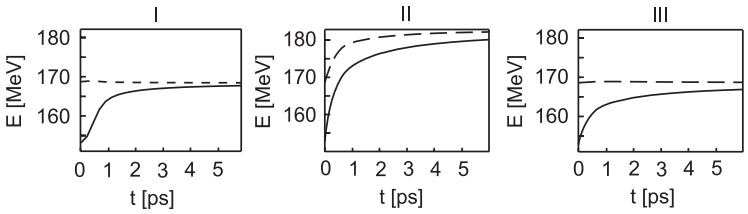

FIG. 4. The solid line shows the kinetic energy. The dashed line shows the total energy which is the sum of kinetic energy and field energy using Eq. (1). The calculations correspond to Fig. 3.

these cases, velocities in the mean rest frame might not allow one to neglect the magnetic fields, where PPI codes using Eqs. (5) being performed in the mean rest frame of the bunch yield the least artifacts. Figures 2(c) and 2(d) and column III of Fig. 3 show results as obtained from a Poisson solver at a later point in time. Coulomb interaction is considered in the mean rest frame and is assumed to set in instantaneously. This wrong initial condition leads to the difference compared to column I of Fig. 3. Considering energy conservation for the example beam in Fig. 4 yields the total energy being conserved in the case of the calculation performed in the mean rest frame of the electron bunch and for the case using the Poisson solver.

IV. CONCLUSION

The method discussed allows the calculation of the electron bunch evolution with negligible retardation artifacts in a space charge regime which could be reached by laser acceleration. This calculation is performed in the mean rest frame of the bunch, where the relative velocities are only weakly relativistic. Moreover, the required Lorentz transformation between the laboratory frame and the mean rest frame is shown to be nontrivial, since assumptions concerning the 4D trajectories of the particles of the bunch have to be made. The result of this calculation is compared with the results of two commonly applied methods, one using PPI performed in the laboratory frame and one using a Poisson solver. For different reasons, both approaches yield significant deviations concerning the characteristics of the longitudinal phase space, which could ultimately mislead the design of applications using laser accelerated electron bunches: A PPI simulation performed in the laboratory frame principally suffers from retardation artifacts, which leads to the violation of energy and momentum conservation and to a wrong spatial density distribution. The temporal development of the energy chirp within the longitudinal phase space is overestimated and, thus, the examinations in [10] describe an upper boundary. The artifacts obtained from the method of using a Poisson solver as considered here have two causes. The first cause originates from codes which solve the equations of motion within the laboratory frame. This approach principally suffers from a Lorentz transformation which has to be done in every time step. Some implementations were found to apply the Lorentz transformation for the longitudinal spatial position by merely linearly stretching the bunch by the Lorentz factor corresponding to the velocity of the mean rest frame. Using $z(z')$ as in Eq. (2), instead, helps improving the result. This transformation still assumes constant velocity, which might introduce artifacts due to the Coulomb driven bunch expansion. The second cause for artifacts originates from not considering the propagation of the plasma boundary through the electron bunch within the mean rest frame and thus, incorrect initial conditions. These are, however, no principal problems involved and, thus, appropriate results can be obtained using a Poisson solver if three conditions are met: First, the electrostatic space charge field in the mean rest frame has to be calculated correctly (the solver might not converge). Second, the equations of motion have to be solved in the mean rest frame to avoid Lorentz transformations (the beam line elements have to be transformed into the mean rest frame only once). Third, the initial conditions have to be considered correctly. Since the solver almost scales linearly with the number of particles in terms of CPU time, many more particles can be considered than using the PPI model and thus could be the preferred method. However, we have shown here that in the space charge regime considered, one has to be thoughtful about assumptions made. The PPI model only uses the Coulomb interaction and is thus based on fundamental principles. This model, applied as discussed here, is therefore recommended for validating results of other calculation methods.

ACKNOWLEDGMENTS

We thank M. Dohlus (DESY) for fruitful discussions. This work has been funded by the DFG through transregio TR18 and supported by the DFG Cluster-of-Excellence Munich Center for Advanced Photonics MAP.

[1] A. Pukhov and J. Meyer-ter-Vehn, Appl. Phys. B **74**, 355 (2002).
[2] S. P. D. Mangles *et al.*, Nature (London) **431**, 535 (2004).
[3] C. G. R. Geddes *et al.*, Nature (London) **431**, 538 (2004).
[4] W. P. Leemans *et al.*, Nature Phys. **2**, 696 (2006).
[5] J. Osterhoff *et al.*, Phys. Rev. Lett. **101**, 085002 (2008).
[6] J. D. Jackson, *Classical Electrodynamics* (Wiley & Sons, New York, 1999).
[7] R. A. Bosch, Phys. Rev. ST Accel. Beams **10**, 050701 (2007).
[8] G. Geloni, E. Saldin, E. Schneidmiller, and M. Yurkov, Nucl. Instrum. Methods Phys. Res., Sect. A **578**, 34 (2007).
[9] G. Stupakov and Z. Huang, Phys. Rev. ST Accel. Beams **11**, 014401 (2008).
[10] F. Grüner, C. Schroeder, A. R. Maier, S. Becker, and Y. M. Mikhailova, Phys. Rev. ST Accel. Beams **12**, 020701 (2009).
[11] G. Fubiani, J. Qiang, E. Esarey, W. P. Leemans, and G. Dugan, Phys. Rev. ST Accel. Beams **9**, 064402 (2006).
[12] F. Grüner *et al.*, Appl. Phys. B **86**, 431 (2007).
[13] General Particle Tracer, www.pulsar.nl.
[14] B. van der Geer and M. de Loos, Ph.D. thesis, Technische Universiteit Eindhoven, 2001.

Chapter II

Tunable Permanent Magnet Quadrupoles

Title of publication:

Characterization and Tuning of Ultra High Gradient Permanent Magnet Quadrupoles

The additional references [60]-[70] are included in this publication.

PHYSICAL REVIEW SPECIAL TOPICS - ACCELERATORS AND BEAMS **12**, 102801 (2009)

Characterization and tuning of ultrahigh gradient permanent magnet quadrupoles

S. Becker,[1,*] M. Bussmann,[2] S. Raith,[1] M. Fuchs,[1] R. Weingartner,[1] P. Kunz,[3] W. Lauth,[3] U. Schramm,[2] M. El Ghazaly,[3] F. Grüner,[1,4] H. Backe,[3] and D. Habs[1]

[1]*Ludwig-Maximilians-Universität München, 85748 Garching, Germany*
[2]*Forschungszentrum Dresden-Rossendorf FZD, 01314 Dresden, Germany*
[3]*Institut für Kernphysik, Universität Mainz, 55099 Mainz, Germany*
[4]*Max-Planck-Institut für Quantenoptik, 85748 Garching, Germany*

(Received 13 February 2009; published 19 October 2009)

The application of quadrupole devices with high field gradients and small apertures requires precise control over higher order multipole field components. We present a new scheme for performance control and tuning, which allows the illumination of most of the quadrupole device aperture because of the reduction of higher order field components. Consequently, the size of the aperture can be minimized to match the beam size achieving field gradients of up to 500 $\mathrm{T\,m^{-1}}$ at good imaging quality. The characterization method based on a Hall probe measurement and a Fourier analysis was confirmed using the high quality electron beam at the Mainz Microtron MAMI.

DOI: 10.1103/PhysRevSTAB.12.102801 PACS numbers: 41.85.Lc, 52.38.Kd

I. INTRODUCTION

High field gradient compact quadrupole devices have recently been the subject of an increasing amount of attention, in particular, as a compact element for beam manipulation in laser based particle acceleration. Permanent magnet quadrupole devices (PMQs) with a small aperture can reach high magnetic field gradients because of maintaining high surface magnetization. A number of design approaches have been developed and realized such as pure PMQs [1,2] in accordance with a Halbach design [3] or as modified (hybrid) Halbach quadrupole devices utilizing saturated iron to guide the magnetic field [4,5].

While being of importance in compact accelerator setups, the main interest in PMQs lies in focusing particle beams of high divergence such as laser accelerated ion beams [6] and electron beams [7–9]. The control of the field quality as introduced in this work opens the path for using PMQs as focusing elements in free-electron lasers [10] having a demand on high quality beam transport systems. Multipole field components higher than the quadrupole field component have distorting effects on the electron beam and therefore increase the beam emittance. These higher order multipole field components (HOMFC) have to be minimized.

Assuming a constant ratio of the HOMFC and the pure quadrupole field component at a given radius, small aperture approaches typically suffer from a strong influence of the HOMFC on the beam quality as the beam size to aperture is large compared to commonly used electromagnetic quadrupole devices.

*Corresponding author.
stefan.becker@physik.uni-muenchen.de

We present a method of tuning PMQs in order to achieve control over higher order field components; this allows the significant reduction of HOMFC and thus allows a large ratio of beam size to aperture.

Halbach-type PMQs where built using 12 wedges (Fig. 1). The permanent magnet material is NdFeB [11] with a remanent field of 1.3 T. The assembled PMQ reaches surface magnetization fields of 1.5 T. The ability to reduce the aperture size compared to electromagnetic quadrupole devices allows the realization of field gradients of up to 500 $\mathrm{T\,m^{-1}}$ at an aperture diameter of 6 mm. Conventional electromagnetic quadrupole devices require a larger aperture and yield thus gradients of typically only 50 $\mathrm{T\,m^{-1}}$. These devices, however, usually allow the gradient to be adjusted which is not possible with a simple approach using PMQs. The PMQs as applied here were preliminarily tested and presented in [1].

Small apertures pose challenges in the measurement of the magnetic field distribution within. Common approaches involve the application of Hall probes to determine the field gradients or rotating coils to determine

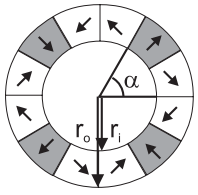

FIG. 1. Design of a miniature PMQ is shown with 12 wedges of permanent magnet. The inner radius of the aperture is r_i = 3 mm and the outer radius is r_o = 10 mm. The arrows point in the magnetization direction.

 © 2009 The American Physical Society

HOMFC. This poses challenges in fabrication of the miniature coil and, in particular, suppressing vibrations during the measurement [12,13]. We present a method allowing the measurement of all relevant magnetic vector field components relying solely on a miniature Hall probe which can be applied to very small apertures at the precision required.

The ability to measure all relevant field components within small apertures allows the introduction of specific HOMFC by changing the position of individual magnet segments. We are thus able to compensate for undesired field components and also deliberately introduce specific components such as octupoles for compensating spherical aberrations or dodecapoles for compensating the effect of fringe fields. In order to minimize the influence of the correction of one field component on the entire field distribution, we apply materials with negligible nonlinear interactions with the magnetic field due to hysteresis effects. Finally, we present measurement results of the tuning of the magnetic field distribution.

II. MEASURING FIELD COMPONENTS

The principle presented here for the measurement of the magnetic field involves a Hall probe.

The magnetic field is scanned in cylindrical coordinates, as shown in Fig. 2: The PMQ is mounted on a rotating stage for controlling the φ coordinate. From the center of rotation, a displacement of the Hall probe along the y axis scans the radial field component B_ρ, whereas the displacement along the x axis scans the azimuthal component B_φ. The offset of $\varphi = 90°$ between B_ρ and B_φ has to be considered.

This method requires the knowledge of the position of the geometrical center of rotation which does not necessarily coincide with the center, i.e., the minimum value, of the magnetic field distribution. The procedure for finding the geometrical center involves a simple feedback algorithm which only requires the Hall probe signal. The result of this iteration is unique as the field changes monotonously from a point inside the aperture.

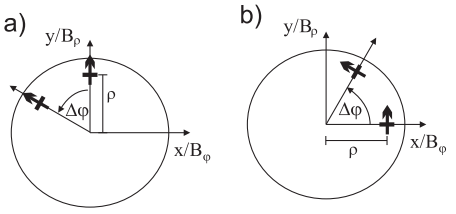

FIG. 2. Scheme of measuring the magnetic vector field in cylindrical coordinates using a Hall probe with the arrow being the surface normal. The radial component (a) as well as the azimuthal component (b) are obtained separately.

A. Fourier analysis

A direct measurement of the entire magnetic field for $0 < \rho < \rho_0$ in cylindrical coordinates inside the aperture overdetermines the magnetic vector field. The assumption of $B_z = 0$ leads to the expansion of the magnetic field using polar coordinates of

$$\vec{B}(\rho, \varphi) = \sum_{l=1}^{\infty} [B_{l\rho}(\rho, \varphi)\vec{e}_\rho + B_{l\varphi}(\rho, \varphi)\vec{e}_\varphi] \qquad (1)$$

with

$$B_{l\rho}(\rho, \varphi) = \rho^{l-1}[a_l \sin(l\varphi) + b_l \cos(l\varphi)] \qquad (2)$$

$$B_{l\varphi}(\rho, \varphi) = \rho^{l-1}[a_l \cos(l\varphi) - b_l \sin(l\varphi)], \qquad (3)$$

a_l and b_l being coefficients representing the HOMFC. The case $B_z \neq 0$ would imply fringe fields, which are discussed in the next section.

Measuring either the B_ρ or the B_φ field component on a single ring [Figs. 3(a) and 3(b)] is sufficient for a complete determination of the magnetic vector field. A Fourier expansion of a ring with the radius ρ_0 leads to the desired coefficients a_l and b_l in magnitude $\sqrt{a_l^2 + b_l^2}$ [Fig. 3(c)] and phase $\arctan(b_l/a_l)$ [Fig. 3(d)] allowing one to construct the vector field [Eq. (1)] using either

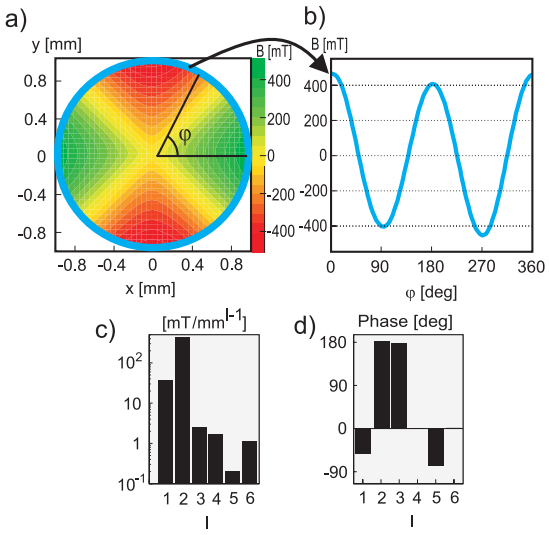

FIG. 3. (Color) Part (a) shows a field measurement using the azimuthal component in cylindrical coordinates and part (b) its outermost ring at $\rho_0 = 1$ mm is plotted against one rotation and used to expand the field coefficients a_l and b_l, shown in (c) magnitude $\sqrt{a_l^2 + b_l^2}$ and (d) phase $\arctan(b_l/a_l)$.

$$a_l = \frac{1}{\pi}\int_0^{2\pi} \rho_0^{1-l} B_\varphi(\rho_0, \varphi)\cos(l\varphi)d\varphi$$
$$b_l = -\frac{1}{\pi}\int_0^{2\pi} \rho_0^{1-l} B_\varphi(\rho_0, \varphi)\sin(l\varphi)d\varphi \quad (4)$$

or

$$a_l = \frac{1}{\pi}\int_0^{2\pi} \rho_0^{1-l} B_\rho(\rho_0, \varphi)\sin(l\varphi)d\varphi$$
$$b_l = \frac{1}{\pi}\int_0^{2\pi} \rho_0^{1-l} B_\rho(\rho_0, \varphi)\cos(l\varphi)d\varphi. \quad (5)$$

B. Proof of principle

The Hall probe used here has a relatively large active probe diameter of 740 μm compared to the aperture of 6 mm. The center of rotation can be determined with micrometer precision in spite of the large probe area. The radius ρ_0 was chosen to be 1 mm, which was the maximum value for the measurements presented here due to the physical size of the entire specific Hall probe device applied. The tilt error of the probe limits the accuracy to sub-5 μm precision for the setup used here. Knowing the absolute positioning error of the geometrical center, we obtain a relative error of $\Delta\rho_0/\rho_0 = 0.5\%$ for $\rho_0 = 1$ mm.

The measurement errors for B_φ or B_ρ and the resolution can be estimated by calculating the remainder:

$$O_k = \int_0^{2\pi} \left| B_{\rho/\varphi}(\rho_0, \varphi) - \sum_{l=1}^{k} B_{l\rho/\varphi}(\rho_0, \varphi) \right| d\varphi. \quad (6)$$

For all field measurements performed, we find contributions of orders up to the sixth (the dodecapole) as is shown by the remainder in Fig. 4(b). This result is expected from the symmetry considerations of the design of the PMQ, but one has to take into account resolution constraints due to the size of the Hall probe, which can make the measurement insensitive to higher order components. Measurement noise or signal drifts would significantly increase the remainder. Such an increase has not been observed in the measurement, indicating that these influences are clearly negligible up to at least the dodecapole order. The maximum order identified by a Hall probe of diameter d_H can be estimated by assuming that the magnetic field is integrated homogeneously over the active area of the probe. An azimuthal variation in field strength as depicted in Fig. 3 can only be resolved if the diameter of the hall probe is smaller than the circumference of the ring of radius ρ_0 over which the variation is measured. For the case considered here with $\rho_0 = 1$ mm and diameter $d_H = 740$ μm, we find that the maximum order component that can be resolved is thus given by $l'_{max} = 2\pi\rho_0/d_H = 8$. Please note that a measurement of the azimuthal field component B_φ does not underlie this resolution limit. For the Halbach quadrupole design only tuning up to the dodecapole ($l = 6$) is required as explained later in Sec. IV. Thus, with the Hall probe available all relevant orders can be resolved, however, one has to consider the measurement error induced by the finite Hall probe size as explained in the following. For each HOMFC l separately one integrates over the active Hall probe surface Ω. The surface has the area $\pi d_H^2/4$ with radial (ρ) or azimuthal (φ) orientation. Using either the coefficient a or b yields the same result. Here, we picked a and obtain

$$B_{\mathrm{int},l,\rho/\varphi}(a_l, \rho, \varphi) = \frac{4}{\pi d_H^2}\int_{\Omega_{\rho/\varphi}} B_{l,\rho/\varphi}(a_l, \rho', \varphi')\cdot dA', \quad (7)$$

with

$$B_{l,\rho}(a_l, \rho, \varphi) = \rho^{l-1} a_l \sin(l\varphi)$$
$$B_{l,\varphi}(a_l, \rho, \varphi) = \rho^{l-1} a_l \cos(l\varphi), \quad (8)$$

following Eq. (3). Using Eqs. (4) and (5) we determine the correction factors,

$$f_{l,\varphi} = \frac{\frac{1}{\pi}\int_0^{2\pi} \rho_0^{1-l} B_{\mathrm{int},l,\varphi}(a_l, \rho_0, \varphi)\cos(l\varphi)d\varphi}{a_l}$$
$$f_{l,\rho} = \frac{\frac{1}{\pi}\int_0^{2\pi} \rho_0^{1-l} B_{\mathrm{int},l,\rho}(a_l, \rho_0, \varphi)\sin(l\varphi)d\varphi}{a_l}. \quad (9)$$

For our case, the factors are given in Table I.

When measuring the radial change in field strength by varying ρ, the Hall probe area integrates over a certain azimuthal variation in φ. This integration yields a value less than the maximum field strength at distance ρ and thus measuring B_ρ underestimates the absolute strength of the HOMFC. For the azimuthal variation the Hall probe inte-

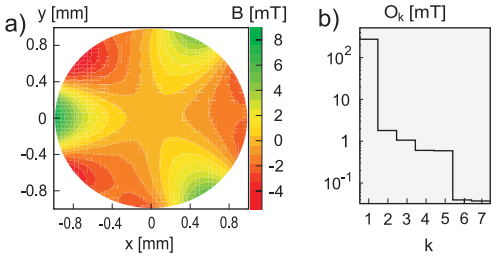

FIG. 4. (Color) Part (a) shows the azimuthal HOMFC from Fig. 3 ($\vec{B} = \sum_{l=3}^{6}[B_{l\rho}(\rho, \varphi)\vec{e}_\rho + B_{l\varphi}(\rho, \varphi)\vec{e}_\varphi]$, note the absolute scale compared to Fig. 3). Part (b) shows the remainder after the kth field component.

TABLE I. Factors f correcting the expanded values of the radial measurement ρ and the azimuthal measurement φ specific to the Hall probe used here.

l	2	3	4	5	6
$f_{l,\rho}$	0.83	0.70	0.54	0.36	0.17
$f_{l,\varphi}$	1	1.05	1.14	1.29	1.49

grates over $B_\varphi(\rho) \propto \rho^{l-1}$ which leads to an overestimation of the HOMFC strength for $l > 2$, since the increase in field strength with increasing distance $\rho > \rho_0$ is not compensated by the reduced field strength measured for $\rho < \rho_0$.

The Hall probe applied here has an enhanced sensitivity in the center of the semiconductor knowing the active Hall probe area. If only the area of the semiconductor is known, one might have to account for an inhomogeneous sensitivity within the area due to the joins to the semiconductor. This is described in [14,15] in detail.

C. Fringe fields

The calculation of the field components from the ring measurement (Fig. 3) requires the assumption of $B_z = 0$ as mentioned before. Hence, the measurement of the ring used for the field expansion must not be performed in the fringes of the field distribution for the expansion following Eq. (1).

There are cases, however, where fringe fields cannot be neglected, in particular when particle beams are being focused to waist sizes on the nanometer scale. Fringe fields are discussed in [3] for Halbach-type PMQs. However, in practice, this does not determine the effect of fringe fields on a beam in a general way. Even if the design of the device and thus the field distribution including the fringe field is known in detail, the final effect on the beam still depends on the length of the PMQ and only works for specific beam properties, which in turn allows the determination of specific HOMFC for compensating the effect of the fringe fields. The method presented here can be used to introduce field components in order to compensate the fringe field.

III. FOCUS MEASUREMENT AT MAMI ELECTRON BEAM

The PMQs as introduced in [1] have been applied at the accelerator MAMI to acquire the imaging quality. These measurements have been carried out prior to the ability to tune the devices. A PMQ lens doublet was used to focus the electron beam. The method of expanding the magnetic field distribution from a Hall probe measurement was applied to reproduce the experimental results.

The beam profile was monitored by a pair of 4 μm wires movable longitudinally in the direction of the beam propagation and transversely through the beam, both in the horizontal and the vertical direction. Bremsstrahlung caused by the beam hitting the wire was detected using an ionization chamber in the forward direction. The Bremsstrahlung's intensity, measured while changing the position of the wires transversely to the beam, determines the beam shape at a certain longitudinal position. The MAMI electron beam can reach energies of up to 855 MeV. We used energies of 270 MeV with an energy stability of $\Delta E/E = 10^{-5}$ and an emittance of 2 nm rad horizontally and 0.7 nm rad vertically.

The calculation of the beam transport involves an expansion of the magnetic fields of the quadrupoles following Eqs. (4) and (5) and tracking the electron beam [16] using the field map given by Eq. (1) and correcting for the Hall probe size following Table I.

The results are shown in Fig. 5 choosing two beam configurations: A convergent electron beam of small size at the entrance of the lens doublet (panel I of Fig. 5), and a

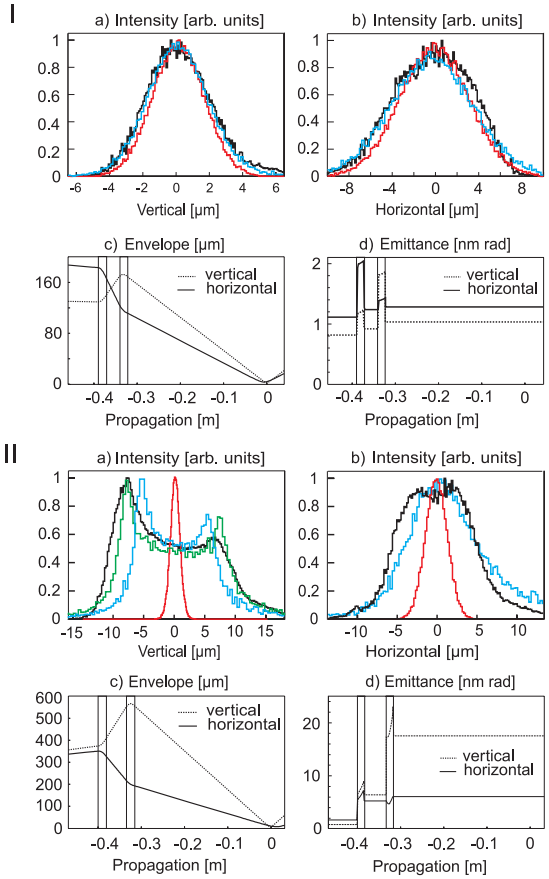

FIG. 5. (Color) Measurements at the Mainz Microtron MAMI are shown with two different beam configurations: The small electron beam configuration (panel I) is shown with the horizontal (Ia) and vertical (Ib) beam plane at the waist. The measured beam (black), the calculated beam using expanded fields (blue), and calculated beam for an ideal quadrupole field (red) are shown for comparison. The calculated beam envelope (Ic) and the emittance (Id) are plotted against the propagation direction of the beam. The vertical lines mark the PMQ positions. The large beam configuration is shown correspondingly (panel II). The green curve in panel IIa is computed from the expanded fields, but with a different focal spot slightly moved towards the PMQs by 1 mm or 0.5% of the focal length.

divergent beam of larger size (panel II of Fig. 5). As expected, the small-beam configuration yields a measured waist size only being a little larger than that of an ideal quadrupole with the same gradient. The waist size of the transport calculation using the expanded fields agrees well with the measured beam waist. The emittance remains virtually constant.

Higher order field components significantly distort the electron beam profile for the large beam configuration, the beam size increases compared to the case of an ideal PMQ doublet, and the form becomes asymmetric as depicted in Ia and Ib of Fig. 5. This distortion is qualitatively described when taking into account the HOMFCs for the computation of the beam evolution. The effect of the HOMFC can also be seen in the evolution of the trace space emittance [17], as is shown in panels Id and IId of Fig. 5. Here, the emittance is deduced from the calculation using the expanded field distribution of the PMQs.

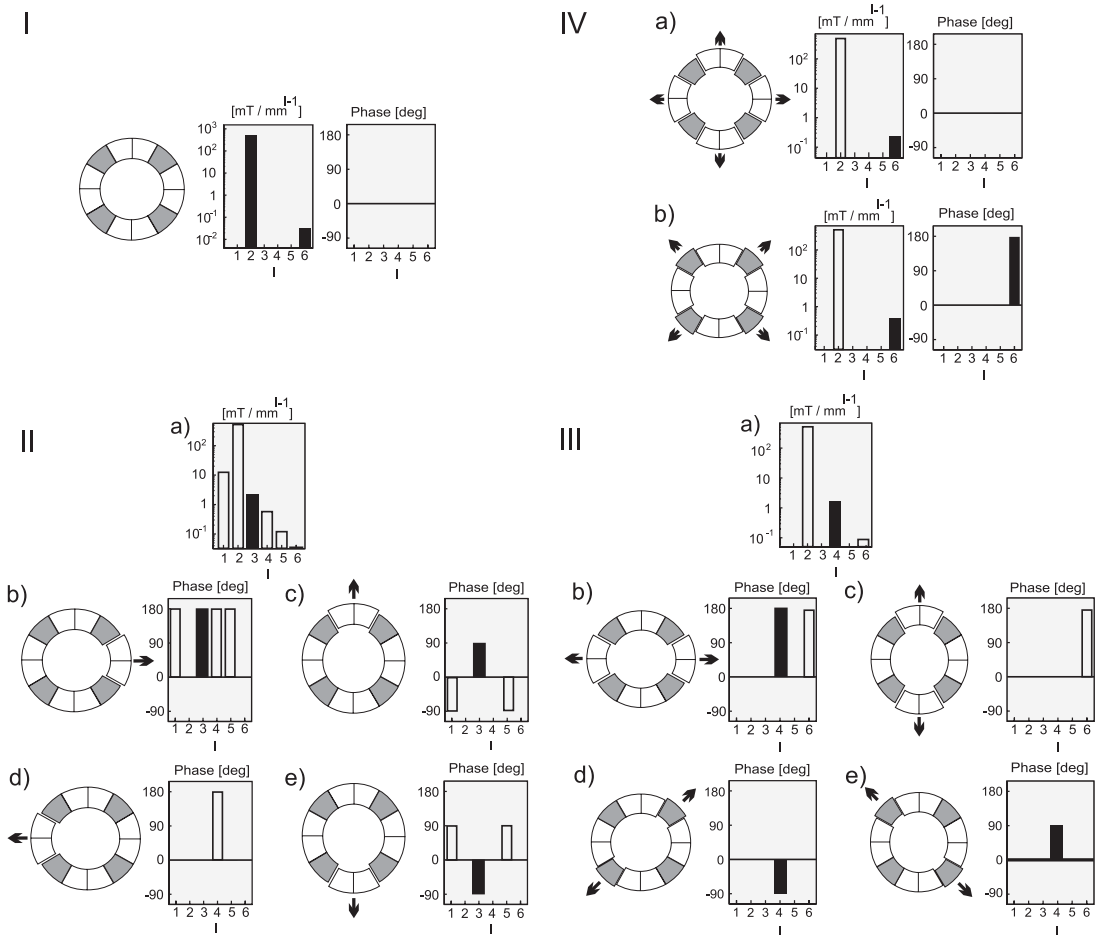

FIG. 6. The introduction of HOMFC with the PMQ having the same orientation as in Fig. 1. Panel I: Magnitude and phases of the calculated magnetic field using the ideal arrangement of permanent magnet wedges. Panel II: Displacing a single pair of tuning wedges by 150 μm introduces a dominant sextupole (IIa). Independent from the specific pairs of tuning wedges displaced, panels IIb–IIe show the effect on the phases of the introduced field components by moving tuning wedges at $\alpha = 0°$, 90°, 180°, 270°. Panel III: Two opposite pairs of tuning wedges are displaced by 150 μm, this introduces a dominant octupole. Panel IIIa shows the effect on the magnitude of the field components. Panel IIIb–IIIc show the effect on the phases of the introduced field components moving tuning wedges at $\alpha = 0°$ and 90° affecting a_4. Moving the positioning wedges as shown in panels IIId–IIIe affect b_4. Panel IV: All pairs of tuning wedges are displaced by 150 μm; this introduces a dominant dodecapole. The effect on the magnitudes are shown in panel IVa. Panels IVb and IVc show distinct pairs of tuning wedges which are moved and the effect on magnitudes and phases of the field components. The application of distance holders might be required as in Fig. 7(b).

There can be several reasons for this mismatch, but we constrain ourself to discussing only those effects that have to be considered when aligning the PMQs, namely an offset of the azimuthal angle φ of the lenses with respect to the beam axis and the absolute position of the lens doublet in the lattice. An offset in φ rotating the PMQs by a few hundred μrad already compensates for the absolute difference between measured and calculated beam waist. However, it also significantly distorts the form of the beam profile and can thus be ruled out for the case discussed here. A change in the absolute position of the lens doublet on the subpercent level changes the absolute beam size while maintaining the form of the transverse beam profile, as shown in IIa of Fig. 5, where the lenses are moved 1 mm away from the beam profile monitor, yielding the green curve which matches well the measured profile. This shows that precise measurement and control of the magnetic field as well as precise alignment of the PMQs are required in order to reproduce the computed beam properties in the experiment.

IV. MAGNETIC FIELD TUNING

HOMFC can have a variety of origins, for example, variations of the shape of the wedges or the magnetization direction or strength. The knowledge of the specific origin of an undesired higher order field component is not necessary for its compensation: The introduction of a field component in the same order and magnitude but with a phase shift of 180° leads to its elimination.

Displacing certain wedges introduces well-defined higher order field components which can be used for correcting manufacturing deviations of the wedges, the housing, or for modeling the magnetic field distribution correcting imaging aberrations.

A. Wedge positioning

Figure 7 schematically shows the assembly of permanent magnet wedges within the housing. The four wedges with the magnetic field oriented towards the device axis, which in the following are called positioning wedges, experience centripetal magnetic forces. A thin nonmagnetic cylinder is placed inside the aperture. Its radius determines the radial distance of the wedges from the axis of the device [panels 7(a) and 7(b)]. The positioning wedges are tightened with positioning screws from the housing for fixing the cylinder. The center of the magnetic field can be adjusted to coincide with the geometrical center of the PMQ for the elimination of the dipole field components.

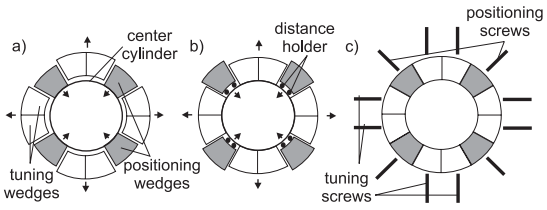

FIG. 7. Part (a) shows an arrangement of permanent magnet wedges and the center cylinder is shown schematically. The arrows point in the direction of the magnetic forces which act centrifugally and centripetally on the wedges. (b) Example for distance holders (e.g. 50–100 μm aluminum foil) of the positioning wedges from the cylinder center. (c) Positioning and tuning screws acting on the wedges.

Magnetic forces centrifugally repel the four remaining pairs of wedges, called tuning wedges in the following. In combination with tuning screws, these forces allow their precise positioning. Since the magnetic forces are acting on the tuning wedges as a pair, the tuning screws are arranged in parallel [panel 7(c)].

B. Introduction of field components

The field distribution is altered by modifying the PMQ by selecting tuning wedges and moving these. The field distribution of a modified PMQ is calculated numerically [18] for obtaining the quantitative effect on individual field components including their phase. The result of the calculation is expanded [Eqs. (4) and (5)] and used for obtaining a table of reference for the effect of moving tuning pairs on the field distribution as shown in Fig. 6.

We first consider the undisturbed quadrupole design in panel I of Fig. 6. Owing to the symmetry of the design, only a dodecapole superimposes on the quadrupole field. Panel II of Fig. 6 shows a dominant sextupole ($l = 3$) which is introduced when moving one pair of tuning wedges. For symmetry reasons, a pure sextupole component cannot be introduced, but an octupole component is also obtained which in turn can be eliminated. The introduction of an octupole component is achieved by moving opposite pairs of wedges as shown in panel III of Fig. 6. Changing b_4 [Eq. (3)] without influencing a_4 requires the movement of the positioning wedges which can be achieved by, e.g., introducing distance holders as is shown in Fig. 7. Alternatively, b_4 can be modified by moving two individual tuning wedges which are arranged at opposite locations from the device center which requires a subsequent compensation of the additionally introduced a_4 component. The introduction of a dodecapole field is shown in panel IV of Fig. 6. Depending on the desired phase, the application of distance holders might be required as is shown in panel 7(b).

C. Adjustment results

Figure 8(a) shows an example of a newly assembled quadrupole. Because of manufacturing deviations of either the wedges or the housing, there is a considerable initial sextupole field component. After compensating for the higher order field components, a much purer quadrupole field is obtained as is shown in Fig. 8, demonstrating the

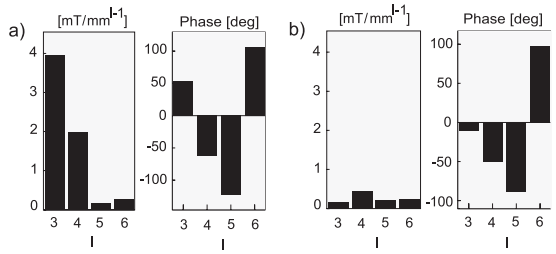

FIG. 8. HOMFC for the proof of principle are illustrated, which are obtained from azimuthal field measurements. Part (a) shows the HOMFC within a newly assembled quadrupole and (b) shows the PMQ tuned with significantly reduced HOMFC. The statistical errors obtained from independent measurements are between 0.1% and 0.7% for the values of the HOMFC, the phases are off between 0.3° and 1°, and are thus negligible.

feasibility of the method discussed. The errors of these measurements correspond to those errors discussed in panel 4(b), since the apparatus used is the same.

V. CONCLUSION

The method presented allows one to shape the magnetic field distribution of a PMQ. The magnetic field distribution is determined from a Fourier expansion of a Hall probe measurement and used as the basis for identifying the tuning wedges to be moved for obtaining the desired field distribution. The precise quantification of HOMFC in conjunction with the complete control of the field configuration allows one to accurately configure the magnetic field distribution to a high degree. After only a few iterations, magnitude and phase of the undesired field components can be reduced significantly. Hence, the control over these field components up to at least the dodecapole allows a larger ratio of the quadrupole's aperture to be illuminated. Moreover, HOMFC such as an octupole or dodecapole can be introduced in order to compensate for imaging aberrations and fringe fields effects.

The advantage of the pure permanent magnet devices over hybrid quadrupole designs lies in the linear superposition of the magnetic field contributions of the individual segments. This allows a decoupled tuning process, and thus a fast and simple adjustment of the magnetic field distribution. The compensation scheme shown here still has potential for improvement since the results presented in this publication were obtained by manually tuning the PMQs. The method for the reduction of HOMFC can easily be automated using simple algorithms which allow one to move the wedges at higher precision.

ACKNOWLEDGMENTS

This work has been funded by the DFG through transregio TR18 and supported by the DFG cluster-of-excellence Munich Center for Advanced Photonics MAP.

[1] T. Eichner, F. Grüner, S. Becker, M. Fuchs, U. Schramm, R. Weingartner, D. Habs, H. Backe, P. Kunz, and W. Lauth, Phys. Rev. ST Accel. Beams **10**, 082401 (2007).
[2] J. K. Lim, P. Frigola, G. Travish, J. B. Rosenzweig, S. G. Anderson, W. J. Brown, J. S. Jacob, C. L. Robbins, and A. M. Tremaine, Phys. Rev. ST Accel. Beams **8**, 072401 (2005).
[3] K. Halbach, Nucl. Instrum. Methods **187**, 109 (1981).
[4] T. Mihara, Y. Iwashita, M. Kumada, and C. M. Spencer, in Proceedings of the 12th Linear Accelerator Conference, Lübeck, Germany, 2004 (SLAC Report No. SLAC-PUB-10878).
[5] C. M. S. Sears, R. L. Byer, E. R. Colby, B. M. Cowan, R. Ischebeck, M. R. Lincoln, T. Plettner, R. H. Siemann, and J. E. Spencer, in Proceedings of the 12th Advanced Accelerator Concepts Workshop, Lake Geneva, Wisconsin, 2005 (SLAC Report No. SLAC-PUB-12422).
[6] M. Schollmeier, S. Becker, M. Geißel, K. A. Flippo, A. Blažević, S. A. Gaillard, D. C. Gautier, F. Grüner, K. Harres, M. Kimmel, F. Nürnberg, P. Rambo, U. Schramm, J. Schreiber, J. Schütrumpf, J. Schwarz, N. A. Tahir, B. Atherton, D. Habs, B. M. Hegelich, and M. Roth, Phys. Rev. Lett. **101**, 055004 (2008).
[7] S. P. D. Mangles, C. Murphy, Z. Najmudin, A. Thomas, J. Collier, A. Dangor, E. Divall, P. Foster, J. Gallacher, C. Hooker, D. Jaroszynski, A. Langley, W. Mori, P. Norreys, F. Tsung, R. Viskup, B. Walton, and K. Krushelnick, Nature (London) **431**, 535 (2004).
[8] C. G. R. Geddes, C. Toth, J. van Tilborg, E. Esarey, C. Schroeder, D. Bruhwiller, C. Nieter, J. Cary, and W. Leemans, Nature (London) **431**, 538 (2004).
[9] J. Faure, Y. Glinec, A. Pukhov, S. Kiselev, S. Gordienko, E. Lefebvre, J.-P. Rousseau, F. Burgy, and V. Malka, Nature (London) **431**, 541 (2004).
[10] F. Grüner, S. Becker, U. Schramm, T. Eichner, M. Fuchs, R. Weingartner, D. Habs, J. Meyer-ter-Vehn, M. Geissler, M. Ferrario, L. Serafini, B. an der Geer, H. Backe, W. Lauth, and S. Reiche, Appl. Phys. B **86**, 431 (2007).
[11] Vacuumschmelze Hanau, Vacodym 764 HR data sheets (2005), www.vacuumschmelze.com.
[12] G. Datzmann, G. Dollinger, G. Hinderer, and H.-J. Körner, Nucl. Instrum. Methods Phys. Res., Sect. B **158**, 74 (1999).
[13] Y. Iwashita, T. Mihara, M. Kumada, and C. M. Spencer, *Proceedings of the 21st Particle Accelerator Conference, Knoxville, 2005* (IEEE, Piscataway, NJ, 2005).
[14] I. Hlásnik and J. Kokavec, *Hall Generator in Inhomogenous Field and Dipole Notion of the Hall Effect*, Solid State Electronics (Pergamon Press, New York, 1966), Vol. 9, pp. 585–594.
[15] V. Yu. Korovkin, Izmeritel'naya Tekhnika **8**, 50 (1988).
[16] General Particle Tracer, www.pulsar.nl.
[17] K. Flöttmann, Phys. Rev. ST Accel. Beams **6**, 034202 (2003).
[18] CST EM Studio, www.cst.com.

Chapter III

Ion Focusing

Title of publication:

Controlled transport and focusing of laser-accelerated protons with miniature magnetic devices

The additional references [71]-[100] are included in this publication.

PRL 101, 055004 (2008) PHYSICAL REVIEW LETTERS week ending 1 AUGUST 2008

Controlled Transport and Focusing of Laser-Accelerated Protons with Miniature Magnetic Devices

M. Schollmeier,[1] S. Becker,[2] M. Geißel,[3] K. A. Flippo,[4] A. Blažević,[5] S. A. Gaillard,[4,6] D. C. Gautier,[4] F. Grüner,[2] K. Harres,[1] M. Kimmel,[3] F. Nürnberg,[1] P. Rambo,[3] U. Schramm,[7] J. Schreiber,[2] J. Schütrumpf,[1] J. Schwarz,[3] N. A. Tahir,[5] B. Atherton,[3] D. Habs,[2] B. M. Hegelich,[2,4] and M. Roth[1]

[1]*Institut für Kernphysik, Technische Universität Darmstadt, Schloßgartenstrasse 9, D-64289 Darmstadt, Germany*
[2]*Department für Physik, Ludwig-Maximilians Universität München, Am Coulombwall 1, D-85748 Garching, Germany*
[3]*Sandia National Laboratories, Albuquerque, New Mexico 87185, USA*
[4]*Los Alamos National Laboratory, Los Alamos, New Mexico 87545, USA*
[5]*GSI—Gesellschaft für Schwerionenforschung mbH, Plasmaphysik, Planckstrasse 1, D-64291 Darmstadt, Germany*
[6]*Physics Department, University of Nevada, Reno, MS220, Reno, Nevada 89557, USA*
[7]*Forschungszentrum Dresden–Rossendorf, Bautzner Landstraße 128, D-01328 Dresden, Germany*

(Received 17 April 2008; published 1 August 2008)

This Letter demonstrates the transporting and focusing of laser-accelerated 14 MeV protons by permanent magnet miniature quadrupole lenses providing field gradients of up to 500 T/m. The approach is highly reproducible and predictable, leading to a focal spot of (286×173) μm full width at half maximum 50 cm behind the source. It decouples the relativistic laser-proton acceleration from the beam transport, paving the way to optimize both separately. The collimation and the subsequent energy selection obtained are perfectly applicable for upcoming high-energy, high-repetition rate laser systems.

DOI: 10.1103/PhysRevLett.101.055004 PACS numbers: 52.38.Kd, 41.85.Lc, 52.59.−f

The realization of intense and energetic laser pulses has resulted in enormous scientific activity over the past decade due to many potential applications including the generation of giga-electron-volt, narrow band electron pulses [1], intense x-ray pulses [2], laser-driven nuclear phenomena [3], inertial fusion energy [4,5], as well as the acceleration of protons from hydrocarbon impurities and heavy ions to mega-electron-volt energies from thin foil targets [6–9]. These ion beams (particularly protons) are generated in a very robust and reproducible way with up to 10^{13} protons by the target normal sheath acceleration mechanism [10]. The ions are accelerated, forming a quasineutral plasma with an exponential energy spectrum that exhibits a sharp cutoff at its maximum energy [11]. Unlike conventionally accelerated ion beams, they contain very high particle numbers in short, picosecond pulses and have unprecedented emittance; i.e., the beams expand in a very laminar fashion [12]. These features make them useful as a diagnostic tool (e.g., proton radiography of transient processes [13]) and they could have applications as compact particle accelerators [14] for the creation of high-energy density (HED) matter [15] or for proton fast ignition [5].

There have been attempts to optimize the source for a more monochromatic beam by using a very thin proton- or carbon-rich layer on the target rear side [16,17]. But, especially for the latter applications, a collimated or focused beam, that maintains the high particle number emitted from a usual foil, is indispensable. Since the beam is divergent with an energy-dependent half-opening angle of up to 40° [18], there have been attempts at ballistic focusing by curving the target foil to a submillimeter half-sphere [15]. However, the focal length is on the order of the sphere's radius, limiting its application. Another possibility for focusing the protons is the ultrafast laser-driven microlens [19] that uses a second laser pulse to create a hot plasma expansion towards the axis of symmetry inside a tiny cylinder. The rapidly varying electric field of the plasma is used to focus traversing protons. The experimental scheme suffers from a complicated geometry with two synchronized high-intensity laser beams that need to be carefully aligned and temporally adjusted. Kar *et al.* [20] recently succeeded in partly collimating the proton beam by combining a microlens device with a flat target foil into a single piece, at the expense of a complex target assembly.

In this Letter an alternative and straightforward approach is presented that uses an ion optical system consisting of novel permanent magnet miniature quadrupoles (PMQ) with strong field gradients of up to 500 T/m, originally developed for laser-accelerated electrons [21]. A set of two PMQs demonstrates transport and focusing of laser-accelerated protons in a very reproducible and predictable manner. This approach uses permanent magnets that do not need to be replaced, hence allowing the application in upcoming high-energy, high-repetition rate lasers. Moreover, it decouples the acceleration process from the beam transport, allowing for independent optimization of the proton beam generation and of the focusing mechanism.

An initial experiment was carried out at the TRIDENT chirped pulse amplification (CPA) laser system at Los Alamos National Laboratory, and obtained a line focus, whereas the demonstration experiments with a point focus were carried out at the *Z*-Petawatt at Sandia National Laboratories (SNL) [22]. The CPA laser at SNL with a wavelength of 1053 nm delivered 40 J laser energy on target, focused by an off-axis parabolic mirror to a beam

 © 2008 The American Physical Society

PRL 101, 055004 (2008) PHYSICAL REVIEW LETTERS week ending 1 AUGUST 2008

spot of 5 μm FWHM. With a pulse duration less than 1 ps, the intensity on the target front side was $I > 5 \times 10^{19}$ W/cm^2. The prepulse contrast ratio was measured as 10^{-7}. A 25 μm thin Cu foil was used as the target, being hit by the p-polarized laser at an angle of 45°. The accelerated protons were detected with a stack of calibrated radiochromic films (RCF) [23]. The calibration for proton energy deposition was done at the tandem linear accelerator at the Max-Planck-Institut für Kernphysik in Heidelberg, Germany. The stacks in the experiment consisted of eight layers of type HD-810 and nine layers of MD-V2-55. Parasitic radiation and target debris require the RCF stacks to be wrapped in 16.3 μm aluminum foil for shielding. The energy-loss response functions of the stacks were calculated with a ray-tracing algorithm using energy-loss values from SRIM-2006 [24], taking into account the different material compositions of the different types of RCF. Because of the Bragg peak of the ion's energy loss at the end of their range, each RCF layer can be attributed to a small energy interval of 1 MeV for MD-V2-55 and 0.5 MeV for HD-810, respectively. Hence, a stack of RCF layers is a two-dimensional imaging spectrometer.

The experimental configuration is shown in Fig. 1. One RCF stack was placed at (40 ± 1) mm behind the target, detecting the divergent proton beam. The axial aperture was 5 mm throughout the PMQ beam transport section. Beam blocks consisting of 12.7 mm aluminum or 6.35 mm stainless steel protected the PMQs from debris and unwanted irradiation. The magnetic fields were calculated using a Maxwell-compliant solver for their specific design [25]. These fields were used to determine the positions of the PMQs and the spectrometer with a tracking algorithm [26]. The goal was to focus 14 MeV protons, since this energy is in the central region of the proton energy spectrum usually produced at TRIDENT and Z-Petawatt. The first PMQ was placed at a distance of 170 mm behind the target and the second one was placed at 230 mm. The focal spot was expected 500 mm behind the target, where another RCF stack was placed.

Protons from hydrocarbon contaminations at the foil's rear side were accelerated up to well above 22 MeV, which

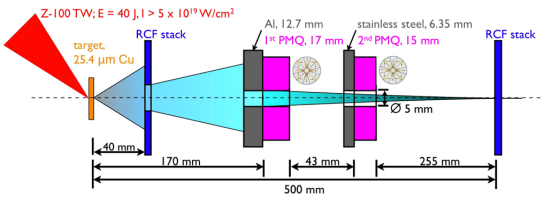

FIG. 1 (color online). Scheme of the experimental setup. A high-intensity laser pulse irradiates a Cu foil. Protons from the rear side propagate into a RCF stack with a 5 mm axial aperture for the detection of the initial beam. The transmitted protons enter two PMQ devices that transport and focus the beam. Another RCF stack in the focal plane records the intensity distribution of the protons.

is the upper detection limit of the RCF stacks used. Although RCF is sensitive to all ionizing radiation, it is most sensitive to protons due to their higher stopping power compared to electrons or x rays. Heavy ions only penetrate the first layer. The total number of protons and their energy spectrum were obtained from the first RCF stack by interpolating over the aperture in the center. High-energy protons were stopped in RCF layers at the end of the stack. Some energy, however, is deposited in the layers before. This fact requires each layer to be deconvolved by the nonlinear detector's response functions. The resulting particle number spectrum dN/dE per unit energy follows the shape obtained in Ref. [11], $dN/dE = N_0/(2Ek_BT)^{1/2} \exp[-(2E/k_BT)^{1/2}]$, with parameters $N_0 = 4.9 \times 10^{12}$ and $k_BT = 1.24$ MeV.

A typical beam profile of (14 ± 1) MeV protons is shown in Fig. 2(a). The white spot in the center is due to a hole allowing for the propagation of the protons through the PMQs. The beam profile shows intensity modulations that originate from microcorrugations of the target rear surface [27]. The beam has a diameter of (29.5 ± 2) mm that corresponds to a (20° ± 1.5°) half-opening angle. A summation of the total signal in Fig. 2(a) leads to 1.3×10^{10} protons with (14 ± 1) MeV. About 7.5×10^8 protons entered the PMQs. This number corresponds to 7.5% of the beam injected into the PMQs. The integration over the spectrum yields a conversion efficiency of 1% of the laser energy into protons with energies above 4 MeV, in agreement with Ref. [11]. The focusing effect of (14 ± 1) MeV protons 50 cm behind the target is shown in Fig. 2(b). By integrating over the peak, a total number of 8.4×10^5 protons is obtained. Hence the transmission through the magnets was $8.4 \times 10^5/7.5 \times 10^8 = 0.1\%$. This was expected, since the first PMQ focused the beam in one plane and defocused the protons in the perpendicular one. The second PMQ's aperture then cut most of the beam.

Although the PMQs were not especially designed for this beam, a small focal spot was obtained. The spot size was by far not limited by the emittance, which is on the order of $10^{-3}\pi$ mm mrad [12]. Simulation results show good agreement with the experiment [Fig. 2(c)]. The RCF was simulated using protons with a Gaussian initial energy distribution of $E = 14$ MeV and standard deviation $\sigma = 1$ MeV. The PMQ's aperture encircles the solid angle of the ion beam by orders of magnitude, justifying the assumption of a uniform initial particle distribution within a much smaller solid angle in order to achieve the best possible statistics for the simulation. The number of macroparticles was 10^6. Interactions (i.e., space charge) were neglected. The horizontal and vertical lineouts of both experiment and simulation (Fig. 3) can be well described by a Lorentzian $f(x) = \sigma/(x^2 + \sigma^2)$ with FWHM $2\sigma = 286$ μm (173 μm) horizontally (vertically), which corresponds to a decrease of the proton beam compared to an unfocused beam of approximately 10^3 times. An estimate based on the simulations for an optimized setup suggests a

PRL 101, 055004 (2008) PHYSICAL REVIEW LETTERS week ending 1 AUGUST 2008

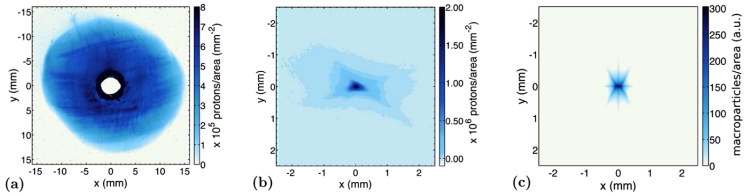

FIG. 2 (color online). (a) Beam profile of (14 ± 1) MeV protons at 40 mm behind the target. The white disk in the center is due to a hole allowing for the propagation of the protons through the PMQs. (b) Beam spot 500 mm behind the target. 8.4×10^5 protons were focused to a small spot by the PMQs. The color map in (b) was optimized to show the weak background signal; therefore, the film appears to have a signal over the whole area. (c) The simulation with a tracking code neglecting emittance shows good agreement with the experiment. The respective RCF was simulated using (14 ± 1) MeV protons.

decrease in the focal spot by an additional factor of 5 in both planes, leading to a demagnification by a factor of $5 \times 5 \times 10^3 = 2.5 \times 10^4$.

Such a small focus is still below the space-charge limit, which can be estimated by the generalized perveance, entrance radius, and focal spot size [28]. Assuming a pulse duration of 0.7 ns from the drift difference of (14 ± 1) MeV protons, the space-charge limit for an optimized focus with 5 mm aperture PMQs corresponds to $\approx 10^9$ protons.

The chromatic properties of PMQs yield an energy-dependent focal spot size. Figure 4(a) shows the ion energy spectrum integrated over an area of 200 μm in diameter. The circles represent the measured data using the PMQ doublet and the solid red line displays the calculated proton spectrum for comparison, using the first RCF stack, under the assumption of an undisturbed propagation of the beam to the same distance. The energy-dependent flux increase due to the focusing is shown in Fig. 4(b). For this specific PMQ configuration, the flux increase for (14 ± 1) MeV protons peaked at about a factor of 75. This allows the system to be used as a spatial filter in order to monochromatize the ion energy spectrum. For an optimization and increased coupling efficiency into the ion optics section, the magnets can be placed closer to the source in combination with an increased aperture of the second PMQ. The latter becomes necessary due to defocusing of the first PMQ in one plane, as well as the space-charge limitation mentioned above that decreases with increasing entrance radius.

Since the ions are emitted in the form of a quasineutral plasma, the question arises of whether or not the copropagating electrons can be safely removed close to the source without distorting the beam, i.e., without increasing the emittance. This was tested experimentally by placing a dipole magnet with 150 mT field strength at a distance of 3 mm behind the target to deflect the electrons, similar to the experiment in Ref. [12], but in our case the magnet was placed much closer to the proton source. A fine mesh (110 μm wire distance, 35 μm wire thickness) that imprints in the beam [29] was placed at the dipole entrance. The protons were recorded with a RCF stack after a drift of 100 mm. The absence of electrons could lead to space-charge forces that diminish the beam quality. However, the image showed a clear imprint of the mesh without any distortion; hence, the beam quality was unchanged. One-dimensional particle-in-cell simulations with the plasma simulation code (PSC) [30] support these findings and show that the magnetic field was sufficient to remove the comoving electrons. Both measurement and simulation demonstrate that even as close as 3 mm from the target a magnetic field can be used to control and transport the ion beam.

These results open up a realm of possibilities for applications; for instance, with an optimized configuration, the transport and focusing of all ions within a certain energy interval could be obtained. It could be used for studies of HED matter by focusing these ions to a small beam spot. The PMQs would allow for a large distance between the proton-production foil and the sample, hence for clean experiments since possible preheating by high-energy photons and electrons [31] would be significantly reduced. As

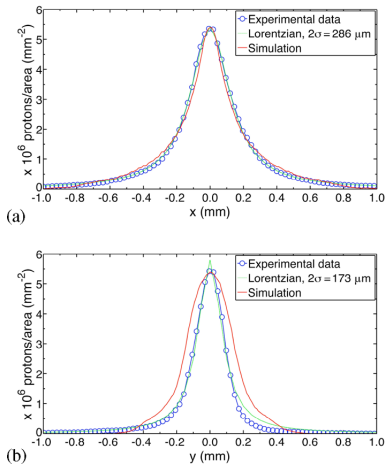

FIG. 3 (color online). Intensity profiles through the beam spot in Fig. 2. The circles show the experimental data, the dark gray (red) lines represent a lineout through the simulated beam profile. Both curves agree well with Lorentzian fits [light gray (green) lines] with a FWHM of $2\sigma = 286$ μm horizontally (a) and even 173 μm vertically (b).

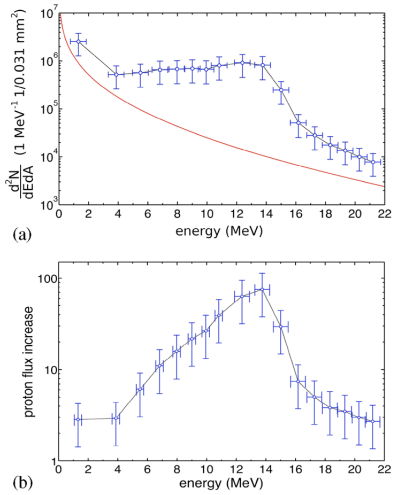

FIG. 4 (color online). (a) 500 mm behind the target the proton beam without the PMQs exhibits an exponentially decreasing spectrum (red solid line). The curve was fit to the RCF data in front of the PMQs adjusted under the assumption of an undisturbed propagation. The spectrum achieved with PMQs (circles) shows a strong signal enhancement which peaks at the designed energy of 14 MeV. (b) The peak of the energy-dependent proton flux increase at 14 MeV shows nearly 75 times more protons per area compared to the case without magnetic lenses.

an example, the HED state of matter that is exposed to 10^{11} protons with 15 MeV, focused to a small spot of 10 μm diameter, was calculated with a semiempirical equation-of-state model [32]. 10 μm thin Al, Ni, and Pb foils were chosen to sample matter from low to high nuclear charge. The energy of the protons is sufficient to penetrate the foil, and the energy deposition is very homogeneous since the Bragg peak is outside the foil. The total specific energy deposition is 505.6 kJ/g for Al, 409.3 kJ/g for Ni, and 277 kJ/g for Pb, respectively. The fast energy deposition by the protons leads to an isochoric heating that transforms the former solid foil to liquid HED matter with temperatures around 20 eV/k_B and around 10 Mbar pressure. This extreme state of matter could be found inside giant planets like Jupiter or Saturn.

In conclusion, the first transport and focusing of laser-accelerated protons with magnetic quadrupole lenses has been shown, which demonstrates the manipulation of laser-accelerated protons by magnetic fields can be done easily, even though the protons are emitted in a quasineutral plasma from the source. The further development and optimization of the magnetic beam transport and focusing system could have significant impact in various areas such as accelerator physics, inertial fusion energy, astrophysics, or even radio oncology (e.g., laser-accelerated hadron therapy for tumor treatment).

We acknowledge the expert support from the TRIDENT and *Z*-Petawatt laser facilities. M. S. thanks H. Ruhl for the PSC. The Darmstadt and Munich groups are supported by VI-VH-144 (VIPBUL). K. A. F., D. C. G., and B. M. H. were funded under LANL Laboratory Directed Research and Development Program, LDRD-DR No. 20040064. Sandia is operated by Lockheed Martin Corp. for the U.S. DOE (Contract No. DE-AC04-94AL85000). S. A. G. is funded under U.S. DOE Grant No. DE-FC52-01NV14050. The Munich group is supported by DFG TR18 and by the Munich Center for Advanced Photonics MAP.

[1] W. P. Leemans *et al.*, Nature Phys. **2**, 696 (2006).
[2] M. M. Murnane *et al.*, Science **251**, 531 (1991).
[3] K. W. D. Ledingham *et al.*, Science **300**, 1107 (2003).
[4] M. Tabak *et al.*, Phys. Plasmas **1**, 1626 (1994).
[5] M. Roth *et al.*, Phys. Rev. Lett. **86**, 436 (2001).
[6] R. A. Snavely *et al.*, Phys. Rev. Lett. **85**, 2945 (2000).
[7] E. L. Clark *et al.*, Phys. Rev. Lett. **84**, 670 (2000).
[8] A. Maksimchuk *et al.*, Phys. Rev. Lett. **84**, 4108 (2000).
[9] M. Hegelich *et al.*, Phys. Rev. Lett. **89**, 085002 (2002).
[10] S. C. Wilks *et al.*, Phys. Plasmas **8**, 542 (2001).
[11] J. Fuchs *et al.*, Nature Phys. **2**, 48 (2006).
[12] T. E. Cowan *et al.*, Phys. Rev. Lett. **92**, 204801 (2004).
[13] L. Romagnani *et al.*, Phys. Rev. Lett. **95**, 195001 (2005).
[14] A. Pukhov, Phys. Rev. Lett. **86**, 3562 (2001).
[15] P. K. Patel *et al.*, Phys. Rev. Lett. **91**, 125004 (2003).
[16] B. M. Hegelich *et al.*, Nature (London) **439**, 441 (2006).
[17] H. Schwoerer *et al.*, Nature (London) **439**, 445 (2006).
[18] M. Zepf *et al.*, Phys. Rev. Lett. **90**, 064801 (2003).
[19] T. Toncian *et al.*, Science **312**, 410 (2006).
[20] S. Kar *et al.*, Phys. Rev. Lett. **100**, 105004 (2008).
[21] T. Eichner *et al.*, Phys. Rev. ST Accel. Beams **10**, 082401 (2007).
[22] J. Schwarz *et al.*, J. Phys. Conf. Ser. **112**, 032020 (2008).
[23] GAFchromic radiochromic film types HD-810 and MD-V2-55 are trademarks of ISP corporation.
[24] J. F. Ziegler, J. P. Biersack, and U. Littmark, *The Stopping and Range of Ions in Solids* (Pergamon, New York, 1985).
[25] CST GmbH, http://www.cst.com.
[26] Pulsar Physics, http://www.pulsar.nl.
[27] M. Roth *et al.*, Phys. Rev. ST Accel. Beams **5**, 061301 (2002).
[28] S. Humphries, Jr., *Charged Particle Beams* (John Wiley and Sons, New York, 1990).
[29] M. Borghesi *et al.* Phys. Rev. Lett. **92**, 055003 (2004).
[30] M. Bonitz, G. Bertsch, V. S. Filinov, and H. Ruhl, *Introduction to Computational Methods in Many Body Physics* (Cambridge University Press, Cambridge, England, 2004).
[31] E. Brambrink *et al.*, Phys. Rev. E **75**, 065401(R) (2007).
[32] A. V. Bushman, I. V. Lomonosov, and V. E. Fortov, *Equations of State for Materials at High Energy Density* (Institute of Problems of Chemical Physics, Moskow, Chernogolovka, 1992), in Russian.

Chapter IV

Dipole Undulator

Title of publication:

Miniature magnetic devices for laser-based, table-top free-electron-lasers

The additional references [101]-[120] are included in this publication.

PHYSICAL REVIEW SPECIAL TOPICS - ACCELERATORS AND BEAMS **10**, 082401 (2007)

Miniature magnetic devices for laser-based, table-top free-electron lasers

T. Eichner,[1] F. Grüner,[1] S. Becker,[1] M. Fuchs,[1] D. Habs,[1] R. Weingartner,[1] U. Schramm,[1,2,*] H. Backe,[3] P. Kunz,[3] and W. Lauth[3]

[1]*Department für Physik, LMU München, 85748 Garching, Germany*
[2]*Forschungszentrum Dresden-Rossendorf FZD, 01314 Dresden, Germany*
[3]*Institut für Kernphysik, Universität Mainz, 55099 Mainz, Germany*

(Received 30 March 2007; published 17 August 2007)

Truly table-top sized radiation sources based on compact laser-plasma accelerators require compact and strong focusing devices and efficient short-period undulators. Complementing our recent theoretical work on the feasibility of a table-top FEL, we here present the design and successful experimental characterizations of a 5 mm period length undulator and miniature quadrupole magnets with field gradients of the order of 500 T/m.

DOI: 10.1103/PhysRevSTAB.10.082401 PACS numbers: 41.85.Lc, 41.60.Cr, 41.75.Jv, 52.38.Kd

I. INTRODUCTION

Over the past few years, laser-plasma acceleration of electrons [1–3] has rapidly advanced into a controllable technique [4,5] that is now widely discussed for first applications. Appealing features of laser-plasma accelerators are the mm-scale size that is required for the generation of GeV electron energies [4] and the high peak currents of up to 100 kA combined with short bunch lengths on the 10 fs scale [6]. Especially the latter suggests the application of laser-accelerated electron bunches as drivers for secondary light sources, either via incoherent synchrotron radiation [7], undulator radiation, or coherent FEL (free-electron laser) radiation [8].

Although the laser-plasma accelerator can be regarded as being intrinsically table-top, the goal of a true table-top concept requires the development of both compact short-period undulators and miniature focusing devices. In a recent design study [8], our group pointed out the feasibility of the operation of a laser-plasma accelerator driven table-top FEL. Thus, the principle aim of this paper is to give experimental evidence that the crucial components that have to be used to control the propagation of the electron beam can be sufficiently miniaturized. We discuss the case of quadrupole lenses and undulators that represent the most fundamental optical elements, bridging the gap between conventional well-established accelerator technology and novel laser-plasma accelerators. A compact sample scenario is illustrated in Fig. 1. An energetic electron bunch is emitted from a near pointlike source with a divergence of a few mrad. A doublet of miniaturized high-gradient quadrupole magnets is used for the imaging of the source to the compact undulator only about one meter downstream. The image of the beam waist is considerably enlarged as a low divergence is required for the generation of narrow-band undulator radiation.

*Corresponding author.
u.schramm@fzd.de

FEL operation is usually based on a planar undulator [9]. Such an arrangement of alternating magnetic dipole fields forces the electron bunch on a sinusoidal trajectory. The bunch can thus couple with a copropagating radiation field. Because of the dispersion of the dipole fields, the induced energy modulation yields a current modulation, called microbunching. It expresses the fact that the electrons are grouped into small bunches separated by a fixed distance that resonantly coincides with the period length of the radiation field. Consequently, the radiation field can be amplified coherently. Lacking an initial resonant radiation field, a seed may also build up from spontaneous incoherent emission [10] in the SASE (self-amplification of spontaneous emission) process.

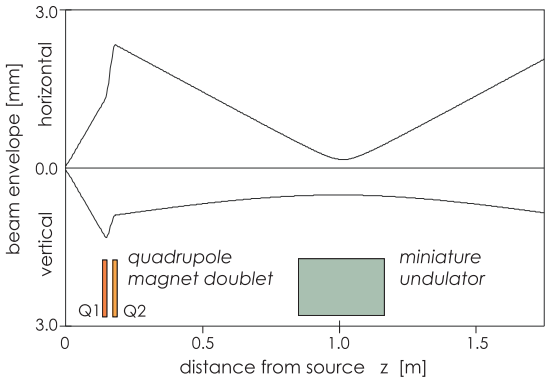

FIG. 1. (Color) Development of the horizontal (upper curve) and vertical (lower curve) beam envelopes of a 150 MeV laser-accelerated electron beam. The beam originates from a source of radius 1.3 μm ($z = 0$) at an exaggerated maximum divergence angle of 8 mrad. It enters a focusing quadrupole doublet (field gradient 500 T/m, individual lengths of the magnets $L_{Q1} = 17$ mm and $L_{Q2} = 15$ mm) and is focused into the miniature undulator ($L_u = 300$ mm).

 © 2007 The American Physical Society

Restrictive conditions have to be fulfilled for the amplification of radiation that, simply speaking, express the need for an overlap between the electron beam and the radiation field in all respects. The radiation bandwidth, and correspondingly the electron energy spread, has to be smaller ($\Delta\lambda_1/\lambda_1 = 2\Delta\gamma/\gamma < 2\rho$) than the so-called Pierce parameter ρ [10]. In large-scale FELs this parameter is typically of the order of 10^{-4}–10^{-3} while for laser-based FELs it can be 1 order of magnitude larger, especially due to the high peak currents [8]. Tolerances of the magnetic field distribution of the undulator are accordingly determined by the Pierce parameter, as will be discussed quantitatively later. A well-defined transport of the electron beam through the undulator has to ensure a divergence matched to the emission characteristics.

Besides the most demanding scenario of the table-top FEL [8] for which the components presented here have been developed, miniaturized lenses and undulators will have numerous applications in conventional as well as laser-driven accelerators. High gradient and thus short focal-length magnetic lenses have the potential for generating focal spots in the sub-micron range. These could be used as pointlike sources of hard radiation for phase contrast imaging with unprecedented transverse coherence [11], for compact Thomson scattering sources [12], or for the localized deposition of high radiation doses. Short focal-length lenses are further mandatory for the compact relay imaging of electron bunches between consecutive acceleration stages in cascaded laser-plasma acceleration schemes. Especially the postacceleration of dense bunches of electrons, first accelerated in the bubble regime [6,13], requires careful matching of the bunch density to the lower plasma density in a plasma wakefield accelerator. Such scenarios might help to increase the energy and improve the energy spread of bubble accelerated dense bunches and are thus of vital interest for table-top FEL projects.

In the following sections, detailed descriptions of the design of the miniaturized magnetic devices and their commissioning at the Mainz electron accelerator MAMI are given. In the last section, applications of undulators in radiation generation and diagnostics of laser-plasma accelerated beams are discussed.

II. HIGH FIELD MINIATURE UNDULATORS

The generation of hard undulator radiation of wavelength

$$\lambda_n = \frac{\lambda_u}{2\gamma^2 n}\left(1 + \frac{K^2}{2} + \gamma^2\theta^2\right) \tag{1}$$

with comparatively low electron energies γ relies on the reduction of the undulator period length λ_u from the usual cm scale to a mm scale, θ standing for the observation angle and n for the harmonic number of the emitted radiation. The performance of such an undulator largely depends on its deflection strength that is described by the normalized undulator parameter

$$K = \gamma\theta_e = \frac{e\lambda_u B_{y,0}}{2\pi m_e c} \approx 0.93\lambda_u[\mathrm{cm}]B_{y,0}[\mathrm{T}], \tag{2}$$

θ_e depicting the maximum electron deflection angle. For most undulator types, the amplitude of the magnetic field on axis $B_{y,0}$ can be maintained during miniaturization when the ratio of the gap height g to the period length λ_u, ideally being of the order of $g/\lambda_u \sim 0.3$, is preserved [9]. Thus, a reduction in λ_u implies an at least similar reduction in g and both will finally set limits to the miniaturization.

A. Design and manufacturing

For the construction of short period length undulators, different techniques have to be considered [9] starting with the well-established Halbach design [14]. In this pure permanent magnet (PPM) design, the field of the alternating magnet poles is closed by additional magnets rotated by 90°, similar to the case of the PPM quadrupoles, discussed in the next section. In contrast, the key of a hybrid design is to not only guide the field of permanent magnets from one period of the undulator to the next, but to concentrate and further increase the field in ferromagnetic plates that form the alternating poles of the undulator. This design is illustrated in Fig. 2 emphasizing the field concentration in the x-y pole plane. Typically, an increase of the peak field on axis $B_{y,0}$ by 20% can be achieved as compared to the PPM type. However, due to the nonlinearity of the approach, this value strongly depends on design details. Modern ferromagnetic materials such as tempered Co-Fe alloys (e.g., vacoflux 50 [15]) provide high saturation field strengths of the order of 2.3 T at room temperature, where the maximum remanent field of $Nd_2Fe_{14}B$ magnets reaches values of 1.2–1.4 T. The hybrid design allows for shorter periods as the ferromagnetic plates can be chosen thinner and ultimately, on the mm scale, manufactured thinner than sintered permanent magnet plates. In decreasing the period to the few-mm scale, however, further aspects have to be regarded. Magnet material with high coercivity has to be carefully chosen in order to withstand the magnetic shear forces, as irreversible demagnetization starts at moderate temperatures of ~60–80 °C.

As a compromise between the design goal of a miniature in-vacuum hybrid undulator of a short-period length of few mm, a gap of at least $g = 1.5$ mm, and a field of the order of $B_{y,0} = 1$ T, and, on the other hand, tolerable magnet stability and handling, a period length of $\lambda_u = 5$ mm has been chosen for the prototype presented here. The design (Fig. 2) was inspired by a similar design of two short 12 mm period precision undulators built in Mainz [16]. Its total length amounts to $N_u = 59.5$ periods or ~30 cm as depicted in the photograph in Fig. 3. Two half periods with approximately half the field strength at the ends [17]

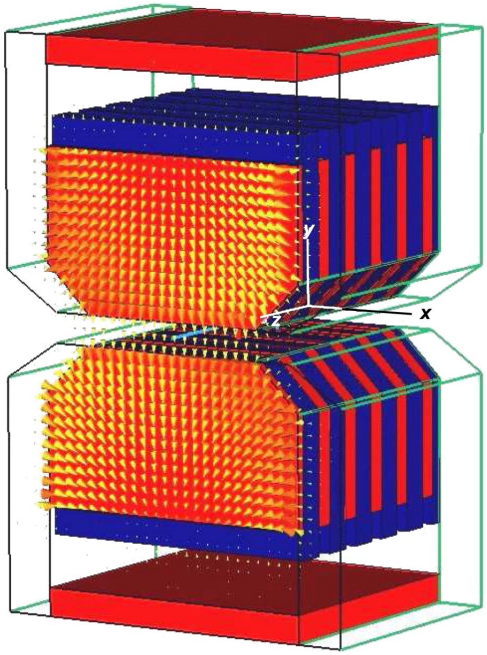

FIG. 2. (Color) Schematic view of the hybrid design of the miniature undulator, consisting of alternating plates of permanent magnets (blue), polarized parallel and antiparallel to the undulator axis z, and ferromagnetic material (red). In the front x-y plane arrows indicate the guiding of the magnetic field inside the ferromagnetic plates toward the undulator gap (simulation CST EM Studio). The transparent frames show the rail structure supporting the magnet blocks, also visible in the photograph in Fig. 3.

are added for a near deflection-free and straight transmission of an electron beam as discussed below.

Precision glued stacks of 1 mm thick Vacoflux 50 plates and 1.5 mm thick Vacodym 764 HR [15] magnets of 4 periods length form mounting units of the size of the order of a cm^3 as depicted in the inset of Fig. 3. Overall mechanical rigidity is guaranteed by nonmagnetic profiles anchored in the outer ferromagnetic yokes on either side of the magnet stacks (see Figs. 2 and 3). These profiles form a rail that holds the magnet stacks in place with a precision of the order of 10 μm. However, this precision on the percent level of the gap width implies deviations from the ideal field on axis $B_{y,0}$ on the same level. Thus, after the final assembly of the full system, the gap surface of the undulator was carefully finished by grinding.

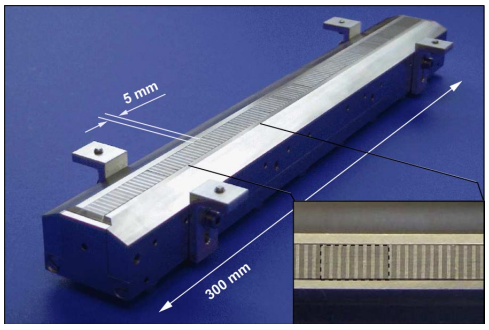

FIG. 3. (Color) Photograph of the lower half of the 60 period planar undulator after the first preliminary assembly. In the inset, the precision glued magnet stacks are visible (dashed box).

At the yoke side of the magnet stacks, the length of the magnets exceeds that of the ferromagnetic plates (see Fig. 4) in order to avoid a short-circuiting of the field between neighboring plates and thus provide the high tip field at the gap side of the poles of about 2 T. At the sides of the stacks in the y-z plane, this option could not be chosen to further increase the field as driving the plates further into saturation reduces the ability for an individual fine adjustment. This fine adjustment of the gap field can in principle be performed by a defined coupling of the individual plates to the yoke via ferromagnetic screws, similar to the technique applied for the tuning of the end plates, that is visible in Fig. 4.

The inset of Fig. 5 shows the distribution of the magnetic field perpendicular to the undulator plane $B_y(z)$ along the undulator axis z. It was measured after the grinding of the magnet surfaces by moving the undulator along a station-

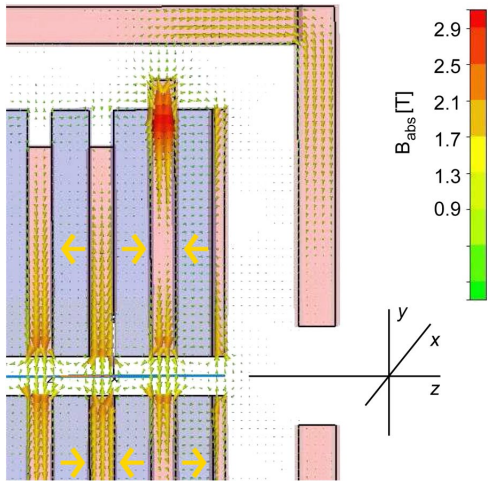

FIG. 4. (Color) False color arrows indicate the direction and strength of the magnetic B-field in the y-z plane of the hybrid undulator. The field at the pole tips amounts to ~2 T, the corresponding $B_{y,0}$ field on axis to ~0.9 T. In the simulation, the magnetization of the thin permanent magnets, indicated by yellow arrows, was set to 1.3 T. Slight tuning of the field on axis can be achieved by coupling the upper part of the ferromagnetic plates to the outer yoke structure, as displayed for the tuning of the end plates.

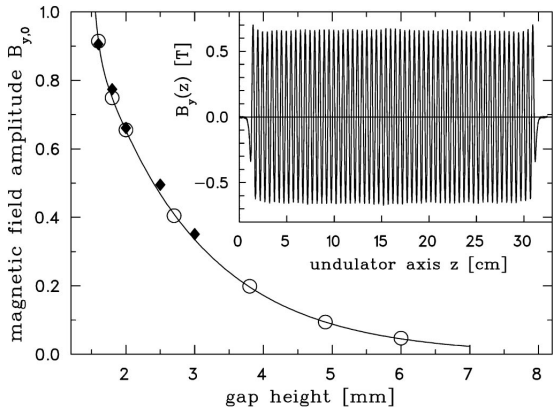

FIG. 5. Hall probe measurement of the magnetic field along the axis of the miniature undulator $B_y(z)$ for a gap height of 2 mm (inset). Measured peak values of the field $B_{y,0}$, corrected for the finite probe size of 0.75 mm diameter by 6% (rhombs), are compared to simulation results (CST EM Studio, open circles) as a function of the gap height g. The line shows a double exponential fit according to Ref. [9].

ary precision Hall probe with 0.75 mm head diameter. Field tuning was finally performed to a level of $\sigma(B_{y,0}) \sim 1\%$. First and second field integrals, representing the deflection strength and beam path, were cross-checked with the pulsed-wire method [18] during the tuning procedure. These measurements [19] exhibited a minor deflection of 400–800 MeV electron beams behind the undulator of few 10 μrad. In the experiments at the MAMI facility, described below, no beam deflection was visible on a screen some 10 m downstream, confirming the order of magnitude. Phase shake, defined as the deviation from the mean phase for one fixed point every half period [20], amounts to $\Delta\Psi_{\mathrm{rms}} = 2.2°$ and corresponds to a relative phase error of less than 1%.

In order to later investigate the effects of surface current induced wakefields on intense laser-accelerated electron bunches [8], the gap height of the prototype undulator can be varied over a wide range. Starting at the lowest value that allows for reasonable electron beam transmission of $g = 1.6$ mm ($g/\lambda_u = 0.32$), a peak field of $B_{y,0} = 0.91$ T was achieved. It exceeds that of typical cm-scale hybrid designs (of same g/λ_u) by a few percent [9] and corresponds to an undulator parameter of $K = 0.42$. With increasing g, the near exponential decrease of the peak field [9], depicted in Fig. 5, nicely corresponds to the design simulation and allows for a wide range of operation.

B. Performance tests

Present laser-driven accelerators still exhibit considerable pulse-to-pulse fluctuations in energy and directional pointing stability. Two complementary performance tests of the miniature undulator have therefore been pursued at the Mainz microtron facility MAMI [21]. Table I summarizes the corresponding beam parameters.

TABLE I. Undulator, electron beam (energy, unnormalized typical emittances, measured beam radii, and divergences at the position of the undulator), and radiation parameters for the two independent performance tests of the undulator at the Mainz microtron as described in the text.

K	0.32	0.45	0.45
E_e [MeV]	855	705	405
ε_x [10^{-9} m rad]	10	5	2
ε_y [10^{-9} m rad]	0.5	0.5	0.8
σ_x [μm]	510	370	236
σ_y [μm]	200	55	37
σ'_x [μrad]		53	
σ'_y [μrad]		3	
n	1, 2, 3, 4 (simultaneously)	1	3
E_n [keV]	1.32 ($n = 1$)	0.863	0.857

The aim of the first test experiment at MAMI was the simultaneous characterization of the spatial emission pattern of the undulator radiation for different harmonic numbers n. At an electron energy of 855 MeV ($\gamma = 1674$), an undulator parameter of $K \sim 0.32$ ($g \sim 2$ mm), and zero emission angle, a photon energy of the fundamental of $E_{n=1} \sim 1.32$ keV was expected. Radiation energy spectra could thus be directly observed with a cold Ge detector providing a 200 eV (FWHM) energy resolution in single photon counting mode. The detector was covered with an aperture of 250 μm radius and positioned 8.8 m downstream, so that an angular resolution of 30 μrad was achieved. This resolution was chosen to be of the order of the expected rms spread of the fundamental radiation ($n = 1$) of a perfect planar undulator,

$$\theta_{\mathrm{rms},x} \sim \frac{1}{2\gamma}\sqrt{\frac{1 + K^2/2}{nN_u}} \sim \frac{1}{2\gamma\sqrt{N_u}}, \tag{3}$$

giving $\theta_{\mathrm{rms},x} \sim 40$ μrad for $N_u = 60$. Electron beam transport was adjusted in order to provide a nearly collimated beam at the position of the undulator. Wire scan measurements at the entrance and exit of the undulator revealed rms widths of $\sigma_x = 0.5$ mm and $\sigma_y = 0.2$ mm. Thus, regarding a horizontal emittance of the order of 10^{-8} m rad, the contribution of the remaining electron beam divergence to the emission angle of the undulator radiation remains small for this experiment.

Figure 6 shows the measured energy spectra of the undulator radiation as a function of the horizontal and vertical emission angles, where the general angular shape is described by Eq. (1) (solid red lines in the density plots). On axis ($\theta = 0$, upper left figure), the total yield is compared to simulations (red line) using the single particle

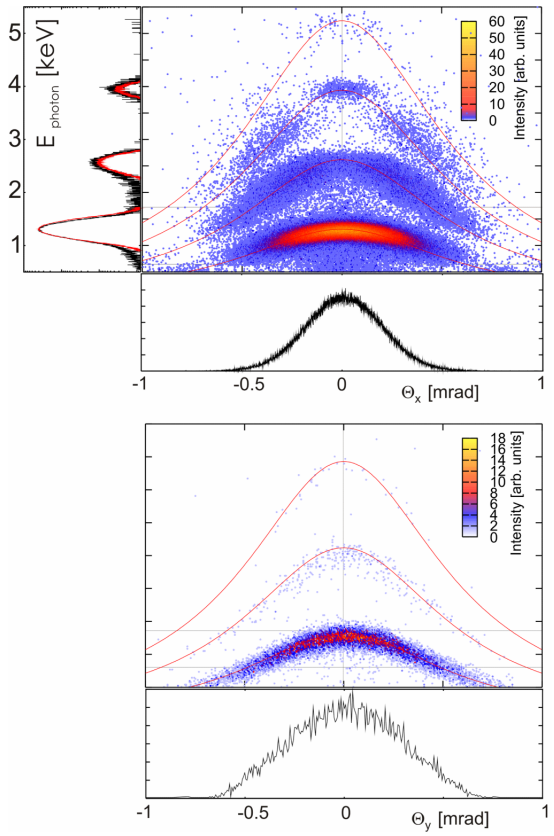

FIG. 6. (Color) Undulator radiation spectra as a function of the horizontal (x) and the vertical (y) observation angles θ, recorded with a Ge detector at an electron energy of 855 MeV at MAMI. The absolute on-axis yield for harmonics up to the third is compared to SPECTRA simulations [22] in the left graph (red line) including an energy resolution of 200 eV (FWHM). The angular spread, integrated between the thin horizontal lines, is depicted in the lower one. Solid (red) lines indicate the general $\gamma^2\theta^2$ dependence of the energy.

code SPECTRA [22], including aperture and energy resolution of the detector. Good agreement is achieved, especially in the amplitude ratio between different harmonics, while details of the spectrum are blurred due to detector resolution.

The second experiment aimed for the precise measurement of the energy spectrum. More stringently than the previous measurement, it provides information on the number of undulator periods for which the undulator radiation adds up coherently and thus on the quality of the beam path inside the undulator.

For the case of an ideal undulator, the radiation is emitted within the box-shaped time window corresponding to the passage of an electron through the alternating field. Thus, the on-axis energy spectrum is described by its Fourier-transform

$$I_n(E) \propto \sin^2\left(\pi n N_u \frac{E_n - E}{E_n}\right) \Big/ \left(\pi n N_u \frac{E_n - E}{E_n}\right)^2 \qquad (4)$$

and the relative bandwidth (FWHM) of the different harmonics can be approximated by

$$\frac{\Delta E_n}{E_n} \sim \frac{2 \times 1.4}{\pi n N_u} \sim \frac{1}{n N_u}. \qquad (5)$$

For this experiment, a high-resolution grating spectrometer with variable line spacing was installed instead of the Ge detector. It was read out by an efficient x-ray CCD camera (pixel size 13×13 μm^2) some 6.7 m further downstream [11,23]. Succeeding the first experiment, the undulator was carefully retuned to the most critical minimum gap height of $g \sim 1.5$ mm ($K = 0.45$). Pulsed-wire measurements indicated a straight electron trajectory in the sense that deviations from the mean path are small compared to the deflection amplitude of the undulating beam over at least the inner 90% of the path [19]. The electron beam energy was set to 705 and 405 MeV as these energies lead to a radiation energy of $E_n \sim 860$ eV for the fundamental and the third harmonic, respectively. This photon energy coincides with two L-absorption edges of a thin Ni foil ($E_{L2} = 854.7$ eV, $E_{L3} = 871.9$ eV [23]) providing the required high-resolution online calibration of the linewidth of the undulator radiation. Electron beam focusing was optimized for a minimum linewidth taking into account beam divergence as well as the analytical off-axis field distribution of an undulator.

Figure 7 depicts energy spectra of the undulator radiation on axis ($\theta = 0$) for the fundamental and for the third harmonic, that are extracted from images resolving the horizontal angular distribution [19]. The measured relative

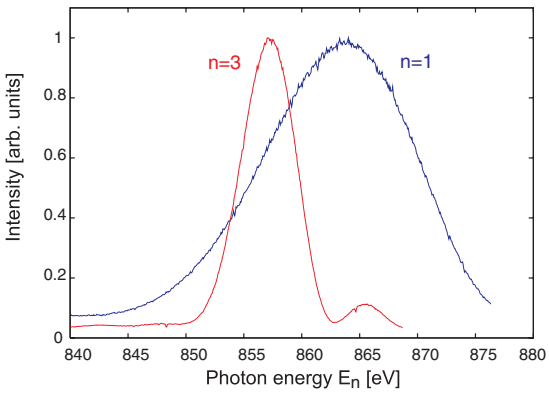

FIG. 7. (Color) On-axis high-resolution energy spectra of the fundamental ($n = 1$) and the more narrow third harmonic ($n = 3$) undulator radiation for an electron energy of 705 and 405 MeV, respectively.

width (FWHM) of the spectra of $\Delta E_1/E_1 = 0.0174$ and $\Delta E_3/E_3 = 0.0063$, respectively, translates into an effective number of undulator periods of $N_{u,\mathrm{eff}} \sim 53$–$58$, when the approximate Eq. (5) is applied. A further consideration of the measured field and phase fluctuations consistently reveals the participation of the full undulator ($N_{u,\mathrm{eff}} \sim 60$) in the generation of the radiation and thus confirms its design performance.

III. COMPACT HIGH-GRADIENT QUADRUPOLE MAGNETS

Beam transport and especially imaging from the compact laser-plasma accelerator to the miniature undulator has to be provided by compact devices with short focal length. The construction of such compact quadrupole magnets with high field gradients relies on well-established principles. On the one hand, the absolute field on the magnet poles $B(r_i)$ has to be maximized while, on the other, the bore radius r_i has to be minimized. A reasonable compromise can be achieved for $r_i = 3$ mm and $B(r_i) \sim 1.5$ T leading to a gradient of the order of 500 T/m [12]. Here, a simple and economical design has been chosen, where the quadrupole field is defined by four radially magnetized wedges of $Nd_2Fe_{14}B$ magnets [15]. The outer field closure is accomplished by four additional pairs of permanent magnets as sketched in Fig. 8. As the four main wedges are strongly attracted toward the center of the quadrupole, mechanical precision and thus field accuracy can be achieved by the insertion of a nonmagnetic precision cylinder into the center of the quadrupole, as visible in the photograph in Fig. 9. Three-dimensional field simulations (CST EM Studio) as well as electron tracking simulations revealed a sufficient optical quality of this simple

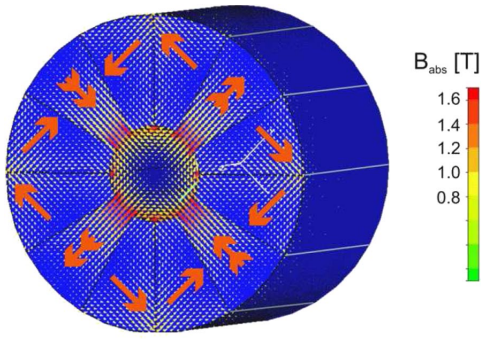

FIG. 8. (Color) Schematic view of the 12 segment Halbach design of one quadrupole magnet. While 4 radially magnetized segments define the quadrupole field, 8 are used for the outer field closure, thick arrows indicating the direction of magnetization. False color arrows illustrate the simulated strength and direction of the resulting quadrupole field inside a bore of radius $r_i = 3$ mm. The tip field strength amounts to $B(r_i) \sim 1.5$ T.

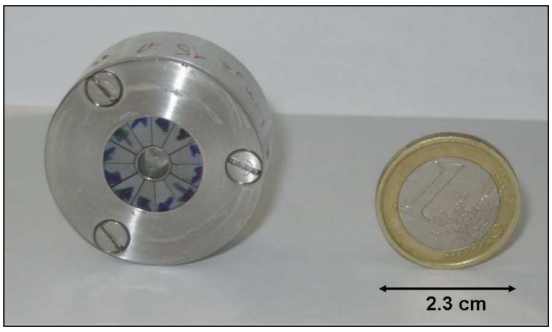

FIG. 9. (Color) Photograph of one mounted miniature quadrupole magnet.

design, comparable to the more complex one recently realized by the PLEIADES group [12].

The field gradient has been verified by systematic measurements of the absolute field as a function of the distance from the quadrupole center. As for the case of the undulator, a precision Hall probe with a head of 0.75 mm diameter was used. Ideally, the probe size should not affect the measurement. Figure 10 expresses not only the good agreement between the design simulations and the measurement, but also the integrity of the quadrupole field over almost the whole aperture of the quadrupole. Ten different quadrupole magnets were analyzed, leading to an average field gradient of (503 ± 6) T/m.

In order to further investigate potential effects of deviations from an ideal quadrupole field, single quadrupoles as well as doublets were tested at the Mainz microtron facility MAMI. An electron energy of 600 MeV was chosen, where the unnormalized rms emittance of the beam amounts to $\varepsilon_y = 0.5 \times 10^{-9}$ m rad and the relative energy spread to

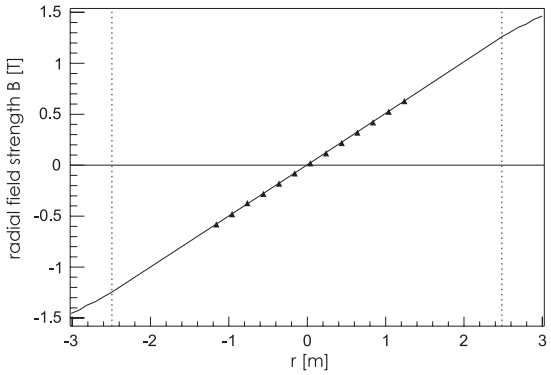

FIG. 10. Hall probe measurements (triangles) are plotted against the distance from the center of the quadrupole and compared to the design simulation (solid line). The dashed lines indicate aperture limitations originating from the central nonmagnetic cylinder. The field gradient amounts to 503 T/m.

10^{-5}. The incoming beam was nearly collimated for an illumination of a large fraction of the lens. Beam radii were again measured by scanning tungsten wires of 4 and 10 μm diameter through the low current electron beam. In Fig. 11 the beta function of the electron beam $\beta_y(z) = \sigma_y^2(z)/\varepsilon_y$, derived from the measured envelope radius σ_y, is depicted around the focus ~15 cm behind the quadrupole magnet. For simplicity only one quadrupole was used, and therefore the vertical degree of freedom was focused to a line focus. From the parabolic shape around the focal point (introducing the relative position coordinate s), the beta function at the focal point β_y^*

$$\beta_y(s) = \beta_y^* + \frac{s^2}{\beta_y^*} \tag{6}$$

can be estimated to $\beta_y^* \sim 1.2$ mm, yielding a width of the focal line of the order of below one micron.

The value of the beta function turns out to be in good overall agreement with the Hall probe measurements, the measured beam size in front of the quadrupole magnet and the remaining beam divergence. We therefore conclude that the imaging properties of this simple lens are sufficient for both the laser-plasma applications as well as for the future generation of a two-dimensional sub-micron focal spot at MAMI.

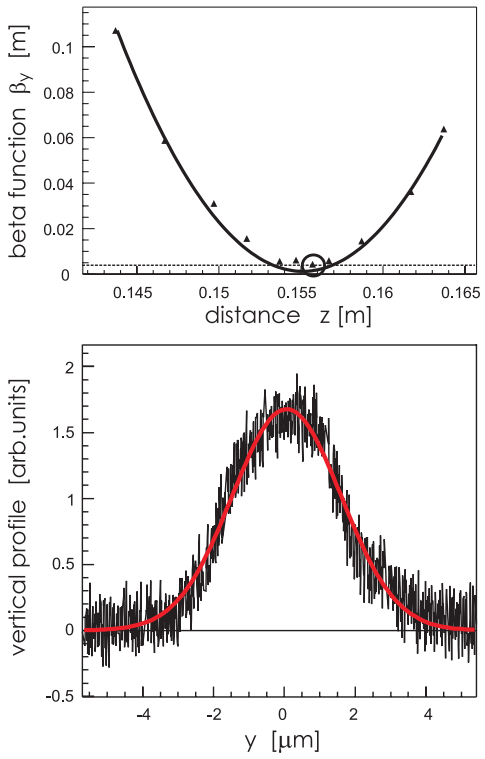

FIG. 11. (Color) Results of the measurement of the imaging properties of a single quadrupole magnet. The triangles in the upper graph depict the measured beta function. The horizontal line indicates the resolution of a single measurement due to the thickness of the wire of 4 μm. The lower graph illustrates the resolution limited width measured close to the focal point.

IV. STATUS AND PERSPECTIVES

Having demonstrated the performance of the miniaturized magnetic devices, the following section focuses on applications with laser-plasma accelerated electron beams, constraints that might arise due to the high peak currents, and technological perspectives for even better performance at similar dimensions.

One first application of miniature undulators will be their use as a diagnostic tool for laser-accelerated electron beams. For laser-plasma accelerator laboratories compact electron spectrometers, that do not rely on magnetic dispersion, are highly valuable. Usually, space is too restricted for the installation of dipole magnets with bending radii of the order of 10 m for the detection of electrons of GeV energies. A well characterized diagnostic undulator, however, could be used for measuring electron energy and energy spread as well as the beam divergence. Laser-accelerated electron beams typically exhibit broad spectra of the order of 1%–10%. Thus, an intrinsic line width $1/(nN_u)$ of <1% is sufficient to determine the energy spread with unprecedented accuracy. Beam alignment errors and divergence have to be kept small so that according to Eq. (1) only the variation in γ effects the observed wavelength λ_1. On the other hand, the electron beam divergence can be measured provided the divergence of the undulator light $1/(2\gamma\sqrt{nN_u})$ is significantly smaller. Both conditions imply that a diagnostic undulator must have a period number of at least $N_u \sim 100$.

Regarding the potential for high peak currents of $I \sim$ 100 kA [6] in laser-plasma acceleration for energies of presently up to ~GeV, miniature undulators should be used in laser-driven FELs in order to reach the regime of extreme UV and soft x-ray radiation. Such a regime [8] leads to comparatively large Pierce parameters ρ and hence higher tolerance of the FEL process against disturbing effects, such as initial energy spread and emittance, but also wakefield-induced energy spreads [24]. Further, for medical applications, where photons of at least 20 keV are required, quantum fluctuations in the spontaneous emission [25] cause additional energy spread which hinders the FEL process. Since their impact increases with γ as $d\langle\Delta\gamma^2\rangle/dz \propto \gamma^4$, electron energies should remain below 10 GeV. Note that, for the generation of 50 keV photons, 7 GeV electrons and an undulator period of 7 mm are sufficient.

A short undulator period must thus be compensated by peak currents I that exceed those used in large-scale FEL facilities. On the one hand, a large Pierce parameter re-

duces the saturation length of the FEL. On the other, the saturation power of the FEL $P_{\mathrm{sat}} \propto \rho P_{\mathrm{beam}}$ roughly scales as $P_{\mathrm{sat}} \propto (I\lambda_u)^{4/3}$ [8]. However, the shorter the undulator period is, the smaller the corresponding gap height becomes and thus, the stronger the induced wakefields. This effect constitutes a fundamental limit to the undulator period besides the technological obstacles.

The undulator presented in this paper was found to have a mean field inhomogeneity of about 1%. Since the undulator parameter $K = 0.4$ remains below unity, the effective increase of the undulator radiation wavelength $\Delta\lambda_1/\lambda_1$ is smaller by a factor of $K^2\Delta K/K$, hence $\Delta\lambda_1/\lambda_1 = 1.6 \times 10^{-3}$. Since the Pierce parameter amounts to about 0.01 for the proof-of-principle FEL suggested in Ref. [8], the present field errors appear tolerable. Although the present undulator is about a factor of 3 too short for reaching saturation of the SASE process, amplification should become visible [8,26]. The undulator radiation spectra measured at MAMI exhibit a well-reproducible ratio of the intensity of the fundamental and the third harmonic in the case of spontaneous emission. For the detection of SASE signatures this ratio is important, because a change in favor of the fundamental constitutes a hint for amplification.

Regarding the high peak currents, resistive wall and geometric wakefields seem likely to represent the main degradation effect for table-top FELs. The most obvious countermeasure will be an increase of the undulator gap size as the strength of the wakefields scales as one over the square of the gap size. However, merely increasing the gap would lower the peak magnetic field strength on axis and thus the K parameter. The intensity of spontaneous undulator radiation scales with K^2 and, furthermore, a decrease in K leads to an increase in the FEL saturation length. Thus, an increase of the gap size can only be accepted when novel techniques are developed that maintain the field strength on axis.

Future progress in the increase of the peak field of miniature undulators by about 30% could be made by cooling the permanent magnets to near liquid nitrogen temperatures. It has been suggested that for hybrid types the saturation field strength in the ferromagnetic pole material can be increased by simultaneously replacing the Co steel by dedicated materials such as dysprosium [27]. Superconducting technology on the other hand has not yet reached mm-scale period length with the desired field strength. The smallest prototype of the Karlsruhe group ($\lambda_u = 3.8$ mm) based on NbTi wires reached peak fields of around 1 T for a gap of 1 mm [28]. Recent results achieved [29] with an in-vacuum, $\lambda_u = 14$ mm, and $g/\lambda_u = 0.6$ undulator indicate an improvement of about 20% compared to conservative hybrid designs and no improvement over the one presented here. However, there is room for future coil development based on Nb_3Sn that might allow for comparative K-values and the desired increase in the gap height [30] by a factor of about 1.5.

Briefly summarizing, we presented results on the successful commissioning of miniaturized lenses and undulators dedicated for the use in the field of laser-plasma accelerators. First experiments on beam diagnostics in this field are presently on the way and further undulator development as mentioned above is planned.

ACKNOWLEDGMENTS

This work has been funded by DFG through TRANSREGIO TR18 and supported by the DFG cluster-of-excellence Munich Center for Advanced Photonics MAP.

[1] S. P. D. Mangles, C. Murphy, Z. Najmudin, A. Thomas, J. Collier, A. Dangor, E. Divall, P. Foster, J. Gallacher, C. Hooker, D. Jaroszynski, A. Langley, W. Mori, P. Norreys, F. Tsung, R. Viskup, B. Walton, and K. Krushelnick, Nature (London) **431**, 535 (2004).

[2] C. G. R. Geddes, C. Toth, J. van Tilborg, E. Esarey, C. Schroeder, D. Bruhwiller, C. Nieter, J. Cary, and W. Leemans, Nature (London) **431**, 538 (2004).

[3] J. Faure, Y. Glinec, A. Pukhov, S. Kiselev, S. Gordienko, E. Lefebvre, J.-P. Rousseau, F. Burgy, and V. Malka, Nature (London) **431**, 541 (2004).

[4] W. P. Leemans, B. Nagler, A. Gonsalves, C. Toth, K. Nakamura, C. Geddes, E. Esarey, C. Schroeder, and S. Hooker, Nature Phys. **2**, 696 (2006).

[5] J. Faure, C. Rechatin, A. Norlin, A. Lifschitz, Y. Glinec, and V. Malka, Nature (London) **444**, 737 (2006).

[6] M. Geissler, J. Schreiber, and J. Meyer-ter-Vehn, New J. Phys. **8**, 186 (2006).

[7] A. Rousse, K. T. Phuoc, R. Shah, A. Pukhov, E. Lefebvre, V. Malka, S. Kiselev, F. Burgy, J.-P. Rousseau, D. Umstadter, and D. Hulin, Phys. Rev. Lett. **93**, 135005 (2004).

[8] F. Grüner, S. Becker, U. Schramm, T. Eichner, M. Fuchs, R. Weingartner, D. Habs, J. Meyer-ter-Vehn, M. Geissler, M. Ferrario, L. Serafini, B. an der Geer, H. Backe, W. Lauth, and S. Reiche, Appl. Phys. B **86**, 431 (2007).

[9] P. Elleaume, J. Chavanne, and B. Faatz, Nucl. Instrum. Methods Phys. Res., Sect. A **455**, 503 (2000).

[10] R. Bonifacio, C. Pellegrini, and L. M. Narduci, Opt. Commun. **50**, 373 (1984).

[11] M. El-Ghazaky, H. Backe, W. Lauth, G. Kube, P. Kunz, A. Sharafutdinov, and T. Weber, Eur. Phys. J. A **28**, 197 (2006).

[12] J. K. Lim, P. Frigola, G. Travish, J. B. Rosenzweig, S. G. Anderson, W. J. Brown, J. S. Jacob, C. L. Robbins, and A. M. Tremaine, Phys. Rev. ST Accel. Beams **8**, 072401 (2005).

[13] J. Meyer-ter-Vehn and A. Pukhov, Appl. Phys. B **74**, 355 (2002).

[14] K. Halbach, Nucl. Instrum. Methods **187**, 109 (1981).

[15] Vacuumschmelze Hanau, Vacoflux 50, and Vacodym 764 HR data sheets, 2005, http://www.vacuumschmelze.com.

[16] S. Dambach, H. Backe, Th. Doerk, N. Eftekhari, H. Euteneuer, F. Görgen, F. Hagenbuck, K. H. Kaiser,

O. Kettig, G. Kube, W. Lauth, H. Schöpe, A. Steinhof, Th. Tonn, and Th. Walcher, Phys. Rev. Lett. **80**, 5473 (1998); S. Dambach, Ph.D. thesis, Universität Mainz, 1998.
[17] I. Vassermann and E. R. Moog, Rev. Sci. Instrum. **66**, 1943 (1995).
[18] R. W. Warren, Nucl. Instrum. Methods Phys. Res., Sect. A **272**, 257 (1988).
[19] T. Eichner, Diploma thesis, LMU Munich, 2007.
[20] R. P. Walker, Nucl. Instrum. Methods Phys. Res., Sect. A **335**, 328 (1993).
[21] http://www.kph.uni-mainz.de/B1/floorplan.php.
[22] T. Tanaka and H. Kitamura, J. Synchrotron Radiat. **8**, 1221 (2001).
[23] W. Lauth, H. Backe, O. Kettig, P. Kunz, A. Sharafutdinov, and T. Weber, Eur. Phys. J. A **28**, 185 (2006).
[24] A. W. Chao, *Physics of Collective Beam Instabilities in High Energy Accelerators* (John Wiley & Sons, New York, 1993); K. Bane, SLAC-PUB-11829, 2006.
[25] M. Sands, Phys. Rev. **97**, 470 (1955).
[26] S. Reiche, Nucl. Instrum. Methods Phys. Res., Sect. A **429**, 243 (1999).
[27] T. Hara, T. Tanaka, H. Kitamura, T. Bizen, X. Marechal, T. Seike, T. Kohda, and Y. Matsuura, Phys. Rev. ST Accel. Beams **7**, 050702 (2004).
[28] T. Hezel, B. Krevet, H. O. Moser, J. A. Rossmanith, R. Rossmanith, and T. Schneider, J. Synchrotron Radiat. **5**, 448 (1998).
[29] S. Casalbuoni, M. Hagelstein, B. Kostka, R. Rossmanith, M. Weisser, E. Steffens, A. Bernhard, D. Wollmann, and T. Baumbach, Phys. Rev. ST Accel. Beams **9**, 010702 (2006).
[30] R. Rossmanith (private communication).

Chapter V

Table-Top Free-Electron Laser

Title of Publication:

Design considerations for table-top, laser-based VUV and X-ray free electron lasers

The additional references [121]-[135] are included in this publication.

Appl. Phys. B 86, 431–435 (2007)
DOI: 10.1007/s00340-006-2565-7

Applied Physics B
Lasers and Optics

Rapid communication

Design considerations for table-top, laser-based VUV and X-ray free electron lasers

F. GRÜNER[1,✉]
S. BECKER[1]
U. SCHRAMM[1]
T. EICHNER[1]
M. FUCHS[1]
R. WEINGARTNER[1]
D. HABS[1]
J. MEYER-TER-VEHN[2]
M. GEISSLER[2]
M. FERRARIO[3]
L. SERAFINI[3]
B. VAN DER GEER[4]
H. BACKE[5]
W. LAUTH[5]
S. REICHE[6]

[1] Department of Physics, Ludwig-Maximilians-Universität München, 85748 Garching, Germany
[2] Max-Planck Institute of Quantum Optics, 85748 Garching, Germany
[3] INFN, 00044 Frascati, Italy
[4] Pulsar Physics, 3762 Soest, Netherlands
[5] Institute of Nuclear Physics, Mainz, Germany
[6] University of California Los Angeles, UCLA, Los Angeles, CA, USA

Received: 12 December 2006
Published online: 27 January 2007 • **© Springer-Verlag 2007**

ABSTRACT A recent breakthrough in laser-plasma accelerators, based upon ultrashort high-intensity lasers, demonstrated the generation of quasi-monoenergetic GeV-electrons. With future Petawatt lasers ultra-high beam currents of ~ 100 kA in ~ 10 fs can be expected, allowing for drastic reduction in the undulator length of free-electron-lasers (FELs). We present a discussion of the key aspects of a table-top FEL design, including energy loss and chirps induced by space-charge and wakefields. These effects become important for an optimized table-top FEL operation. A first proof-of-principle VUV case is considered as well as a table-top X-ray-FEL which may also open a brilliant light source for new methods in clinical diagnostics.

PACS 41.60.Cr; 52.38.Kd

1 Introduction

The pursuit of table-top FELs combines two rapidly developing fields: laser-plasma accelerators, where the generation of intense quasi-monoenergetic electron bunches up to the GeV range has been achieved [1–4], and large-scale X-ray free-electron lasers (XFELs) that are expected to deliver photon beams with unprecedented peak brilliance. A prominent application of such FEL pulses is single molecule imaging [5]. The proposed laser-plasma accelerator-based FELs would not only allow a greater availability due to their smaller size and costs, but also offer new features, such as pulses synchronized to the phase-controlled few-cycle driver laser [6] for pump–probe experiments. Moreover, the X-ray energy of a table-top XFEL can be as large as required for medical diagnostics (above 20 keV [7]).

The mechanism for the generation of intense (nC charge) quasi-monoenergetic electron pulses by laser-plasma accelerators requires an ultrashort, high-intensity laser-pulse with a length shorter than the plasma wavelength (on the μm-scale corresponding to gas densities of $10^{19}\,\mathrm{cm}^{-3}$). Due to the ponderomotive force, plasma electrons are blown out transversely, leaving an electron-free zone – the bubble – behind the laser pulse [8]. These electrons return to the axis after half a plasma oscillation, thus determining the size of the bubble in the order of the plasma wavelength. Typically about $10^9 \ldots 10^{10}$ electrons are captured into the bubble, as found both experimentally and from scaling laws of relevant bubble parameters within the framework of similarity arguments [9]. Due to the inertial positive ion background, these electrons experience a strong electrical field gradient of up to TV/m. Particle-in-cell (PIC) simulations [10] show that the bubble electrons form a stem that is geometrically considerably smaller than the bubble as seen in Fig. 1.

For these dimensions, beam currents of the order of ~ 100 kA (i.e. ~ 1 nC charge within ~ 10 fs) can be reached without the need for any bunch compressor. For preparation of the required gas densities, either supersonic gas-jets or capillaries [11] are used, the latter consisting of a ~ 300 μm-thin gas-filled channel with a parabolic radial ion density profile generated by a second laser pulse or discharge. The advantage of the capillary is that the laser can be guided beyond the Rayleigh length allowing longer acceleration distances and hence higher electron energies. The very recent experiments by Leemans et al. [4], utilizing a 40-TW laser pulse of 38 fs duration and a gas density of $4.3 \times 10^{18}\,\mathrm{cm}^{-3}$, clearly show that 1 GeV electron beams can now be produced with capillaries. However, the measured charge of 30 pC is significantly below our design goal of 1 nC. In order to further improve the resulting current, we propose the scheme described below. The number of bubble electrons can be increased when using plasmas with higher density such as in Fig. 1, because the feeding process is more efficient if more plasma electrons are present. An increased gas density requires shorter laser-pulses (sub-10-fs), such that the entire laser pulse fits into one plasma period. In this case, the entire laser pulse energy can be used,

✉ Fax: +49 89 2891 4072, E-mail: florian.gruener@physik.uni-muenchen.de

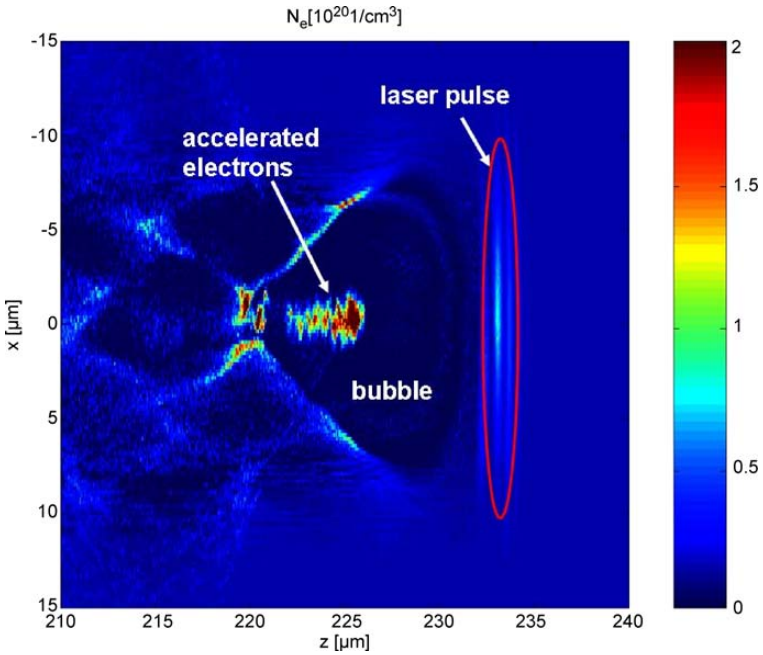

FIGURE 1 (Color online) Snapshot of electron density (in units of 10^{20} cm^{-3}) from PIC simulation. The geometrical size of the electron-free cavity ("bubble") behind the laser spot corresponds to the plasma period, which is about 8 µm in this case (gas density 1.8×10^{19} cm^{-3}). The stem of the high-energy electrons is much shorter than the plasma period

while longer pulses lose energy during self-shortening for entering the bubble regime. Therefore, in contrast to all previous laser-acceleration experiments, we propose to use a different driver laser, namely a ~ 5 fs-Petawatt laser (like the Petawatt-field-synthesizer PFS at MPQ [12]). Own PIC simulations show that such ultrashort lasers can capture more than 1 nC charge inside the bubble. The smaller plasma period leads to smaller bubbles, hence shorter bubble stems and thus higher currents (1 nC in 10 fs). However, the expected final energy in the bubble regime is, according to the scaling laws, lower for shorter laser pulses. To overcome this limit, we also propose to use a capillary and suggest the following scenario therein: with a longitudinal plasma density gradient, the laser pulse can be forced to gradually increase its diameter, thus adiabatically turning from the pure bubble regime into the pure blow-out regime long before the laser is depleted. Figure 1 shows a snapshot of a bubble around the transition from the bubble to the blow-out regime, where the electrons blown away from the laser and flowing around the bubble are so strongly deflected by the electric field of the captured bubble electrons, that electrons are no longer scattered into the bubble (which is not charge-neutralized yet). The number and absolute energy spread of the bubble electrons is thus frozen, but their energy is still increased due to the present bubble fields. The remaining energy of the laser allows maintaining of the bubble structure for the remaining distance inside the capillary, where the laser is then guided along to overcome the Rayleigh limit. It is only for this stage with increased laser beam size, that the capillary-induced guiding is relevant. Note that this scheme is a two-stage approach, but within one and the same capillary, where the laser turns adiabatically from one stage into the other. It can be expected that the energy spread for 100 MeV is about 1% (as confirmed by measurements [2]), but 0.1% for 1 GeV[1]. Normalized emittances are found both from simulations and experiments to range between 0.1–1 mm mrad.

[1] Note that the detector resolution in the cited GeV-experiment did not suffice to resolve energy spreads below one percent.

2 Table-top free-electron-lasers

An FEL requires an undulator which is an arrangement of magnets with an alternating transverse magnetic field. Electrons in an undulator are forced on a sinusoidal trajectory and can thus couple with a co-propagating radiation field. The induced energy modulation yields a current modulation from the dispersion of the undulator field. This modulation is called micro-bunching expressing the fact that the electrons are grouped into small bunches separated by a fixed distance. Therefore, electrons emit coherent radiation with a wavelength equal to the periodic length between the micro-bunches. In a self-amplification of spontaneous emission (SASE) FEL, there is no initial radiation field and the seed has to be built up by the spontaneous (incoherent) emission [13]. We present quantitative arguments, which are complemented by SASE FEL (GENESIS 1.3 [14]) simulations. The gain length, which is the e-folding length of the exponential amplification of the radiation power, is

$$L_{\mathrm{gain,ideal}} = \frac{\lambda_\mathrm{u}}{4\pi\sqrt{3}\varrho}\,, \tag{1}$$

with undulator period λ_u and the basic scaling parameter ϱ. This Pierce or FEL parameter describes the conversion efficiency from the electron beam power into the FEL radiation power and reads for the one-dimensional and ideal case (neglecting energy spread, emittance, diffraction, and time-dependence) [13, 15]

$$\varrho = \frac{1}{2\gamma}\left[\frac{I}{I_\mathrm{A}}\left(\frac{\lambda_\mathrm{u} A_\mathrm{u}}{2\pi\sigma_x}\right)^2\right]^{1/3}. \tag{2}$$

Here $\gamma = E_\mathrm{beam}/mc^2$ is the electron beam energy, I the beam current, $I_\mathrm{A} = 17$ kA the Alfven-current, σ_x the beam size and $A_\mathrm{u} = a_\mathrm{u}[J_0(\zeta) - J_1(\zeta)]$ (planar undulator), whereby $a_\mathrm{u}^2 = K^2/2$, K is the undulator parameter ($K = 0.93\lambda_\mathrm{u}[\mathrm{cm}]B_0[T]$ and B_0 the magnetic field strength on the undulator axis), $\zeta = a_\mathrm{u}^2/(2(1+a_\mathrm{u}^2))$, and J are Bessel functions. In the presence of energy spread, emittance, and diffraction, a correction factor Λ is introduced for the gain length [15]: $L_\mathrm{gain} = L_\mathrm{gain,ideal}(1+$

Λ). The saturation length $L_{\rm sat}$ is the length along the undulator at which maximum micro-bunching is reached. The power of the FEL radiation at this point is the saturation power $P_{\rm sat}$, while the shot noise power $P_{\rm n}$ is the power of the spontaneous undulator radiation from which the SASE FEL starts. The coupling factor $\alpha = 1/9$ describes the efficiency at which the noise power couples to the FEL gain process. The saturation length reads

$$L_{\rm sat} = L_{\rm gain} \ln\left(\frac{P_{\rm sat}}{\alpha P_{\rm n}}\right) , \qquad (3)$$

where the saturation power scales as

$$P_{\rm sat} \sim \left(\frac{1}{1+\Lambda}\right)^2 (I\lambda_{\rm u})^{4/3} . \qquad (4)$$

The FEL-wavelength is, in case of a planar undulator,

$$\lambda = \frac{\lambda_{\rm u}}{2\gamma^2}\left[1+\frac{K^2}{2}\right]. \qquad (5)$$

Thus, for reaching a certain wavelength λ, a shorter undulator period $\lambda_{\rm u}$ allows the use of less energetic electrons. In the following Table 1 and Fig. 2, we compare the FLASH VUV FEL (DESY) in the so-called femtosecond mode [16] with our corresponding table-top VUV FEL as well as a table-top XFEL operating with 1.2 GeV electrons, as discussed below.

The importance of the ultra-high current in the table-top case is evident. The smaller undulator period allows a smaller beam energy, hence decreasing the gain and saturation lengths. The Pierce parameter gives the upper limit of the acceptable energy spread σ_γ/γ. Thus, for compensating the relatively large energy spread of laser-plasma accelerators and for maintaining a large output power, a beam current significantly above ~ 17 kA is mandatory for keeping ϱ large and Λ small.

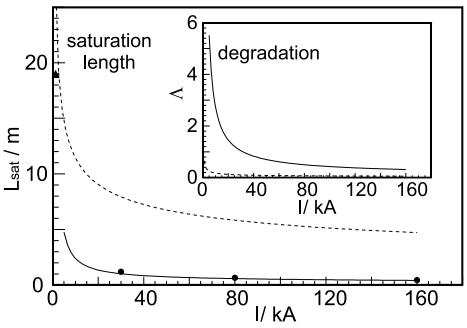

FIGURE 2 Saturation lengths (3) and (*inset*) degradation factor Λ as a function of electron beam current I: DESY's FLASH (*dashed curve*, *triangle*) and the table-top VUV scenario (*solid line*). The circles denote specific GENESIS runs

2.1 *Space charge effects*

Such ultra-high beam currents are subject to strong space-charge forces. After release into vacuum, the electron bunch starts expanding, for which there are two sources: (i) its own space-charge, driving a Coulomb-explosion, i.e. (transverse) space-charge expansion and (longitudinal) debunching, and (ii) its initial divergence, which drives a linear transverse expansion. Such expansions transform potential energy into kinetic, hence changing the initial energy distribution and bunch form. First, we want to discuss an extreme case, that is, an upper limit of the charge that can be expected from a laser-plasma accelerator at lower energies. For this study we take a beam energy of $\gamma_0 = 260$, 1.25 nC charge, and a Gaussian bunch with sizes $\sigma_{x,y,z} = 1\,\mu$m, corresponding to $I = 150$ kA, and an initial divergence of $\theta_0 = 1$ mrad. In the rest frame of the bunch, its length amounts to $\sigma_z' = \sigma_z\gamma_0 = 260\,\mu$m. For such an aspect-ratio, the transverse Coulomb-explosion dominates over the longitudinal one (GPT [17] simulations reveal that after a time period of 1 ps $\sigma_x' = 73\,\mu$m, while $\sigma_z' = 268\,\mu$m). Figure 3 shows the electron distribution in the bunch rest frame from the GPT simulations.

It can be seen that the transverse Coulomb explosion dominates the longitudinal one. We want to emphasize here that studies of space-charge effects of such ultra-dense relativistic bunches can be simulated most accurately only with codes (such as GPT and CSRtrack [18]) which utilize point-to-point interactions (a result also found in [19]). In contrast, other codes merely based upon Poisson-solvers cannot cope with large relative particle motions within the bunch rest frame in case of large initial energy spreads and Coulomb explosion-induced motion. In comparison with the Coulomb-driven explosion, the linear divergence-driven transverse expansion is even larger: after a distance of 1 cm in the laboratory frame, the beam size is increased to 10 μm, while the transverse Coulomb-explosion yields 6 μm only. Hence, even in the extreme case the transverse bunch expansion is dominated by the initial divergence and for lower charges this dominance increases. If γ_0 is the bunch energy just before release into vacuum, γ' and β' the energy and velocity of a test electron in the bunch rest frame, γ and $\beta \approx 1$ for its laboratory frame energy and velocity, then one can clearly distinguish between a transverse-dominated expansion and a longitudinal-dominated one: in the first case, where the electron moves in the rest frame with velocity $\pm\beta'$ along transverse direction, $\gamma = \gamma_0\gamma'$, while in the latter case, where

Parameter	FLASH (fs)	TT-VUV-FEL	TT-XFEL
current	1.3 kA	50 kA	160 kA
norm. emitt.	6 mm mrad	1 mm mrad	1 mm mrad
beam size	170 μm	30 μm	30 μm
energy	461.5 MeV	150 MeV	1.74 GeV
energy spread	0.04%	0.5%	0.1%
und. period	27.3 mm	5 mm	5 mm
wavelength	30 nm	32 nm	0.25 nm
Pierce par.	0.002	0.01	0.0015
sat. length	19 m	0.8 m	5 m
pulse length	55 fs	4 fs	4 fs
sat. power	0.8 GW	2.0 GW	58 GW

TABLE 1 Parameters for the comparison between the DESY femtosecond-mode Flash-VUV case and the corresponding table-top VUV FEL as well as a table-top X-ray FEL (rms values)

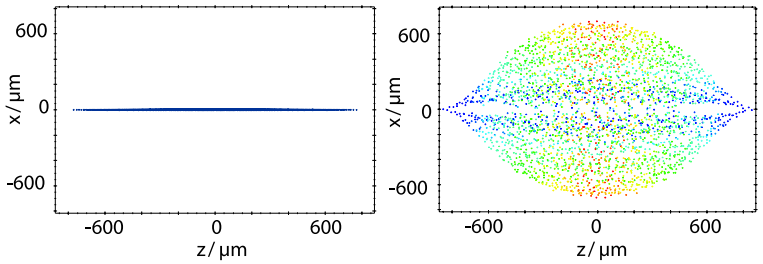

FIGURE 3 (Color online) Projected spatial electron distribution within the bunch rest frame in the extreme case, at $\tau = 0$ s (*left*) and $\tau = 4$ ps (*right*), from a GPT run. The color code indicates the electron energy (blue is initial kinetic energy, *red* is increased energy). The transverse expansion is clearly dominating

the electron moves with velocity $\pm\beta'$ in the beam direction, $\gamma = \gamma_0\gamma'(1 \pm \beta')$. Hence, in a purely transverse expansion all electrons gain kinetic energy, while in a purely longitudinal expansion, some electrons lose energy. The inset of Fig. 4 shows the absolute kinetic electron energy distribution along the bunch at a distance of $z = 3$ cm after its release into vacuum (in case of 0.6 nC). This spectrum shows that the bunch under study mostly undergoes a transverse expansion. The maximum energy gain lies in the middle of the bunch, where the density is highest, i.e., where initially the highest potential energy was stored. That the space-charge driven transverse expansion is weaker than the divergence-driven one is also confirmed by the fact that (even in the extreme case) the divergence is increased only to 1.3 mrad. After passing a focusing system (a triplet of quadrupoles, positioned at $z = 4$ cm, having a length of about 10 cm), the Gaussian-like energy distribution is transformed into a quasi-linear one, as depicted in Fig. 4. The reason is that in the resulting quasi-collimated low-divergence beam faster electrons can catch up the slower ones. Note that after $z = 3$ cm (inset) the fastest electrons are symmetrically distributed around the middle of the bunch. These electrons start overtaking the slower ones, that is, they move forward within the bunch. If initially longitudinal debunching dominates, the fastest electrons are found in the head and the slowest ones in the tail of the bunch.

A key parameter for SASE to occur is the energy spread σ_γ/γ, which must always be smaller than the Pierce parameter ϱ. The relevant energy spread is taken over a bunch slice with the size of one cooperation length, i.e. the slippage length of the radiation along the bunch over one gain length. As seen in Fig. 4, a large fraction of the bunch fulfills $\sigma_\gamma/\gamma < \varrho$. Due to the slippage of the radiation relative to the bunch, the linear energy chirp must be compensated, because the energy factor γ in (5) increases along the bunch. However, in case of short-period undulators the gap is correspondingly small (typically one third of the undulator period) and such small gaps lead to strong wakefields also causing an energy variation along the bunch [23, 24]. In case of ultrashort bunches, the characteristic length of the resistive wake potential is longer than the bunch length and, hence, the energy change is found to be negative with a linear few-percent variation along the bunch. This in turn implies that the bunch as a whole is decelerated during the passage of the undulator, whereby the head loses less energy than the tail. It turns out that the linear energy chirp induced by space-charge corresponds well with the wakefield-induced slowing down of the entire electron bunch. Therefore, the radiation slipping in the forward direction interacts with electrons of effectively constant energy, if by varying the gap the bunch energy loss is tuned with respect to the slippage. In other words, the space-charge effects and the wakefield effects cancel each other. We have found with simulations that for a first proof-of-principle of a table-top FEL the comparably low energy of 130–150 MeV is well suited to cope with the wakefields in the undulator. In this sense the table-top VUV case given in Table 1 can be regarded as an optimal test case.

Coherent synchrotron radiation (CSR) [20] as another source for increasing the (slice) energy spread within the undulator was found to have negligible impact. This was shown with CSRtrack simulations which take into account that in our cases the bunches have a much larger transverse size ($\sigma_{x,y} \sim 30$ µm) than length ($\sigma_z \sim 1$ µm).

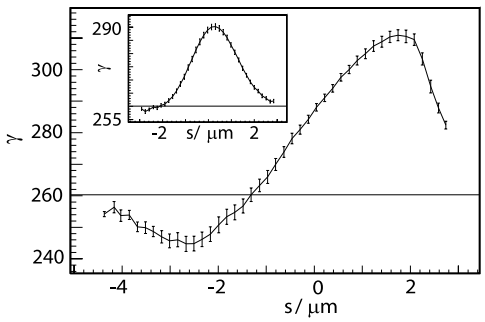

FIGURE 4 Energy vs. position (in co-moving frame) along the bunch before entering the undulator (GPT simulation): the Gaussian-like distribution after a drift of $z = 3$ cm behind the gas-jet (*inset*), indicating a transverse-dominated bunch expansion, is stretched into a quasi-linear one behind the focusing system. The vertical lines show the slice energy spread σ_γ and the horizontal lines mark the initial energy $\gamma_0 = 260$

2.2 *Table-top* XFEL

So far we have discussed a proof-of-principle scenario at relatively low electron energies, where space-charge effects play a dominant role leading to a linear energy chirp. The situation of the proposed table-top X-FEL (TT-XFEL) is different. For reaching a wavelength of $\lambda = 0.25$ nm, an electron energy of 1.74 GeV is needed in case of a period of $\lambda_u = 5$ mm. Space charge effects are much weaker here. For this less demanding situation we have confirmed with four different simulation codes (GPT, ASTRA [21], CSRtrack, HOMDYN [22]) that above 1 GeV, with the same parameters as in the extreme case given above, Coulomb-explosion leads to a projected energy chirp of below 0.3% and a bunch elongation with a fac-

tor below 1.1. Furthermore, CSR can be neglected in agreement with the 1D theory. Experimentally the most demanding constraint is that the Pierce parameter is one order of magnitude smaller than in the test case at 130 MeV, hence the electron (slice) energy spread should be as small as 0.1%. This goal seems to be within reach considering the bubble-transformation scenario mentioned above.

Without the effect of wakefields GENESIS simulations have shown that this TT-XFEL scenario with an undulator length of only 5 m yields 8×10^{11} photons/bunch within ~ 4 fs and 0.2% bandwidth, a divergence of 10 μrad, and a beam size of 20 μm. However, the wakefields become the dominant degrading effect as the required undulator length is larger and the Pierce parameter reduced, hence also the tolerance with respect to variations in the electron energy. But since there is no initial space-charge-induced energy chirp, one must find another method for compensating the wakefield-induced energy variation. A suitable method for compensating the wakefields for the TT-XFEL would be tapering, i.e., varying the undulator period along the undulator. Due to the fact that the undulator parameter K is smaller than unity, tapering via K, i.e., by gap variation, could only be used as fine-tuning. Depending on the specific material properties of the undulator surface, our first wake calculations show that the bunch center loses over the entire 5 m undulator length about 10% of its initial energy. Due to the linear wake field variation along the bunch only a fraction of it will undergo SASE. A detailed study will be further investigated in a future paper.

2.3 *Experimental status*

In order to demonstrate practical feasibility, we have built and tested a miniature focusing system and undulator consisting of permanent magnets. The focusing triplet consists of mini-quadrupoles with an aperture of just 5 mm, hence allowing for measured gradients of 530 T/m. Their focusing strength was measured with a 600 MeV electron beam (at Mainz Microtron facility MAMI, Mainz, Germany). A first test hybrid undulator with a period of only 5 mm and a peak magnetic field strength of ~ 1 T has been built, and produced, with a 855 MeV beam (also at MAMI), an undulator radiation spectrum as expected. These results will be published elsewhere.

3 Conclusion

We have shown by means of analytical estimates and SASE FEL simulations that laser-plasma accelerator-based FELs can only be operated with meter-scale undulators. The key parameter is the ultra-high electron peak current, which significantly reduces the gain length and increases the tolerance with respect to the energy spread and emittance. The latter would also allow increasing of the TT-XFEL photon energy into the medically relevant range of 20–50 keV, because the limiting quantum fluctuations in the spontaneous undulator radiation, scale with γ^4 [25] and the required electron energy of the TT-XFEL is comparatively small.

ACKNOWLEDGEMENTS We thank W. Decking, M. Dohlus, K. Flöttmann, T. Limberg, and J. Rossbach (all DESY) for fruitful discussions. Supported by Deutsche Forschungsgemeinschaft through the DFG-Cluster of Excellence Munich-Centre for Advanced Photonics. This work was also supported by DFG under Contract No. TR18.

REFERENCES

1 S.P.D. Mangles, C. Murphy, Z. Najmudin, A. Thomas, J. Collier, A. Dangor, E. Divall, P. Foster, J. Gallacher, C. Hooker, D. Jaroszynski, A. Langley, W. Mori, P. Norreys, F. Tsung, R. Viskup, B. Walton, K. Krushelnick, Nature **431**, 535 (2004)
2 C.G.R. Geddes, C. Toth, J. van Tilborg, E. Esarey, C. Schroeder, D. Bruhwiller, C. Nieter, J. Cary, W. Leemans, Nature **431**, 538 (2004)
3 J. Faure, Y. Glinec, A. Pukhov, S. Kiselev, S. Gordienko, E. Lefebvre, J.-P. Rousseau, F. Burgy, V. Malka, Nature **431**, 541 (2004)
4 W.P. Leemans, B. Nagler, A. Gonsalves, C. Toth, K. Nakamura, C. Geddes, E. Esarey, C. Schroeder, S. Hooker, Nature Phys. **2**, 696 (2006)
5 R. Neutze, R. Wouts, D. van der Spoel, E. Weckert, J. Hajdu, Nature **406**, 752 (2000)
6 A. Baltus, T. Udem, M. Uiberacker, M. Hentschel, E. Goulielmakis, C. Gohle, R. Holzwarth, V.S. Yakovlev, A. Scrinzi, T.W. Hänsch, F. Krausz, Nature **421**, 611 (2003)
7 W. Thomlinson, P. Suortti, D. Chapman, Nucl. Instrum. Methods Phys. Res. A **543**, 288 (2005)
8 A. Pukhov, J. Meyer-ter-Vehn, Appl. Phys. B **74**, 355 (2002)
9 A. Pukhov, S. Gordienko, Philos. Trans. R. Soc. London A **364**, 623 (2006)
10 M. Geissler, J. Schreiber, J. Meyer-ter-Vehn, New J. Phys. **8**, 186 (2006)
11 D.J. Spence, A. Butler, S. Hooker, J. Opt. Soc. Am. B **20**, 138 (2003)
12 http://www.attoworld.de/research/PFS.html
13 R. Bonifacio, C. Pellegrini, L.M. Narduci, Opt. Commun. **50**, 373 (1984)
14 S. Reiche, Nucl. Instrum. Methods Phys. Res. A **429**, 243 (1999)
15 M. Xie, Nucl. Instrum. Methods Phys. Res. A **445**, 59 (2000)
16 Technical Design Report: http://www.hasylab.desy.de/facility/fel/vuv/ttf2_update/TESLA-FEL2002-01.pdf
17 M.J. de Loos, S.B. van der Geer, Proc. 5th Eur. Part. Acc. Conf., Sitges, 1241 (1996)
18 M. Dohlus, T. Limberg, Proc. FEL 2004 Conf., 18-21
19 G. Fubiana, J. Qiang, E. Esarey, W.P. Leemans, Phys. Rev. ST Accel. Beams **9**, 064 402 (2006)
20 E. Saldin, E.A. Schneidmiller, M.V. Yurkov, Nucl. Instrum. Methods Phys. Res. A **417**, 158 (1998)
21 K. Floettmann, Astra User's Manual, 2000, http://www.desy.de/mpyflo/
22 M. Ferrario, J.E. Clendenin, D.T. Palmer, J.B. Rosenzweig, L. Serafini, Proc. of the 2nd ICFA Adv. Acc. Workshop on "The Physics of High Brightness Beams", UCLA, Nov., 1999; see also SLAC-PUB-8400
23 A.W. Chao, *Physics of Collective Beam Instabilities in High Energy Accelerators* (Wiley, New York, 1993)
24 K. Bane, SLAC-PUB-11829 (2006)
25 M. Sands, Phys. Rev. **97**, 470 (1955)

Chapter VI

Quadrupole Undulator

Title of publication:
Design Study for a Strong Focusing Quadrupole Undulator

submitted to PHYSICAL REVIEW SPECIAL TOPICS - ACCELERATORS AND BEAMS

The additional references [136]-[139] are included in this publication.

Design Study for a Strong Focusing Quadrupole Undulator

S. Becker,[1,*] A.R. Maier,[1] S. Raith,[1] C. Frevert,[1] M. Fuchs,[1] P. Polzer,[1]
W. Rittershofer,[1] M. Scheer,[2] T. Seggebrock,[1] R. Weingartner,[1] and F. Grüner[1]

[1] *Ludwig-Maximilians-Universität München, 85748 Garching, Germany*
[2] *Helmholtz-Zentrum Berlin, Berlin, Germany*

We present a design study for an undulator built from quadrupole magnets. The dipole field component required for the undulating motion is introduced by positioning individual quadrupoles off the undulator device axis. The quadrupole undulator has strong intrinsic focusing properties which can sustain a significantly reduced electron beam diameter over a long distance while still permitting well defined tuning and tapering. A reduced beam diameter reduces the photon beam spot size of spontaneous undulator radiation and could also proof benefit in compact free-electron laser experiments.

PACS numbers: 41.85.Lc, 07.85.Qe, 41.60.Cr

I. INTRODUCTION

Undulators have been established as brilliant light sources for decades [1]. A planar undulator consists of dipole magnetic fields, which are alternately orientated and force an electron beam on a sinusoidal trajectory. The transverse acceleration leads to emission of spontaneous undulator radiation. Based on this principle undulators are usually installed at large-scale synchrotron facilities, delivering brilliant photon beams for various branches of science.

Just recently laser-plasma accelerated electrons [2–7] have been used to generate spontaneous undulator radiation in the soft x-ray range [8]. Extending this concept into the hard x-ray range, ultrafast x-ray pump probe experiments on a few ten femtosecond timescale become feasible on a university-lab scale. Even protein structure analysis experiments with tunable spontaneous undulator radiation in the low keV range are thus permitted.

Those experiments would benefit from a decrease in the transverse beam size σ_x. Some proteins can be crystallized only to a size of a few ten microns. An electron beam, and thus a radiation spot, having the size of the protein crystal would allow to maximize the photon flux on the target.

σ_x is minimized by focusing the electron beam within the undulator using two major focusing mechanisms:

- External focusing: A strong focusing FODO lattice is built from external quadrupoles. These quadrupoles can be integrated in the undulator device. Alternatively, the undulator is split into modules, which are placed within the drift sections of the FODO lattice.

- Natural focusing: The beam size is kept constant using the undulator's intrinsic focusing.

*Corresponding author; Electronic address: stefan.becker@physik.uni-muenchen.de

Considering a very compact table-top size experiment, splitting the undulator into modules seems not favorable as it prolongs the undulator beam line.

Dipole-based undulators yield natural focusing due to field gradients emerging from the alternating dipole field components. However the intrinsic focusing of dipole undulators is comparably weak and only existent in one transverse beam plane. An advanced concept extends natural focusing to both transverse planes by utilizing parabolic shaped magnets [9]. Due to mechanical complications this scheme is rarely used. The natural focusing of a planar Halbach type dipole undulator [10] is described by

$$k = \left(\frac{\sqrt{2}\pi K}{\lambda_U \gamma}\right)^2 = \left(\frac{eB_0}{\sqrt{2}\gamma m_e c}\right)^2, \quad (1)$$

with k being the focusing strength, λ_U the undulator period length, B_0 the on-axis magnetic peak field and K the undulator parameter with $K = eB_0\lambda_U/2\pi m_e c$, where e is the charge and m_e is the mass of the electron. An electron beam is considered to be matched to the undulator if the defocusing effect of the emittance ϵ is compensated by the focusing strength k of the undulator. The matched beam size σ_m is

$$\sigma_m = \sqrt{\frac{\epsilon}{\sqrt{k}}}. \quad (2)$$

Thus, a planar undulator using a typical peak undulator field of 1 T yields a matched beam size of not smaller than $\sigma_m = 49$ μm at $k = 0.43$ for $\gamma = 626$ and a normalized emittance of $\epsilon_n = 1$ mm.mrad due to natural focusing.

In the following, we present a design for a strong intrinsic focusing undulator built from a channel of permanent magnet quadrupole devices, which focuses equally on both beam planes. The beam diameter thus can be kept small and at constant values over a long distance. The deflection of the electron beam is achieved by positioning individual quadrupole devices off the beam axis by x_{off}, reaching a peak magnetic dipole field of $\hat{B} = g_B x_{\text{off}}$ with $g_B = dB/dx$ being the magnetic field gradient. Detri-

mental effects on the beam quality are minimized by using highly tunable quadrupoles presented before [11].

This publication is structured as follows: In II A we describe the design concept for a quadrupole undulator followed by numerical simulations in II B showing electron beam trajectories. In section II C we compare the expected undulator radiation from the quadrupole undulator with a conventional planar undulator. After an analytical description of its focusing properties in section III we describe the problem to couple the electron beam into the undulator in section IV and conclude with an outlook on the current experimental status.

II. QUADRUPOLE UNDULATOR

A. Design Concept

In [11] we presented highly tunable permanent magnet quadrupoles (TPMQ) of gradients $g_B = 500$ T/m with an aperture radius of 3 mm, which follow the Halbach design [12]. The magnetic field measured along a ring within the aperture of a TPMQ can be expanded into a Fourier series. Thereby, detailed knowledge of the higher order field components introduced by each single magnet wedge is gained. Undesirable higher order field components can be corrected by displacing the wedges in a controlled manner. This allows to illuminate the TPMQ even off-axis without significant deterioration of the electron beam emittance.

We propose an undulator design using TPMQs that is based on a channel of focusing/defocusing TPMQs of length $\lambda_U/2$ with λ_U being the undulator period. The alternating transverse displacement of the TPMQs by x_{off} introduces dipole field components of strength $\hat{B} = g_B x_{\text{off}}$. This forms an alternating B-field along the device axis.

A stable configuration needs to decouple the deflection properties leading to the undulating electron trajectories from the focusing properties. A simple displacement of the electron beam from the device's symmetry axis leads to a global deflection of the beam (Fig. 1a). A straight electron trajectory requires an arrangement of periodically displaced quadrupoles such that the electron beam is on the device axis. This condition is fulfilled for a two-fold focusing undulator as shown in Fig. 1b. Focusing period lengths being multiples of the minimal focusing period can be selected as well, such as the four-fold focusing undulator as shown in Fig. 1c.

B. Numerical Simulations

We examined the feasibility of the quadrupole undulator with numerical simulations and tolerance studies. We have chosen a four-fold focusing quadrupole undulator in the following as shown in Fig. 1c because the larger focusing period length leads to a larger intrinsic focusing

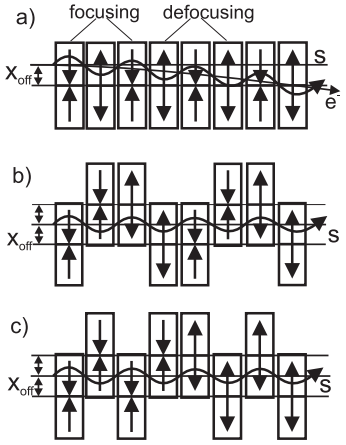

FIG. 1: Examples of quadrupole undulators are shown schematically. a) One-fold focusing quadrupole undulator, meaning one focusing period length equals one undulator period length. With the undulator period λ_U equal to the focusing period the initially displaced (x_{off}) electron beam leaves the initial beam axis z. b) Two-fold focusing quadrupole undulator: The focusing period length is two times the undulator period length. c) Four-fold focusing quadrupole undulator.

strength of the undulator. The magnet configuration of a single quadrupole as well as the B-Field along the longitudinal axis, displaced transversely by x_{off}, is shown in Fig. 2 for quadrupoles of different lengths.

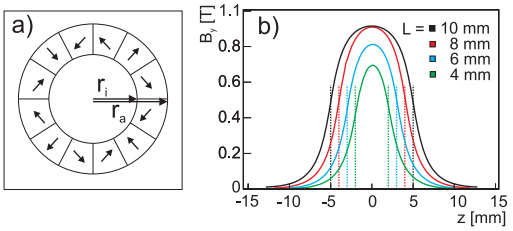

FIG. 2: a) Tunable Permanent Magnet Quadrupoles (TPMQ) with inner radius $r_i = 3$ mm and outer radius $r_a = 10$ mm. b) $B_y \approx |\vec{B}|$ along the longitudinal position s inside the quadrupole at a transverse off-axis position of $x = 1.8$ mm for different quadrupole lengths $L = 4$ mm, 6 mm, 8 mm and 10 mm.

The magnetic field of an assembled quadrupole differs from the ideal quadrupole field distribution. Basically there are three different sources of errors. The quadrupole design symmetry, i.e. the specific number of magnet wedges, introduces higher order field components. Furthermore, the magnetic field axis and the geometric shape of the actual manufactured magnet wedges will have certain tolerances, which introduce additional higher order field components. Finally, the quadruple field orientation may by tilted around the geometric cen-

ter of the quadrupole, which would significantly lower the electron beam quality.

We calculated the magnetic field distribution of a single quadrupole using EM-Studio [13]. In the calculations we presumed perfectly shaped magnet wedges. The higher order magnetic field components, which originate from the quadrupole device symmetry, are included in the field calculation. Remaining errors can in principle be minimized with the tuning procedure presented in [11]. In the following we assume, that we are able to tune the quadrupoles to the desired accuracy. Thus for first basic considerations it is sufficient to assume idealized magnet wedges for field calculations.

The tunable quadrupoles are solely built from permanent magnet materials which can assumed to be transparent for magnetic fields. Hence, non-linearities due to hysteresis effects are neglected. The calculation of the magnetic field distribution of a single quadrupole is used to compute the undulator field by superimposing the calculated fields of the quadrupole. This method neglects the field variations from quadrupole to quadrupole, which are still present after the tuning process. This has to be subject of further studies.

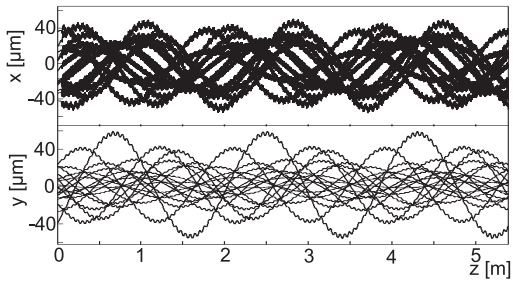

FIG. 3: Electron beam at an energy of 320 MeV and a normalized emittance of $\epsilon_n = 1$ mm.mrad propagating through a four-fold quadrupole undulator with $\lambda_U = 14$ mm. Both transverse spatial directions are shown. The upper graph shows the undulating plane with the apparently thicker lines resulting from the electrons' undulating motion superimposed to the trajectories due to focusing. The rms beam size is $\sigma_m = 20$ μm.

We calculated the complete B-Field map of a four-fold quadrupole undulator built from single quadrupoles with field gradients of 450 T/m, $\lambda_u = 14$ mm and $x_{\text{off}} = 1.8$ mm. We performed beam propagation calculations utilizing the tracking code GPT [14]. Electron trajectories are shown in Fig. 3. Despite the undulator being relatively long, the emittance does not increase, which can also be seen from the beam size remaining at constant values. The configuration in Fig. 3 keeps the electron beam at a constant value of $\sigma_m = 20$ μm over a distance of several meters.

C. Undulator radiation

Undulator radiation was calculated numerically in 3D using the generated magnetic field map for evaluating the electron trajectory. The code used is WAVE [15], which is capable of processing 3D magnetic field maps for tracking the electrons and calculating the undulator radiation spectrum on an array of observation points. Paramters for the calculations are $\lambda_U = 14$ mm and $\gamma = 626$.

Fig. 4 compares the undulator radiation of an ideal planar undulator with the radiation emitted by the quadrupole undulator. Fig. 4a shows the single-electron spectrum of an on-axis electron in an ideal planar undulator of magnetic field $B = 0.72$ T. The undulator parameter is $K = 0.927$ and following the well-known resonance formula

$$\lambda = \frac{\lambda_U}{2\gamma^2}\left(1 + \frac{K^2}{2} + \gamma^2\theta^2\right), \tag{3}$$

radiation of wavelength $\lambda = 25.5$ nm, i.e. $E = 48.5$ eV is emitted on-axis. With the observation angel θ the parabolic shape of the angle dependent energy spectrum is clearly visible (Fig. 4a.IV).

Fig. 4b presents the corresponding case of an on-axis electron propagating through a quadrupole undulator build from TPMQs of gradient $g_B = 450$ T/m. The quadrupoles are displaced by $x_{\text{off}} = 1.8$ mm off the device axis. Superposition of the single quadrupole fields decreases the on-axis magnetic field to $B = 0.71$ T. An additional small B-Field variation (compare Fig. 4b.II) is a result of fringe field superposition of the alternating displaced quadrupoles. Fig. 5 compares the electron trajectory and the corresponding B-field for an ideal planar undulator and the proposed quadrupole undulator. Due to the slightly altered B-field, the electron trajectory in the quadrupole undulator is a few percent longer compared to the ideal planar undulator. This causes a shift of the emitted wavelength to $\lambda = 26.4$ nm. As the undulator parameter is a measure for the amplitude of the sinusoidal electron trajectory in an ideal planar undulator, this behavior can be absorbed in an effective undulator parameter K' for the quadrupole undulator and $K' = 0.977 = 1.054K$.

Finally, Fig. 4c shows an electron in the quadrupole undulator with a large betatron oscillation amplitude of about 40 μm. Note, that this oscillation is much larger than the presumed beam size of $\sigma_m = 20\mu$m. Even in this extreme case the fundamental peak of the emitted energy spectrum does not significantly deviate from the spectrum emitted by an on-axis electron. Thus, the constant focusing of the electron in the quadrupole undulator does not degrade the emitted spectrum.

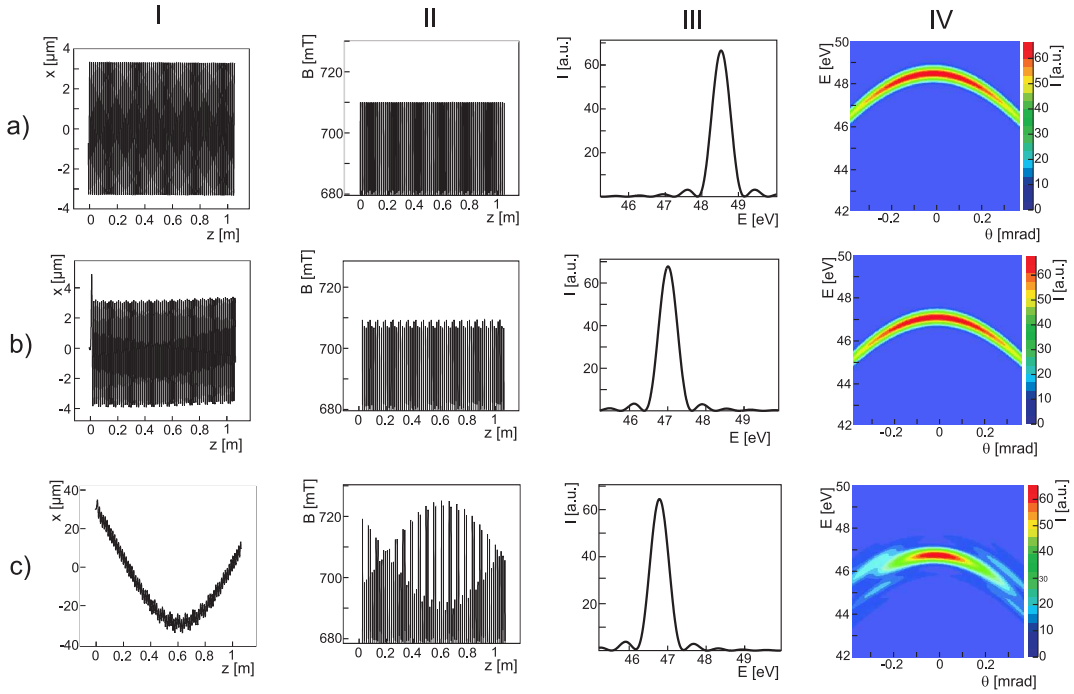

FIG. 4: Single electron spectrum calculations at an electron energy of 320 MeV for (a) an ideal undulator, (b) a four-fold focusing quadrupole undulator with an electron on axis and (c) the same quadrupole undulator with an electron performing a strong betatron oscillation. (I) shows the trajectories in the undulating plane, (II) the magnetic field experienced by the electron along its trajectory, (III) the spectrum of the undulator radiation's fundamental peak and (IV) the spectrum of the fundamental peak against the observation angle θ within the undulating plane.

III. ANALYTICAL TREATMENT

Important quantities concerning the analytical description of the quadrupole undulator can be obtained considering a quadrupole channel. From the effective focusing strength k^* of a single quadrupole we derive the effective focusing strength k' of the quadrupole undulator. Using Eq. 2 we calculate the matched beam size σ_m.

A. Effective Focusing of a Harmonic Magnetic Field Oscillation

We first consider an individual quadrupole device, shown in Fig. 2. It can be seen that the peak field and hence the field gradient saturates at a length of 8 mm. Below this value, the ratio of length and aperture of the quadrupole is too small for the field to reach a maximum gradient.

We present a specific case, where the TPMQs have a length of 6 mm, a field gradient of 450 T/m and an aperture radius of 3 mm. The undulator period length is $\lambda_U = 14$ mm, with a gap of 1 mm between the TPMQs. Fig. 5a) shows the magnetic field of a quadrupole undulator with an off-axis displacement of 1.8 mm or 60 % of the aperture radius. Fringe fields of neighboring quadrupoles reduce the gradient to 400 T/m. The resulting dipole component is 710 mT which is a peak value of the magnetic field on the quadrupole undulator axis.

The effective focusing strength over one quadrupole k^* is obtained by continuously multiplying thin focusing transport matrices modeling the course of the magnetic field as shown in Fig. 5a). The focusing beam plane of the quadrupole is described using the linear transport matrix

$$\mathbf{QF}(\mathbf{s},\mathbf{k}) = \begin{pmatrix} \cos\Omega & \frac{1}{\sqrt{k}}\sin\Omega \\ -\sqrt{k}\sin\Omega & \cos\Omega \end{pmatrix} \qquad (4)$$

with $\Omega = \sqrt{k}s$ and s the longitudinal position along the quadrupole. With $s = n\lambda_U/2$ for an n-fold focusing quadrupole undulator the effective transport matrix is given by

$$\mathbf{QF_{m,Eff}}(\mathbf{s},\mathbf{k}) = \prod_{\mathbf{i=1}}^{\mathbf{m}} \mathbf{QF}\left[{}^{s}/_{\mathbf{m}}, \mathbf{k}\sin({}^{i}/_{\mathbf{m}}\,\pi)\right]. \qquad (5)$$

The comparison of $\mathbf{QF_{m,Eff}}(\mathbf{s},\mathbf{k})$ and $\mathbf{QF}(\mathbf{s},\mathbf{k})$ yields convergence of k^*/k as shown in Fig. 6a for a specific

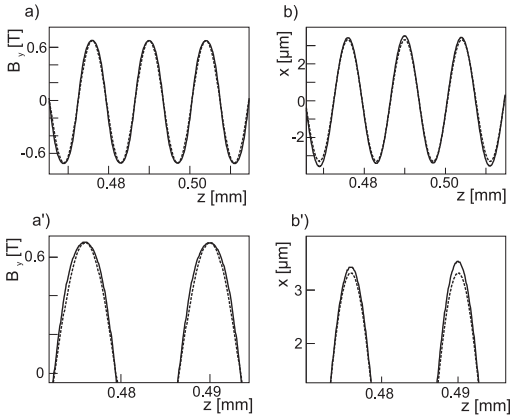

FIG. 5: The magnetic field on the device axis of the quadrupole undulator (solid line) in comparison with an ideal dipole undulator (dashed line) is shown in (a). The resulting trajectories rendered from the magnetic fields are presented in (b), where the amplitude of the quadrupole undulator is slightly increased. (a') and (b') show a close-up of the figures above.

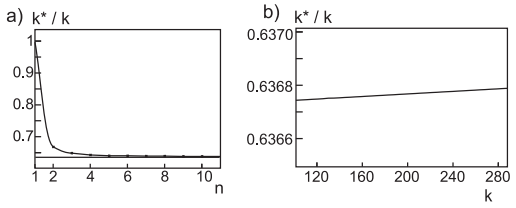

FIG. 6: a) The ratio of the effective focusing strength inside the quadrupole k^* and the peak focusing strength $k = 211$ m^{-2}. b) The converged factor $^{k^*}/_k$ for $m \to \infty$ is practically constant over a wide range of k.

$k = 211$ m^{-2}, which is the peak focusing strength of a quadrupole as considered here. For $m \to \infty$, we finally obtain $k^*/k = 0.637$.

There is virtually no dependence of $^{k^*}/_k$ on k for $100 < k < 300$ as shown in Fig. 6b and thus, we can assume a constant value in the range of our interest.

B. Effective Focusing of the Quadrupole Channel

In the following we derive the effective focusing strength of the quadrupole undulator k' to calculate the matched beam size. A beam remains at constant size within a transport element $\mathbf{M}$ if the matched beam condition

$$\mathbf{B} = \mathbf{M}^{\mathbf{T}}\mathbf{B}\mathbf{M} \tag{6}$$

is met for the beta matrix $\mathbf{B}$,

$$\mathbf{B} = \begin{pmatrix} \beta_0 & -\alpha_0 \\ -\alpha_0 & \gamma_0 \end{pmatrix}, \tag{7}$$

with the well-known twiss parameters α_0, β_0 and γ_0 [19]. A simple focusing transport element of length s given by

$$\mathbf{M} = \begin{pmatrix} \cos\Omega & \frac{1}{\sqrt{k}}\sin\Omega \\ -\sqrt{k}\sin\Omega & \cos\Omega \end{pmatrix}. \tag{8}$$

$\Omega = \sqrt{k}s$ in combination with the matched beam condition (Eq. 6) yields Eq. 2. The focusing strength of a quadrupole channel is deduced using a focusing and a defocusing transport element given by

$$\mathbf{QF}^* = \begin{pmatrix} \cos\Omega^* & \frac{1}{\sqrt{k^*}}\sin\Omega^* \\ -\sqrt{k^*}\sin\Omega^* & \cos\Omega^* \end{pmatrix}, \tag{9}$$

$$\mathbf{QD}^* = \begin{pmatrix} \cosh\Omega^* & \frac{1}{\sqrt{k^*}}\sinh\Omega^* \\ \sqrt{k^*}\sinh\Omega^* & \cosh\Omega^* \end{pmatrix}, \tag{10}$$

with $\Omega^* = \sqrt{k^*}s$. The resulting transport element $\mathbf{M} = \mathbf{QF}^* \cdot \mathbf{QD}^*$ together with the matched beam condition (Eq. 6) finally yields

$$k' = k^* \, \frac{3/2 - \cos(2\Omega^*)\cosh^2(\Omega^*) - 1/2\cosh(2\Omega^*)}{\cosh(2\Omega^*) - \cos(2\Omega^*) + \sin(2\Omega^*) + \sinh(2\Omega^*)}. \tag{11}$$

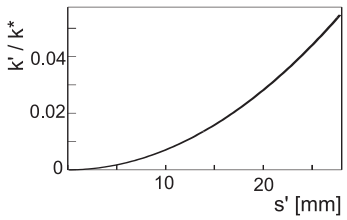

FIG. 7: Eq. 11 for the case of quadrupole devices with a gradient of 500 T/m. s' is the focusing period which consists of a focusing and a defocusing element.

Fig. 7 shows Eq. 11 using quadrupole devices with a gradient of 500 T/m in dependence of the focusing period $s' = 2s$. For the case of the quadrupole channel presented above we obtain a matched beam size of only 20 μm. This corresponds to a beta function of $\beta = 0.25$ m, for the presumed electron beam with $\gamma = 626$ and $\epsilon_n = 1$ mm.mrad.

IV. COUPLING IN

Laser-plasma based sources yield electron beam divergences of about 1 mrad and a source size of few microns. It is challenging to image this source into a collimated beam of small size, such as $\sigma_m = 20$ μm in our case.

Collimation in this context means to achieve a Courrant-Snyder $\alpha_0 = 0$ at the beginning of the undulator and thus a waist at $\sigma_0 = 20$ μm. Using a doublet or a triplet would require very long drift distances, resulting in enlarged setups and sensitive adjustment conditions. This is certainly not a particular problem of the quadrupole undulator itself, but contradicts of course the goal of a compact setup.

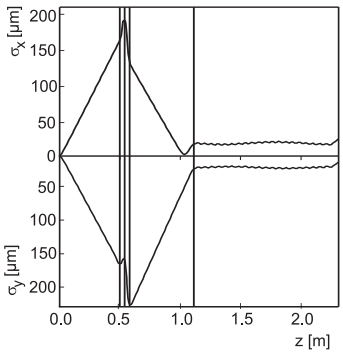

FIG. 8: Possible beam guidance system for coupling into a quadrupole undulator shown in horizontal and vertical beam plane. The four vertical lines represent the quadrupole device positions. The quadrupole undulator entrance is right behind the last quadrupole at 1.1 m. The drift distances are 500 mm, 10 mm, 10 mm and 500 mm. The length of the quadrupole are 10.8 mm, 33.3 mm, 23.2 mm and 30.6 mm.

A possible solution is shown in Fig. 8. This beam-guidance concept allows to collimate the laser-plasma accelerated beam at a large divergence to small sizes. The first element is a triplet to refocus the divergent beam. The collimating element is a high gradient single quadrupole which defocuses one converging plane of the electron beam. The other electron beam plane is configured such that the beam passes through a waist and the focusing plane of the quadrupole also collimates the beam at the desired size. Yet, it imposes further requirements to the position accuracy and magnetic field tolerance of the coupling quadrupoles, as well as the electron beam stability.

V. CONCLUSION AND OUTLOOK

The presented quadrupole undulator concept allows to keep the beam size at a small and constant size over a long distance. This can be beneficial for compact spontaneous undulator radiation experiments as well as table-top free-electron lasers.

The presented concept has advantages over conventional designs in terms of tuning and tapering. Whereas field errors in conventional undulators have to be corrected by shimming, the quadrupole undulator design would allow to correct the field by simply adjusting the transverse displacement of the single quadrupoles. Assuming a field gradient of 500 T/m and micrometer position accuracy this is possible with sub-percent precision. For the transverse components, each single period can be adjusted independently, since the quadrupoles have no iron components, and the superposition of the B-Field can be assumed linear. The same concept can be used to taper the undulator, i.e. to adjust the undulator parameter K along the undulator by altering the field strength, and therefore correct wake field and space charge induced energy chirps [18].

A further application of the quadrupole undulator could be in a compact free-electron laser experiment [16]. In the special regime of a free-electron laser (FEL), coherent amplification of the undulator radiation increases the total emitted radiation and photon beam brilliance by several orders of magnitude compared to the solely spontaneous radiation. Among the main parameters describing an FEL is the saturation length L_{sat}, which is the undulator length required to obtain a maximum in emitted radiation power. The saturation length scales in the 1D FEL theory with the beam diameter σ_x as $L_{\mathrm{sat}} \propto \sigma_x^{2/3}$ [17]. Thus by decreasing σ_x the saturation length can be significantly reduced.

However, several effects, that play an important role due to the quadrupole undulator's specific design concept, have to be considered. Of course diffraction effects limit the reasonable beam radius, dependent on the FEL design wavelength. For a fixed emittance, an ever decreasing beam size concurrently increases the axial velocity spread. This can be interpreted as an increased effective energy spread, which hinders the FEL process.

In Fig. 4c a small spectral broadening resulting from electrons far off the device axis has been observed. Driving an FEL it has to be ensured that the overall spectral broadening of the quadrupole undulator still fulfills the condition $\Delta\lambda/\lambda < \rho$, with ρ the dimensionless FEL parameter [17] and usually $\rho < 1$ %. Our group is currently examining the impacts of these effects on the FEL process and the possibilities to drive a table-top FEL by the proposed quadrupole undulator.

The undulator concept however, relies crucially on the ability to precisely correct higher order field components in the utilized quadrupoles. Of course, the longitudinal magnetic field can not be adjusted using the method in [11] and magnet wedges have to be manufactured within the required tolerances, to keep the longitudinal component sufficiently homogeneous. To examine the practical feasibility we are currently building a first undulator prototype to explore our capability to tune the quadrupoles to the desired accuracy and to couple an electron beam into the undulator.

Acknowledgments

We thank Sven Reiche (Paul Scherrer Institut), Atoosa Meseck, Andreas Gaupp and Johannes Bahrdt (all

Helmholtz Zentrum Berlin) for fruitful discussions and comments. This work has been funded by DFG through transregio TR18 and supported by the DFG cluster-of-excellence Munich-Centre for Advanced Photonics (MAP).

[1] P. Elleaume, J. Chavanne, B. Faatz, Nucl. Instrum. Methods Phys. Res. Sect. A **455**, 503 (2000).
[2] S. P. D. Mangles, C. D. Murphy, Z. Najmudin, A. G. R. Thomas, J. L. Collier, A. E. Dangor, E. J. Divall, P. S. Foster, J. G. Gallacher, C. J. Hooker, D. A. Jaroszynski, A. J. Langley, W. B. Mori, P. A. Norreys, F. S. Tsung, R. Viskup, B. R. Walton, K. Krushelnick, Nature **431**, 535 (2004).
[3] C. G. R. Geddes, Cs. Toth, J. van Tilborg, E. Esarey, C. B. Schroeder, D. Bruhwiler, C. Nieter, J. Cary, W. P. Leemans, Nature **431**, 538 (2004).
[4] J. Faure, Y. Glinec, A. Pukhov, S. Kiselev, S. Gordienko, E. Lefebvre, J.-P. Rousseau, F. Burgy, V. Malka, Nature **431**, 541 (2004).
[5] W. P. Leemans, B. Nagler, A. J. Gonsalves, Cs. Toth, K. Nakamura, C. G. R. Geddes, E. Esarey, C. B. Schroeder, S. M. Hooker, Nature Physics **2**, 696 (2006).
[6] S. Karsch, J. Osterhoff, A. Popp, T. P. Rowlands-Rees, Zs. Major, M. Fuchs, B. Marx, R. Hörlein, K. Schmid, L. Veisz, S. Becker, U. Schramm, B. Hidding, G. Pretzler, D. Habs, F. Grüner, F. Krausz, S. M. Hooker, New J. Phys. **9**, 415 (2007).
[7] J. Osterhoff, A. Popp, Zs. Major, B. Marx, T. P. Rowlands-Rees, M. Fuchs, M. Geissler, R. Hörlein, B. Hidding, S. Becker, E. A. Peralta, U. Schramm, F. Grüner, D. Habs, F. Krausz, S. M. Hooker, and S. Karsch, Phys. Rev. Lett. **101**, 085002 (2008).
[8] M. Fuchs, R. Weingartner, A. Popp, Zs. Major, S. Becker, J. Osterhoff, I. Cortrie, R. Hörlein, G. D. Tsakiris, U. Schramm, T. P. Rowlands-Rees, S. M. Hooker, D. Habs, F. Krausz, S. Karsch, F. Grüner, submitted.
[9] E. T. Scharlemann, J. Appl. Phys. **58**, 2154 (1985).
[10] R.P. Walker, Nucl. Instrum. Methods in Phys. Res. **214**, 497 (1983).
[11] S. Becker, M. Bussmann, S. Raith, M. Fuchs, R. Weingartner, P. Kunz, W. Lauth, S. Schramm, M. El Ghazaly, F. Grüner, H. Backe, D. Habs, arXiv 0902.2371
[12] K. Halbach, Nucl. Instrum. Methods **187**, 109 (1981).
[13] CST EM Studio, www.cst.com.
[14] General Particle Tracer, www.pulsar.nl.
[15] Michael Scheer, PhD. thesis, Humboldt-Universität zu Berlin (2008).
[16] F. Grüner, S. Becker, U. Schramm, T. Eichner, M. Fuchs, R. Weingartner, D. Habs, J. Meyer-ter-Vehn, M. Geissler, M. Ferrario, L. Serafini, B. an der Geer, H. Backe, W. Lauth, S. Reiche, Appl. Phys. B **86**, 431 (2007).
[17] R. Bonifacio, C. Pellegrini, L. M. Narducci, Opt. Commun. **50**, 373 (1984).
[18] F. J. Grüner, C. B. Schroeder, A. R. Maier, S. Becker and Y. M. Mikhailova, Phys. Rev. ST Accel. Beams **12**, 020701 (2009).
[19] E. D. Courant and H. S. Snyder, Annals of Physics **3**, 1-48 (1958).

Appendix A

Geometrical Center of Multipole Devices

The expansion of higher order magnetic field components as introduced in section 4.2 requires the knowledge of the radius ρ [Eq. (4.10)]. Determining ρ requires the knowledge of the center of rotation with respect to the Hall probe which can experimentally obtained only requiring the Hall probe signal.

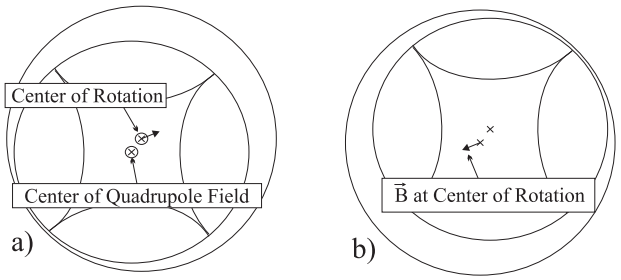

Figure A.1: a) General case of a quadrupole mounted on a measurement setup: The center of rotation is not equal to the center of the magnetic field. b) After the rotation of 180°. The field vector at the center of rotation is inverted.

Fig. A.1 schematically shows the general case, where the center of the magnetic field does not coincide with the center of rotation.

An example measurement that senses whether or not the Hall probe is located within the center of rotation is given by rotating the quadrupole and measuring the B-field flux through the Hall probe every 45°. The conditions shown in Table A.1 have to be met within the desired precision.

The position of the Hall probe at the center of the axis of rotation can be approached according to Figure A.2 using a simple feedback algorithm, which keeps rotating the quadrupole back and forth by 180° until the desired precision is achieved. This proce-

Angle	0	45	90	135	180	225	270	315
B-Field	a	b	c	d	-a	-b	-c	-d

Table A.1: Hall probe signal at the quadrupole center of rotation.

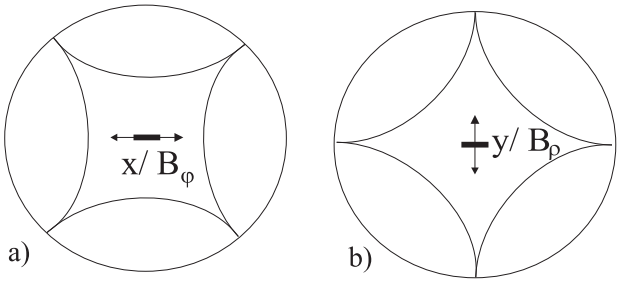

Figure A.2: a) Finding the center of the x-axis, scanning the azimuthal field component B_φ. b) Finding the center of the y-axis, scanning the radial field component B_ρ.

dure has to repeated alternatingly for the radial and the azimuthal axis.

Bibliography

[1] D. Strickland and G. Mourou, Optics Communications **56** (3), 219 (1985).

[2] T. Tajima and J.M. Dawson, Phys. Rev. Lett. **43**, 267 (1979).

[3] A. Pukhov and J. Meyer-ter-Vehn, Appl. Phys. B **74**, 355 (2002).

[4] S.P.D. Mangles, C. Murphy, Z. Najmudin, A. Thomas, J. Collier, A. Dangor, E. Divall, P. Foster, J. Gallacher, C. Hooker, D. Jaroszynski, A. Langley, W. Mori, P. Norreys, F. Tsung, R. Viskup, B. Walton, K. Krushelnick, Nature **431**, 535 (2004).

[5] C.G.R. Geddes, C. Toth, J. van Tilborg, E. Esarey, C. Schroeder, D. Bruhwiller, C. Nieter, J. Cary, W. Leemans, Nature **431**, 538 (2004).

[6] http://www-ssrl.slac.stanford.edu/lcls/commissioning/documents/th3pbi01.pdf

[7] P. Gibbon. *Short Pulse Laser Interaction with Matter*, Imperial College Press, London (2005).

[8] D. Bauer, P. Mulser and W.-H. Steeb, Phys. Rev. Let. **75**, 4622 (1995).

[9] P. Mora and T.M. Antonsen, Phys. Plasmas **4**, 217 (1997).

[10] R.J. Goldston and P. H. Rutherford. *Plasmaphysik - Eine Einführung*, Vieweg Verlag, Wiesbaden (1998).

[11] P. Kaw and J. Dawson, Physics of Fluids **13**, 472 (1970).

[12] M. Geissler, J. Schreiber, and J. Meyer-ter-Vehn, New J. Phys. **8** 186 (2006).

[13] J. Faure, Y. Glinec, A. Pukhov, S. Kiselev, S. Gordienko, E. Lefebvre, J.-P. Rousseau, F. Burgy, V. Malka, Nature **431**, 541 (2004).

[14] W.D. Kilpatrick, Rev. Sci. Instr. **28**, 824 (1957).

[15] Technical Design Report: http://xfel.desy.de/tdr/tdr.

[16] ELI: http://www.extreme-light-infrastructure.eu/

[17] J. Schreiber, F. Bell, F. Grüner, U. Schramm, M. Geissler, M. Schnürer, S. Ter-Avetisyan, B. M. Hegelich, J. Cobble, E. Brambrink, J. Fuchs, P. Audebert and D. Habs, Phys. Rev. Lett. **97**, 045005 (2006).

[18] T. Esirkepov, M. Yamagiwa and T. Tajima, Phys. Rev. Lett. **96**, 105001 (2006).

[19] J. Fuchs, P. Antici, E. D'Humire, E. Lefebvre, M. Borghesi, E. Brambrink, C. A. Cecchetti, M. Kaluza, V. Malka, M. Manclossi, S. Meyroneinc, P. Mora, J. Schreiber, T. Toncian, H. Ppin and P. Audebert, Nature Phys. **2**, 48 (2006).

[20] S.C. Wilks, W.L. Kruer, M. Tabak and A.B. Langdon, Phys. Rev. Lett. **69**, 1383 (1992).

[21] A. Henig et al., Phys. Rev. Lett **102**, 095002 (2009).

[22] M. Chen, A. Pukhov and T. P. Yu, Phys. Rev. Lett. **103**, 024801 (2009).

[23] A. Macchi, F. Cattani, T.V. Liseykina and Fulvio Cornolti, Phys. Rev. Lett. **94**, 165003 (2005).

[24] O. Klimo, J. Psikal, J. Limpouch, and V. T. Tikhonchuk, Phys. Rev. ST Accelerators and Beams **11**, 031301 (2008).

[25] X. Q. Yan, C. Lin, Z. M. Sheng, Z. Y. Guo, B. C. Liu, Y. R. Lu, J. X. Fang and J. E. Chen, Phys. Rev. Lett. **100**, 135003 (2008).

[26] A.P.L. Robinson, M. Zepf, S. Kar, R.G. Evans and C. Bellei, New J. Phys **10**, 013021 (2008).

[27] B. Rau et al., Phys. Rev. Lett. **78**, 3310 (1997).

[28] X.Q. Yan, C. Lin, Z.M. Sheng, Z.Y. Guo, B.C. Liu, Y.R. Lu, J.X. Fang and J. E. Chen, Phys. Rev. Lett. **100**, 135003 (2008).

[29] Toshiki Tajima, Dietrich Habs, Xueqing Yan, accepted for publication in Review of Accelerator Science and Technology Vol. 2, World Scientific Publishing Company, (2009).

[30] A. Henig, S. Steinke, M. Schnürer, T. Sokollik, R. Hörlein, D. Kiefer, D. Jung, J. Schreiber, B. M. Hegelich, X. Q. Yan, J. Meyer-ter-Vehn, T. Tajima, P. V. Nickles, W. Sander and D. Habs, accepted for publication in Physical Review Letters.

[31] J.D. Jackson, *Classical Electrodynamics* John Wiley & Sons (1999).

[32] B. van der Geer and M. de Loos, PhD. thesis, Technische Universiteit Eindhoven (2001).

[33] General Particle Tracer, www.pulsar.nl.

[34] K. Flöttmann, Astra User's Manual, www.desy.de/∼mpyflo (2000).

[35] K. Wille, *Physik der Teilchenbeschleuniger und Synchrotronstrahlungsquellen*, B.G. Teubner Stuttgart (1996).

[36] H. Wollnik, *Optics of charged particles*, San Diego u.a., Acad. Pr. (1987).

[37] C.M.S. Sears, R.L. Byer, E.R. Colby, B.M. Cowan, R. Ischebeck, M.R. Lincoln, T. Plettner, R.H. Siemann, J.E. Spencer, *Beam Coupling to Optical Scale Accelerating Structures* 12th Advanced Accelerator Concepts Workshop. Lake Geneva, Wisconsin, USA. July 10-15, 2005. SLAC-PUB-12422.

[38] K. Floettmann, Phys. Rev. ST Accelerators and Beams **6**, 034202 (2003).

[39] E. D. Courant and H. S. Snyder, Annals of Physics **3**, 1-48 (1958).

[40] K. Halbach, Nucl. Instr. Meth. **187**, 109 (1981)

[41] *Image taken from* http://www.xfel.eu/en/in-comparison.

[42] J.B. West, P.R. Woodruff, K. Codling and R.G. Houlgate, J. Phys. B **9** (1976) 407.

[43] V. Schmidt, N. Sandner, H. Kuntzmüller, P. Dhez, F. Wuilleumier and E. Kallne Phys. Rev. A and R.G. Houlgate, J. Phys. B **13** (1976) 1746.

[44] Onuki Onuki, Hideo Onuki, Pascal Elleaume, *Undulators, Wigglers and Their Applications*, Taylor & Francis Ltd. (2002).

[45] *Image taken from* www.wikipedia.org.

[46] Michael Scheer, PhD. thesis, Humboldt-Universität zu Berlin (2008).

[47] M. Fuchs *et al.*, Nature Physics, accepted for publication.

[48] Stanford Linear Accelerator Center: http://ssrl.slac.stanford.edu/lcls.

[49] S. Reiche, Nucl. Instrum. Methods Phys. Res. A **429**, 243 (1999).

[50] R. Bonifacio, C. Pellegrini, and L.M. Narduci, Opt. Comm. **50**, 373 (1984).

[51] M. Xie, Nucl. Instrum. Methods Phys. Res. A **445**, 59 (2000).

[52] W.P. Leemans *et al.*, Nature Phys. **2**, 696-9 (2006).

[53] J. Osterhoff *et al.*, Phys. Rev. Lett. Phys. Rev. Lett. **101**, 085002 (2008).

[54] R.A. Bosch, Phys. Rev. ST Accelerators and Beams **10**, 050701 (2007).

[55] G. Geloni, E. Saldin, E. Schneidmiller and M. Yurkov, Nucl. Instrum. Methods Phys. Res., Sect. A **578**, 34 (2007).

[56] G. Stupakov and Z. Huang, Phys. Rev. ST Accelerators and Beams **11**, 014401 (2008).

[57] F. Grüner, C. Schroeder, A.R. Maier, S. Becker and Y.M. Mikhailova, Phys. Rev. ST Accel. Beams **12**, 020707 (2009).

[58] G. Fubiani, J. Qiang, E. Esarey, W.P. Leemans and G. Dugan, Phys. Rev. ST Accelerators and Beams **9**, 064402 (2006).

[59] F. Grüner, S. Becker, U. Schramm, T. Eichner, M. Fuchs, R. Weingartner, D. Habs, J. Meyer-ter-Vehn, M. Geissler, M. Ferrario, L. Serafini, B. an der Geer, H. Backe, W. Lauth and S. Reiche, Appl. Phys. B **86**, 431 (2007).

[60] T. Eichner, F. Grüner, S. Becker, M. Fuchs, U. Schramm, R. Weingartner, D. Habs, H. Backe, P. Kunz, W. Lauth, Phys. Rev. ST Accel. Beams **10**, 082401 (2007).

[61] J.K. Lim et al, Phys. Rev. ST Accel. Beams **8**, 072401 (2005).

[62] T. Mihara, Y. Iwashita, M. Kumada, C.M. Spencer, *Superstrong Adjustable Permanent Magnet for a Linear Collider Final Focus* 12th Linear Accelerator Conference. Lübeck, Germany. August 16-20, 2004. SLAC-PUB-10878.

[63] M. Schollmeier, S. Becker, M. Geißel, K.A. Flippo, A. Blažević, S.A. Gaillard, D.C. Gautier, F. Grüner, K. Harres, M. Kimmel, F. Nürnberg, P. Rambo, U. Schramm, J. Schreiber, J. Schütrumpf, J. Schwarz, N.A. Tahir, B. Atherton, D. Habs, B.M. Hegelich, M. Roth, Phys. Rev. Lett **101**, 055004 (2008).

[64] Vacuumschmelze Hanau, Vacodym 764 HR data sheets (2005) www.vacuumschmelze.com.

[65] G. Datzmann, G. Dollinger, G. Hinderer, H.-J. Körner, Nucl. Instr. Meth. B **158**, 74 (1999).

[66] Y. Iwashita, T. Mihara, M. Kumada, C.M. Spencer, *Field Quality and Magnetic Center Stability Achieved in a Variable Permanent Magnet Quadrupole for the Ilc* PAC at Knoxville, TN, USA. May 16-20, 2005. SLAC-PUB-11667.

[67] I. Hlásnik, J. Kokavec, *Hall Generator In Inhomogenous Field And Dipole Notion Of The Hall Effect*, Solid State Electronics **9**, 585-594, Pergamon Press (1966).

[68] V. Yu. Korovkin, *Hall EMF in a Two-Dimensional Inhomogeneous Magnetic Field*, Translated from Izmeritel'naya Tekhnika, **8**, 50 (1988).

[69] R.G. Barrera, G.A. Estvez, J. Giraldo, Eur. J. Phys. **6** 287-294 (1985).

[70] CST EM Studio, www.cst.com.

[71] M.D. Perry and G. Mourou, Science **264**, 917 (1994).

[72] M.M. Murnane *et al.*, Science **251**, 531 (1991).

[73] K.W.D. Ledingham *et al.*, Science **300**, 1107 (2003).

[74] M. Tabak *et al.*, Phys. Plasmas **1**, 1626 (1994).

[75] M. Roth *et al.*, Phys. Rev. Lett. **86**, 436 (2001).

[76] R.A. Snavely *et al.*, Phys. Rev. Lett. **85**, 2945 (2000).

[77] E.L. Clark *et al.*, Phys. Rev. Lett. **84**, 670 (2000).

[78] A. Maksimchuk *et al.*, Phys. Rev. Lett. **84**, 4108 (2000).

[79] M. Hegelich *et al.*, Phys. Rev. Lett. **89**, 085002 (2002).

[80] S.C. Wilks *et al.*, Phys. Plasmas **8**, 542 (2001).

[81] J. Fuchs *et al.*, Nature Phys. **2**, 48 (2006).

[82] T.E. Cowan *et al.*, Phys. Rev. Lett. **92**, 204801 (2004).

[83] L. Romagnani *et al.*, Phys. Rev. Lett. **95**, 195001 (2005).

[84] A. Pukhov, Phys. Rev. Lett. **86**, 3562 (2001).

[85] P.K. Patel *et al.*, Phys. Rev. Lett. **91**, 125004 (2003).

[86] B.M. Hegelich *et al.*, Nature **439**, 441 (2006).

[87] H. Schwoerer *et al.*, Nature **439**, 445 (2006).

[88] M. Zepf *et al.*, Phys. Rev. Lett. **90**, 064801 (2003).

[89] T. Toncian *et al.*, Science **312**, 410 (2006).

[90] S. Kar *et al.*, Phys. Rev. Lett. **100**, 105004 (2008).

[91] V. Yanovsky *et al.*, Optics Express **16**, 2109 (2008).

[92] J. Schwarz *et al.*, J. Phys.: Conf. Ser. **112**, 032020 (2008).

[93] GAFchromic radiochromic film types HD-810 and MD-V2-55 are trademarks of ISP corporation.

[94] J.F. Ziegler, J.P. Biersack and U. Littmark, *The Stopping and Range of Ions in Solids.* (Pergamon Press, New York, 1985) `http://www.srim.org`.

[95] M. Roth *et al.*, PRST-AB **5**, 061301 (2002).

[96] S. Humphries, Jr., *Charged Particle Beams.* (John Wiley and Sons, 1990), `http://www.fieldp.com/cpb.html` (2008).

[97] M. Borghesi *et al.*, Phys. Rev. Lett. **92**, 055003 (2004).

[98] M. Bonitz, G. Bertsch, V.S. Filinov and H. Ruhl, *Introduction to Computational Methods in Many Body Physics* (Cambridge University Press, Cambridge, 2004).

[99] E. Brambrink *et al.*, Phys. Rev. E **75**, 065401(R) (2007).

[100] A.V. Bushman, I.V. Lomonosov and V.E. Fortov, *Equations of State for Materials at High Energy Density [in russian].* (Moskow: Institute of Problems of Chemical Physics, Chernogolovka, 1992).

[101] W.P. Leemans, B. Nagler, A. Gonsalves, C. Toth, K. Nakamura, C. Geddes, E. Esarey, C. Schroeder, S. Hooker, Nature Physics **2**, 696 (2006).

[102] J. Faure, C. Rechatin, A. Norlin, A. Lifschitz, Y. Glinec, V. Malka Nature **444**, 737 (2006).

[103] A. Rousse, K.T. Phuoc, R. Shah, A. Pukhov, E. Lefebvre, V. Malka, S. Kiselev, F. Burgy, J.-P. Rousseau, D. Umstadter, D. Hulin, Phys. Rev. Lett. **93**, 135005 (2004).

[104] P. Elleaume, J. Chavanne, B. Faatz, Nucl. Instr. Meth. **A 455**, 503 (2000).

[105] M. El-Ghazaky, H. Backe, W. Lauth, G. Kube, P. Kunz, A. Sharafutdinov, T. Weber, Europ. Phys. Journal **A 28**, 197 (2006).

[106] J.K. Lim, P. Frigola, G. Travish, J.B. Rosenzweig, S.G. Anderson, W.J. Brown, J.S. Jacob, C.L. Robbins, A.M. Tremaine, Phys. Rev. ST Accelerators and Beams **8**, 072401 (2005).

[107] S. Dambach, H. Backe, Th. Doerk, N. Eftekhari, H. Euteneuer, F. Görgen, F. Hagenbuck, K. H. Kaiser, O. Kettig, G. Kube, W. Lauth, H. Schöpe, A. Steinhof, Th. Tonn, and Th. Walcher, Phys. Rev. Lett. **80**, 5473 (1998) and S. Dambach, PhD thesis (Univ. Mainz, unpublished).

[108] I. Vassermann,E.R. Moog, Rev. Sci. Instr. **66**, 1943 (1995).

[109] R.W. Warren, Nucl. Instr. Meth. **A 272**, 257 (1988).

[110] T. Eichner, Diploma Thesis LMU Munich, unpublished (2007).

[111] R.P. Walker, Nucl. Instr. Meth. **A 335**, 328 (1993).

[112] http://www.kph.uni-mainz.de/B1/floorplan.php.

[113] T. Tanaka, H. Kitamura, J. of Synch. Rad. **8**, 1221 (2001).

[114] W. Lauth, H. Backe, O. Kettig, P. Kunz, A. Sharafutdinov, T. Weber, Europ. Phys. Journal **A 28**, 185 (2006).

[115] A.W. Chao, *Physics of collective beam instabilities in high energy accelerators* (John Wiley & Sons, New York, 1993); K. Bane, SLAC-PUB-11829 (2006).

[116] M. Sands, Phys. Rev. **97**, 470 (1955).

[117] T. Hara, T. Tanaka, H. Kitamura, T. Bizen, X. Marechal, T. Seike, T. Kohda, Y. Matsuura, Phys. Rev. ST Accelerators and Beams **7**, 050702 (2004).

[118] T. Hezel, B. Krevet, H. O. Moser, J. A. Rossmanith, R. Rossmanith and T. Schneider, J. Synchrotron Rad. **5**, 448 (1998).

[119] S. Casalbuoni, M. Hagelstein, B. Kostka, R. Rossmanith, M. Weisser, E. Steffens, A. Bernhard, D. Wollmann, T. Baumbach, Phys. Rev. ST Accelerators and Beams **9**, 010702 (2006).

[120] R. Rossmanith, private communication (2007).

[121] R. Neutze *et al.*, Nature **406**, 752 (2000).

[122] A. Baltuska *et al.*, Nature **421**, 611 (2003).

[123] W. Thomlinson, P. Suortti, and D. Chapman, Nucl. Instrum. Methods Phys. Res. A **543**, 288 (2005).

[124] A. Pukhov and S. Gordienko, Phil. Trans. R. Soc. A **364**, 623 (2006).

[125] D.J. Spence, A. Butler, and S. Hooker, J. Opt. Soc. Am. B **20**, 138 (2003).

[126] http://www.attoworld.de/research/PFS.html.

[127] Note that the detector resolution in the cited GeV-experiment did not suffice to resolve energy spreads below one percent.

[128] Technical Design Report: http://www-hasylab.desy.de/facility/fel/vuv/ttf2_update/TESLA-FEL2002-01.pdf.

[129] M.J. de Loos, S.B. van der Geer, Proc. 5th Eur. Part. Acc. Conf., Sitges, 1241 (1996).

[130] M. Dohlus and T. Limberg, Proceedings of the FEL 2004 Conference, 18-21.

[131] G. Fubiana, J. Qiang, E. Esarey, and W.P. Leemans, Phys. Rev. ST Accel. Beams **9**, 064402 (2006).

[132] E. Saldin, E.A. Schneidmiller, and M.V. Yurkov, Nucl. Instrum. Methods Phys. Res. A **417**, 158 (1998).

[133] M. Ferrario, J. E. Clendenin, D. T. Palmer, J. B. Rosenzweig, L. Serafini, Proc. of the 2nd ICFA Adv. Acc. Workshop on "The Physics of High Brightness Beams", UCLA, Nov., 1999; see also SLAC-PUB-8400.

[134] A.W. Chao, *Physics of collective beam instabilities in high energy accelerators* (John Wiley & Sons, New York, 1993); K. Bane, SLAC-PUB-11829 (2006).

[135] M. Sands, Phys. Rev. **97**, 470 (1955).

[136] S. Karsch *et al.*, New J. Phys **9**, 415 (2007).

[137] E. T. Scharlemann, J. Appl. Phys. **58**, 2154 (1985).

[138] R.P. Walker, Nucl. Instrum. Methods **214**, 497 (1983).

[139] S. Becker, M. Bussmann, S. Raith, M. Fuchs, R. Weingartner, P. Kunz, W. Lauth, S. Schramm, M. El Ghazaly, F. Grüner, H. Backe, D. Habs, arXiv 0902.2371

List Of Publications

- **S. Becker**, M.R. Maier, S. Raith, C. Frevert, T. Seegebrock, M. Scheer, M. Fuchs, R. Weingartner and F. Grüner,
  Design Study for a Strong Focusing Quadrupole Undulator,
  submitted to Physical Review Special Topics - Accelerators And Beams.

- **S. Becker**, M.R. Maier,
  Quadrupole Undulator Apparatus,
  patent pending.

- M. Fuchs, R. Weingartner, A. Popp, Zs. Major, **S. Becker**, J. Osterhoff, I. Cortrie, R. Hörlein, G. D. Tsakiris, U. Schramm, T. P. Rowlands-Rees, S. M. Hooker, D. Habs, F. Krausz, S. Karsch and F. Grüner,
  Laser-driven soft-X-ray undulator source,
  accepted for publication in Nature Physics.

- **S. Becker**, P.B. Hilz, F. Grüner and D. Habs,
  On Retardation Effects in Space Charge Calculations Of High Current Electron Beams,
  Physical Review Special Topics - Accelerators And Beams **12**, 101301 (2009).

- **S. Becker**, M. Bussmann, M. Fuchs, R. Weingartner, P. Kunz, W. Lauth, U. Schramm, S. Raith, M. El Ghazaly, F. Grüner, H. Backe and D. Habs,
  Characterization and Tuning of Ultra High Gradient Permanent Magnet Quadrupoles,
  Physical Review Special Topics - Accelerators And Beams **12**, 102801 (2009).

- F. Grüner, C. Schroeder, A.R. Maier, **S. Becker** and Y.M. Mikhailova,
  Space-charge effects in ultra-high current electron bunches generated by laser-plasma accelerators,
  Physical Review Special Topics - Accelerators And Beams **12**, 020707 (2009).

- J. Osterhoff, A. Popp, Zs. Major, B. Marx, T. P. Rowlands-Rees, M. Fuchs, M. Geissler, R. Hörlein, B. Hidding, **S. Becker**, E. A. Peralta, U. Schramm, F. Grüner, D. Habs, F. Krausz, S. M. Hooker, and S. Karsch,
  Generation of stable, low-divergence electron beams by laser wakefield acceleration in a steady-state-flow gas cell,
  Physical Review Letters **101**, 085002 (2008).

- M. Schollmeier, **S. Becker**, M. Geißel, K.A. Flippo, A. Blažević, S.A. Gaillard, D. C. Gautier, F. Grüner, K. Harres, M. Kimmel, F. Nürnberg, P. Rambo, U. Schramm, J. Schreiber, J. Schütrumpf, J. Schwarz, N.A. Tahir, B. Atherton, D. Habs, B.M. Hegelich and M. Roth,
  Controlled transport and focusing of laser-accelerated protons with miniature magnetic devices,
  Physical Review Letters **101**, 055004 (2008).

- S. Karsch, J. Osterhoff, A. Popp, T. P. Rowlands-Rees, Zs. Major, M. Fuchs, B. Marx, R. Hörlein, K. Schmid, L. Veisz, **S. Becker**, U. Schramm, B. Hidding, G. Pretzler, D. Habs, F. Grüner, F. Krausz and S. M. Hooker,
  GeV-scale electron acceleration in a gas-filled capillary discharge waveguide,
  New Journal of Physics **9**, 415 (2007).

- T. Eichner, F. Grüner, **S. Becker**, M. Fuchs, U. Schramm, R. Weingartner, D. Habs, H. Backe, P. Kunz and W. Lauth,
  Miniature magnetic devices for laser-based, table-top free-electron lasers,
  Physical Review Special Topics - Accelerators And Beams **10**, 082401 (2007).

- F. Grüner, **S. Becker**, U. Schramm, T. Eichner, M. Fuchs, R. Weingartner, D. Habs, J. Meyer-ter-Vehn, M. Geissler, M. Ferrario, L. Serafini, B. an der Geer, H. Backe, W. Lauth and S. Reiche,
  Design considerations for table-top, laser-based VUV and X-ray free electron lasers,
  Appl. Phys. B **86**, 431 (2007).

Acknowledgements

I would like to thank Prof. Dr. Roland Sauerbrey for his support and for accepting this thesis.

The research discussed in this thesis mainly relates to the subject of laser-driven Table-Top Free-Electron-Lasers and thus I would like to thank Prof. Dr. Florian Grüner, the head of the TT-TEL group. His support and encouragement was of importance during the completion of this thesis.

I would like to thank Prof. Dr. Stefan Karsch an Dr. Peter Thirolf for their feedback during the process of writing this thesis without which this thesis would not be the same.

Dr. Ulrich Schramm delivered essential knowledge concerning the TT-FEL project, starting from the laser and encompassing the beam transport elements and the diagnostics. I have always been able to trust his judgments. Particular thanks go to Dr. Werner Lauth, Dr. Peter Kunz and Prof. Dr. Hartmut Backe who made an important contribution in developing and testing the undulator. They also made many beam times possible at the MAMI accelerator in Mainz, which were necessary for understanding and improving the undulator and quadrupole devices.

Many thanks go also to Prof. Dr. Friedhelm Bell for many hours of very valuable discussions about questions and problems which improved the results of this thesis. Special thanks go to Dr. Thorsten Limberg, Dr. Martin Dohlus and Dr. Klaus Flöttmann from the DESY, where I had the opportunity to spend time having valuable discussions. I want to tank Dr. Michael Scheer from the Helmholtz Zentrum Berlin for valuable discussions about undulators and undulator radiation. Thanks go to Dr. Walter Assmann for very important support. I would also like to thank Prof. Dr. Dietrich Habs for the opportunity to work at his chair.

Special thanks go to Dr. Michael Bussmann, who has always been a reliable source of inspiration which improved the results of this work. I would also like to thank Dr. Thomas Morgan for discussions concerning physics and topics beyond. His devotion to events commonly referred to as “socializing” greatly improved the working atmosphere not only among the people in the first floor of the Coulombwall, but also with other research groups and the workshop. Special thanks also go to Dr. Mario Schubert. His programming skills in combination with his understanding of physics lead to a calculation tool based on “GEANT 4”. This tool is sill the foundation of many calculations performed concerning

radiation background and electron scattering in experiments relating to laser-based electron acceleration performed.

I further want to thank Sebastian Raith who is the diploma student working on improving the tuning of miniature quadrupoles. His devotion to details lead to valuable discussions and improvements in understanding the very important miniature quadrupole devices. I further thank my colleagues Matthias Fuchs, Raphael Weingartner and Thomas Eichner. Although some beam times at MAMI have been strenuous, their company made them a delight and a success (certainly with the help of Mr. Bachforelle, whom I want to thank as well).

Further I want to thank Peter Hilz, Wolf Rittershofer, Stefan Neukamm, Christian Lang, Jürgen Neumayr, Andreas Maier, Carlo Frevert, Patrick Polzer, Tobias Weineisen, Andrea Leinthaler, Ludwig Treppl, Walter Carli, Ralf Hertenberger, Klaus Steinberger, Otto Schaile, Martin Gross, Rolf Oehm and this crew and all the people I forgot to mention here.

Last but not least, thanks go to my parents and my brothers who have always been an important source of encouragement and inspiration.